

**OOPSI: A FAMILY OF OPTIMAL OPTICAL SPIKE INFERENCE
ALGORITHMS
FOR INFERRING NEURAL CONNECTIVITY FROM
POPULATION CALCIUM IMAGING**

by

Joshua T. Vogelstein

A dissertation submitted to The Johns Hopkins University in conformity with the
requirements for the degree of Doctor of Philosophy.

Baltimore, Maryland

Dec, 2009

© Joshua T. Vogelstein 2009

All rights reserved

Abstract

Since Ramon y Cajal observed that brains seem to be composed of networks of neurons, neuroscientists and others have wondered about the details of these networks. This work hopefully brings us one step closer towards realizing that goal, at least for small sub-networks. More specifically, this work assumes that the activity of a neural ensemble of around 100–1000 cells has been imaged with calcium indicators; the task is then to infer the most likely set of connections governing these observable neurons. To that end, we built three complementary algorithms. First, a fast, nonnegatively constrained deconvolution filter to infer spike trains online, without requiring any user intervention after image registration and segmentation. Second, a sequential Monte Carlo (SMC) filter can further refine the spike train estimates, and incorporate spike history terms, which are used to infer connectivities. Third, an algorithm to infer the mostly likely connectivity, given the SMC output. While the first two algorithms have been verified using *in silico*, *in vitro*, and *in vivo* experiments, the connectivity inference remains to be confirmed with living cells. That said, the discussion describes several next steps that are currently ongoing.

ABSTRACT

Primary Reader and Advisor: Eric Young

Secondary Reader: David Yue

Acknowledgements

thank you parents for literally creating me. then, you went beyond, and showed me complete and unconditional love and support for everything that i did, from leaving naked mannequins named “happy birthday ellen” for dr. so-and-so, to biking around eastern european countryside. i wouldn’t really say that i *need* much, but i literally *needed* you, to get here; and i’ll probably need you to get anywhere else in the future, so thanks in advance for that.

thank you rest of my family, especially jacob (always showing me the way), rachel (being the way), ahava (only reflecting my best), sage (being obviously perfect), and the wienerhead crew (providing me a place i think of as home, and being in that home with me).

thank you my friends, especially caplis, joel, the weinbergs, seth, alice. turns out, you are my family too. see above for details regarding my love for you, and the necessity of you.

thank you eric for providing financial and emotional support for all the years, even though my research interests were far outside the fields of what had been your normal

ACKNOWLEDGEMENTS

inquires. like my family/friends, i literally could not have done this without your support.

thank you to the rest of my “official” thesis committee, ed, david, kechen, and especially bruno. i could imagine being able to find such a breadth and depth of knowledge elsewhere, but finding those qualities in people who i want to be my teachers in life, not just in school, has been a special gift for me.

thank you to yuste-paninski crew (adam, baktash, brendon, darcy, tanya, tim, and yuriy) for providing a comfy lab home for me in nyc, data, theory, code, and insight. although this acknowledgement section is beginning to feel repetitive, i literally couldn’t have done this stuff without you (in fact, some of the stuff in here you actually did).

thank you to the rest of my “unofficial” thesis committee, including, at various times, alipasha vaziri, vincent bonin, david greenberg, karel svoboda, and especially mike tadross and quentin huys, who provide far more than brilliant insight and reflections.

thank you liam. i went to you a bunch of years ago because i liked hanging out with you, and i had a problem i didn’t know how to solve. you told me how i could do it. i kept coming back for more. i hope to keep coming back for more for years to come. you helped me learn about a whole world of statistics, that my mind essentially lives in now. this mode of thought has permeated all aspects of my life at this point. so, in a sense, i owe part of all my thoughts to you.

thank you to the “me” that worked on this stuff for the past few years. you were awesome. without you, well, i’m not even sure how to think about that . . .

Dedication

this thesis is dedicated to anybody that has ever, is ever, will ever, (and ‘any other tenses that i cannot imagine’ ever) love anybody or anything in any way. thank you. we love you.

Contents

Abstract	ii
Acknowledgements	iv
List of Tables	xiii
List of Figures	xiv
0 general introduction	1
1 fast-oopsi	4
1.1 Introduction	4
1.2 Methods	6
1.2.1 Data driven generative model	6
1.2.2 Goal	10
1.2.3 Inferring the most likely spike train, given a fluorescence trace . . .	12
1.2.4 Learning the parameters	15

CONTENTS

1.2.4.1	Initializing the parameters	16
1.2.4.2	Estimating the parameters given $\hat{\mathbf{n}}$	16
1.2.5	Spatial filtering	18
1.2.6	Overlapping spatial filters	21
1.2.7	Experimental Methods	23
1.2.7.1	Slice Preparation and Imaging	23
1.2.7.2	Electrophysiology	24
1.2.7.3	Fluorescence preprocessing	24
1.3	Results	25
1.3.1	Main Result	25
1.3.2	Online analysis of spike trains using the fast filter	29
1.3.3	Extensions	31
1.3.3.1	Replacing Gaussian observations with Poisson	31
1.3.3.2	Allowing for a time-varying prior	32
1.3.3.3	Saturating fluorescence	33
1.3.3.4	Using the fast filter to initialize the sequential Monte Carlo filter	34
1.3.4	Spatial filter	36
1.3.5	Overlapping spatial filters	38
1.4	Discussion	39
A	Wiener filter	43

CONTENTS

A.1	Pseudocode	44
A.2	Wiener Filter	46
2	smc-oopsi	47
2.1	Introduction	47
2.2	Model	50
2.3	Mathematical Methods	54
2.4	Experimental Methods	59
2.4.1	Slice Preparation and Imaging	59
2.4.2	Electrophysiology	60
2.5	Results	61
2.5.1	Main Result	61
2.5.2	Saturation	62
2.5.3	Superresolution	68
2.5.4	Spike History and Stimulus Dependence	70
2.5.5	Learning the parameters	74
2.6	Discussion	75
A	Details for constructing the particle filters	79
A.1	Linear observation particle filter	80
A.1.1	Constructing $q_{\theta}^L(n_t^{(i)})$	81
A.1.2	Constructing $q_{\theta}^L([Ca^{2+}]_t^{(i)})$	82

CONTENTS

A.1.3	Computing the weights and resampling when sampling from	
	$q_{\theta}^L([\text{Ca}^{2+}]_t^{(i)}, n_t^{(i)})$	83
A.2	Nonlinear observation particle filter	84
A.2.1	Constructing $q_{\theta}^{NL}(n_t^{(i)})$	85
A.2.2	Constructing $q_{\theta}^{NL}([\text{Ca}^{2+}]_t^{(i)})$	87
A.2.3	Computing the weights and reweighting when sampling from	
	$q_{\theta}^{NL}([\text{Ca}^{2+}]_t^{(i)}, n_t^{(i)})$	87
A.3	Superresolution particle filter	87
A.3.1	Superresolution one-observation-ahead sampling intuition	89
A.3.2	Computing $P_{\theta}^{NL}(F_v \mid [\text{Ca}^{2+}]_t)$ for all $t \in (u, v)$	94
A.3.2.1	Initializing $P_{\theta}^{NL}(F_v \mid [\text{Ca}^{2+}]_v)$	94
A.3.2.2	Recurring backwards	94
A.3.2.3	Approximating the 2^{v-t} component mixture	96
A.3.3	Superresolution sampling details	97
A.3.3.1	Superresolution sampling spikes	97
A.3.3.2	Superresolution sampling calcium	98
A.3.3.3	Computing the weights and reweighting when sampling	
	from $q_{\theta}^S([\text{Ca}^{2+}]_t^{(i)}, n_t^{(i)})$	99
A.4	GLM particle filter	99
B	Learning the parameters	102
B.1	Spike Rate Parameters	103

CONTENTS

B.2	Calcium Parameters	104
B.3	Spike History Parameters	106
B.4	Observation Parameters	106
3	pop-oopsi	108
3.1	Introduction	108
3.2	Methods	111
3.2.1	Model	111
3.2.2	Goal and general strategy	117
3.2.3	Initialization of intrinsic parameters via sequential Monte Carlo methods	119
3.2.4	A factorized approximation of the joint posteriors	122
3.2.5	Estimating the connectivity matrix	123
3.2.5.1	Imposing a sparse prior on the connectivity	124
3.2.5.2	Imposing Dale’s law on the connectivity	124
3.2.6	Specific implementation notes	125
3.2.7	Simulating a neural population	127
3.3	Results	129
3.3.1	Impact of coarse time discretization of calcium imaging data and scale factor of inferred connection weights	131
3.3.2	Impact of prior information on the inference	135
3.3.3	Impact of experimental factors on estimator accuracy	136

CONTENTS

3.3.4	Impact of strong correlations and deviations from generative model on the inference	140
3.4	Discussion	143
4	discussion	147
4.1	Towards improving image preprocessing	148
4.2	Towards improving spatial filtering	149
4.3	Towards improving spike inference	151
4.4	Towards improving connectivity learning	151
4.5	Towards confirming connectivity	152
	Bibliography	154
	Vita	185

List of Tables

2.1	calcium parameters	75
3.1	table of simulation parameters	130

List of Figures

1.1	data-based model	8
1.2	fast filter outperforms Wiener filter	27
1.3	parameters may be estimated using the fast filter	28
1.4	fast filter outperforms Wiener filter on biological data	29
1.5	fast filter outperforms Wiener filter on multi-spike events	30
1.6	fast filter is robust and works online for populations of neurons	31
1.7	fast filter can initialize Wiener filter	35
1.8	spatial filtering can improve effective SNR	37
1.9	overlapping spatial filters are not problematic	39
1.10	overlapping spatial filters can be estimated	40
2.1	main result	53
2.2	saturated simulation	65
2.3	in vivo bursts	66
2.4	real data saturation	67
2.5	array of inference	69
2.6	GLM PFS	72
2.7	in vitro data superresolution	73
A.1	laplace approximation	86
A.2	sampling strategies	90
A.3	mixture approximation	92
3.1	schematic overview	112
3.2	firing rate vs. $f(J)$	114
3.3	simulated example traces	116
3.4	quality of inferred connectivity matrices	131
3.5	low frame rate explains scale error	132
3.6	sparse prior improves estimate	136
3.7	sparse prior improves estimates 2	137

LIST OF FIGURES

3.8	accuracy vs. frame rate	138
3.9	accuracy vs. SNR	139
3.10	accuracy vs. imaging time and # of neurons	139
3.11	strong correlations break inference abilities	140
3.12	inference is robust to model misspecifications	141

Chapter 0

general introduction

In the early 1900's, Ramon y Cajal wrote that the brain seemed to be a *network* of neurons, connected to one another in beautifully complex ways [1]. Since then, people interested in neuroscience have devoted many thousands of hours towards unraveling these complicated networks [2]. Unfortunately, the pace of knowledge acquisition had been very slow, given the complete lack of any high-throughput mechanisms of determining neural circuitry.

Broadly speaking, people have approached the neural circuit inference problem from three distinct but related approaches: anatomical, functional, and effective. Anatomical measures of connectivity represent the gold standard: if two neurons are connected to one another, then, by definition, a synapse has been formed between the two. Functional measures of connectivity look at pairwise activations of neurons, to determine whether any pair is “functionally” connected [3]. Finally, effective measures of connectivity are model

CHAPTER 0. GENERAL INTRODUCTION

based [3]. By building a parametric model, and estimating those parameters from the data, one can infer the probability that any neuron is pre- or post-synaptic to any other observable neuron, given all the observations. It has been our belief that these effective measures of connectivity are the most promising for achieving high-throughput neural circuit inferences for relatively small populations of neurons (eg, $\approx 100 - 1000$).

That said, having the ability to reliably infer effective connectivity from small neural populations requires the development of a number of tools, both experimental and computational. Experimentally, the data must satisfy several criteria. First, some measure of the spiking activity of a set of interconnected neurons must be simultaneously observable. Second, that measure must have a sufficiently high signal-to-noise ratio (SNR), so that the precise spike timing can be determined with some reasonable confidence level. Third, the data acquisition rate must be sufficiently fast to observe the effects of one neuron spiking on the others. Fourth, the statistics of spiking must be such that the posterior probabilities of the effective connectivity parameters have sufficiently low variance.

Given that these experimental desiderata can be satisfied, computational tools can be developed to maximize the utility of these data. A similar set of desiderata can be established for the computational tools. First, the inference should be optimal, or approximately so. Second, inference should be expedient, possibly fast enough to be used online during experiments. Third, algorithms should be robust, and made to work “out-of-the-box,” without any (or many) knobs to turn. Fourth, all the (well documented) code should be freely available to everybody.

CHAPTER 0. GENERAL INTRODUCTION

The ethos of this thesis has been the following: assume that the experimental hurdles have been overcome, so now it is time to develop the computational tools. The hope was that either: (i) by the time this work was complete, the experimental desiderata would be satisfiable, or (ii) this work would encourage experimentalists to satisfy the above desiderata. It seems that both these hopes are being satisfied.

The text proceeds as follows. First, Chapter 1 describes a fast, non-negatively constrained deconvolution algorithm to quickly infer the most likely spike train, given the fluorescence trace for each neuron. Chapter 2 then develops a more sophisticated sequential Monte Carlo (SMC) method for refining the spike train estimates, given the fluorescence data. Chapter 3 then describes how to build on top of this SMC framework to infer connectivity. The discussion touches on current efforts to confirm inferred connectivity from both *in vitro* and *in vivo* experiments. All of the code, text, and data for each project are available from <http://github.com/jovo/>.

Chapter 1

fast-oopsi: a fast nonnegative deconvolution algorithm for inferring the approximate *maximum a posteriori* spike train¹

1.1 Introduction

Simultaneously imaging large populations of neurons using calcium sensors is becoming increasingly popular [4], both *in vitro* [5,6] and *in vivo* [7–9], and will likely continue as the signal-to-noise-ratio (SNR) of genetic sensors continues to improve [10–12]. Whereas

¹Note that the data in this chapter was collected by Tanya Sippy and Adam Packer in Rafael Yuste’s laboratory

CHAPTER 1. FAST-OOPSI

the data from these experiments are movies of time-varying fluorescence traces, the desired signal consists of spike trains of the observable neurons. Unfortunately, finding the most likely spike train is a challenging computational task, due to limitations of the SNR and temporal resolution, unknown parameters, and computational intractability.

A number of groups have therefore proposed algorithms to infer spike trains from calcium fluorescence data using very different approaches. Early approaches simply thresholded dF/F (e.g., [13, 14]) to obtain “event onset times.” More recently, Greenberg et al. [15] developed a template matching algorithm to identify individual spikes. Holekamp et al. [16] then applied an optimal linear deconvolution (ie, the Wiener filter) to the fluorescence data. This approach is natural from a signal processing standpoint, but does not utilize the knowledge that spikes are always positive. Sasaki et al. [17] proposed using machine learning techniques to build a nonlinear supervised classifier, requiring many hundreds of examples of joint electrophysiological and imaging data to “train” the algorithm to learn what effect spikes have on fluorescence. Vogelstein et al. [18] proposed a biophysical model-based sequential Monte Carlo method to efficiently estimate the probability of a spike in each image frame, given the entire fluorescence time-series. While effective, that approach is not suitable for online analyses of populations of neurons, as the computations run in about real-time per neuron (ie, analyzing one minute of data requires about one minute of computational time on a standard laptop computer).

The present work starts by building a simple model relating spiking activity to fluorescence traces. Unfortunately, inferring the most likely spike train given this model is

CHAPTER 1. FAST-OOPSI

computationally intractable. Making some reasonable approximations leads to an algorithm that infers the approximately most likely spike train, given the fluorescence data. This algorithm has a few particularly noteworthy features, relative to other approaches. First, spikes are assumed to be positive. This assumption often improves filtering results when the underlying signal has this property [19–26]. Second, the algorithm is fast: it can process a calcium trace from 50,000 images in about one second on a standard laptop computer. In fact, filtering the signals for an entire population of about 100 neurons runs faster than real-time. This speed facilitates using this filter online, as observations are being collected. In addition to these two features, the model may be generalized in a number of ways, including incorporating spatial filtering of the raw movie. The efficacy of the proposed filter is demonstrated on several biological data-sets, suggesting that this algorithm is a powerful and robust tool for online spike train inference. The code (which is a simple Matlab script) is available from the authors upon request.

1.2 Methods

1.2.1 Data driven generative model

Figure 1.1 shows data from a typical *in vitro* epifluorescence experiment (see section 1.2.7 for data collection details). The top panel shows the mean frame of this movie, including 3 neurons, two of which are patched. To build the model, the pixels within a

CHAPTER 1. FAST-OOPSI

region-of-interest (ROI) are selected (white circle). Given the ROI, all the pixel intensities of each frame can be averaged, to get a one-dimensional fluorescence time-series, as shown in the bottom left panel (black line). By patching onto this neuron, the spike train can also be directly observed (black bars). Previous work suggests that this fluorescence signal might be well characterized by convolving the spike train with an exponential, and adding noise [4]. This model is confirmed by convolving the true spike train with an exponential (gray line, bottom left panel), and then looking at the distribution of the residuals. The bottom right panel shows a histogram of the residuals (solid line), and the best fit Gaussian distribution (dashed line).

The above observations may be formalized as follows. Assume there is a one-dimensional fluorescence trace, F (throughout this text X indicates the vector $[X_1, \dots, X_T]$, where T is the index of the final frame), from a neuron. At time t , the fluorescence measurement F_t is a linear-Gaussian function of the intracellular calcium concentration at that time, $[\text{Ca}^{2+}]_t$:

$$F_t = \alpha[\text{Ca}^{2+}]_t + \beta + \sigma\varepsilon_t, \quad \varepsilon_t \stackrel{iid}{\sim} \mathcal{N}(0, 1). \quad (1.1)$$

The scale, α , absorbs all experimental variables impacting the scale of the signal, including the number of sensors within the cell, photons per calcium ion, amplification of the imaging system, etc. Similarly, the offset, β , absorbs the baseline calcium concentration of the cell, background fluorescence of the fluorophore, imaging system offset, etc. The standard deviation, σ , results from calcium fluctuations independent of spiking activity, fluorescence fluctuations independent of calcium, and imaging noise. The noise at each time, ε_t , is

CHAPTER 1. FAST-OOPSI

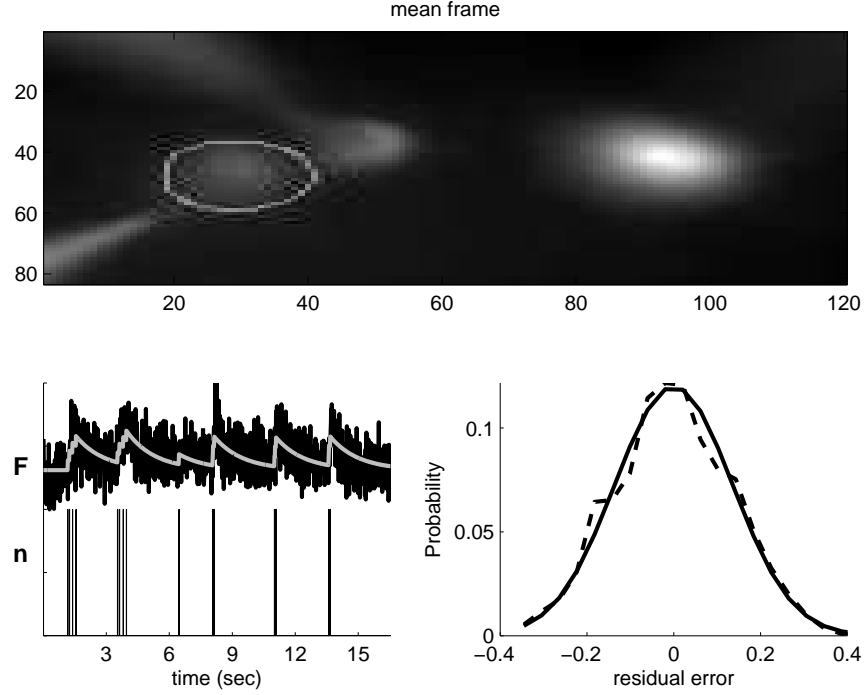


Figure 1.1: Typical *in vitro* data suggest that a reasonable first order model may be constructed by convolving the spike train with an exponential and adding Gaussian noise. Top panel: the average (over frames) of a typical field-of-view. Bottom left: true spike train recorded via a patch electrode (black bars), convolved with an exponential (gray line), superimposed on the fluorescence trace (OGB-1; black line). While the spike train and fluorescence trace are measured data, the calcium is not directly measured, but rather, inferred. Bottom right: a histogram of the residual error between the gray and black lines from the bottom left panel (dashed line), and the best fit Gaussian (solid line). Note that the Gaussian model provides a good fit for the residuals here.

independently and identically distributed according to a standard normal distribution (ie, Gaussian with zero mean and unit variance), as indicated by the notation $\overset{iid}{\sim} \mathcal{N}(0, 1)$.

Then, assuming that the intracellular calcium concentration, $[\text{Ca}^{2+}]_t$, jumps by $A \mu\text{M}$ after each spike, and subsequently decays back down to $C_b \mu\text{M}$ with time constant τ , one

CHAPTER 1. FAST-OOPSI

can write:

$$[\text{Ca}^{2+}]_{t+1} = (1 - \Delta/\tau)[\text{Ca}^{2+}]_t + (\Delta/\tau)C_b + An_t \quad (1.2)$$

where Δ is the time step size — which is the frame duration, or $1/(\text{frame rate})$ — and n_t indicates the number of times the neuron spiked in frame t . Note that because $[\text{Ca}^{2+}]_t$ and F_t are linearly related to one another, the fluorescence scale, α , and calcium scale, A , are not identifiable. In other words, either can be set to unity without loss of generality, as the other can absorb the scale entirely. Similarly, the fluorescence offset, β , and calcium baseline, C_b are not identifiable, so either can be set to zero without loss of generality. Finally, letting $\gamma = (1 - \Delta/\tau)$, Eq. (1.2) can be rewritten replacing $[\text{Ca}^{2+}]_t$ with its non-dimensionalized counterpart, C_t :

$$C_{t+1} = \gamma C_t + n_t. \quad (1.3)$$

Note that C_t does not refer to absolute intracellular concentration of calcium, but rather, a relative measure (see [18] for a more general model). The gray line in the bottom left panel of Figure 1.1 corresponds to the putative C of the observed neuron.

To complete the “generative model” (ie, a model from which simulations can be generated), the distribution from which spikes are sampled must be defined. Perhaps the simplest first order description of spike trains is that at each time, spikes are sampled according to a Poisson distribution with some rate:

$$n_t \stackrel{iid}{\sim} \text{Poisson}(\lambda\Delta) \quad (1.4)$$

CHAPTER 1. FAST-OOPSI

where $\lambda\Delta$ is the expected firing rate per bin, and Δ is included to ensure that the expected firing rate is independent of the frame rate. Thus, Eqs. (1.1), (1.3), and (1.4) complete the generative model.

1.2.2 Goal

Given the above model, the goal is to find the maximum *a posteriori* (MAP) spike train, i.e., the most likely spike train, $\hat{\mathbf{n}}$, given the fluorescence measurements, \mathbf{F} :

$$\hat{\mathbf{n}} = \operatorname{argmax}_{n_t \in \mathbb{N}_0 \forall t} P[\mathbf{n}|\mathbf{F}], \quad (1.5)$$

where $P[\mathbf{n}|\mathbf{F}]$ is the posterior probability of a spike train, \mathbf{n} , given the fluorescent trace, \mathbf{F} , and n_t is constrained to be an integer, $\mathbb{N}_0 = \{0, 1, 2, \dots\}$, because of the above assumed Poisson distribution. From Bayes' rule, the posterior can be rewritten:

$$P[\mathbf{n}|\mathbf{F}] = \frac{P[\mathbf{n}, \mathbf{F}]}{P[\mathbf{F}]} = \frac{1}{P[\mathbf{F}]} P[\mathbf{F}|\mathbf{n}] P[\mathbf{n}], \quad (1.6)$$

where $P[\mathbf{F}]$ is the evidence of the data, $P[\mathbf{F}|\mathbf{n}]$ is the likelihood of observing a particular fluorescence trace \mathbf{F} , given the spike train \mathbf{n} , and $P[\mathbf{n}]$ is the prior probability of a spike train. Plugging the far right-hand-side of Eq. (1.6) into Eq. (1.5), yields:

$$\hat{\mathbf{n}} = \operatorname{argmax}_{n_t \in \mathbb{N}_0 \forall t} \frac{1}{P[\mathbf{F}]} P[\mathbf{F}|\mathbf{n}] P[\mathbf{n}] = \operatorname{argmax}_{n_t \in \mathbb{N}_0 \forall t} P[\mathbf{F}|\mathbf{n}] P[\mathbf{n}], \quad (1.7)$$

where the second equality follows because $P[\mathbf{F}]$ merely scales the results, but does not change the relative quality of various spike trains. Both $P[\mathbf{F}|\mathbf{n}]$ and $P[\mathbf{n}]$ are available

CHAPTER 1. FAST-OOPSI

from the above model:

$$P[\mathbf{F}|\mathbf{n}] = P[\mathbf{F}|\mathbf{C}] = \prod_{t=1}^T P[F_t|C_t], \quad (1.8a)$$

$$P[\mathbf{n}] = \prod_{t=1}^T P[n_t], \quad (1.8b)$$

where the first equality in Eq. (1.8a) follows because \mathbf{C} is deterministic given \mathbf{n} , and the second equality follows from Eq. (1.1). Further, Eq. (1.8b) follows from the Poisson process assumption, Eq. (1.4). Both $P[F_t|C_t]$ and $P[n_t]$ can be written explicitly:

$$P[F_t|C_t] = \mathcal{N}(\alpha C_t + \beta, \sigma^2), \quad (1.9a)$$

$$P[n_t] = \text{Poisson}(\lambda\Delta), \quad (1.9b)$$

where both equations follow from the above model. Now, plugging Eq. (1.9) back into (1.8), and plugging that result into Eq. (1.7), yields:

$$\hat{\mathbf{n}} = \operatorname{argmax}_{n_t \in \mathbb{N}_0 \forall t} \prod_{t=1}^T \frac{1}{\sqrt{2\pi\sigma^2}} \exp \left\{ -\frac{1}{2} \frac{(F_t - \alpha C_t - \beta)^2}{\sigma^2} \right\} \frac{\exp\{-\lambda\Delta\}(\lambda\Delta)^{n_t}}{n_t!} \quad (1.10a)$$

$$= \operatorname{argmax}_{n_t \in \mathbb{N}_0 \forall t} \sum_{t=1}^T \left\{ -\frac{1}{2\sigma^2} (F_t - \alpha C_t - \beta)^2 + n_t \log \lambda\Delta - \log n_t! \right\}, \quad (1.10b)$$

where the second equality follows from taking the logarithm of the right-hand-side and dropping terms that do not depend on \mathbf{n} . Unfortunately, solving Eq. (1.10b) exactly is computationally intractable, as it requires a nonlinear search over an infinite number of possible spike trains. The search space could be restricted by imposing an upper bound, k , on the number of spikes within a frame. However, in that case, the computational complexity scales *exponentially* with the number of image frames — i.e., the number of computations required would scale with k^T — which for pragmatic reasons is intractable.

1.2.3 Inferring the most likely spike train, given a fluorescence trace

The goal here is to develop an algorithm to efficiently approximate $\hat{\mathbf{n}}$, the most likely spike train, given the fluorescence trace. Because of the computational intractability described above, Eq. (1.10) is approximated by modifying Eq. (1.4), replacing the Poisson distribution with an exponential distribution of the same mean. Modifying Eq. (1.10) to incorporate this approximation yields:

$$\hat{\mathbf{n}} \approx \operatorname{argmax}_{n_t > 0 \forall t} \prod_{t=1}^T \left\{ \frac{1}{\sqrt{2\pi\sigma^2}} \exp \left\{ -\frac{1}{2} \frac{(F_t - \alpha C_t - \beta)^2}{\sigma^2} \right\} (\lambda \Delta) \exp \{ -\lambda \Delta n_t \} \right\} \quad (1.11a)$$

$$= \operatorname{argmax}_{n_t > 0 \forall t} \sum_{t=1}^T -\frac{1}{2\sigma^2} (F_t - \alpha C_t - \beta)^2 - n_t \lambda \Delta \quad (1.11b)$$

where the constraint on n_t has been relaxed from $n_t \in \mathbb{N}_0$ to $n_t \geq 0$ (since the exponential distribution can yield any non-negative number). The advantage of this approximation is that the optimization problem becomes concave in \mathbf{C} , meaning that any gradient ascent method guarantees achieving the global maximum (because there are no local maxima, other than the single global maximum). To see that Eq. (1.11b) is concave in \mathbf{C} , rearrange Eq. (1.3) to obtain, $n_t = C_t - \gamma C_{t-1}$, so Eq. (1.11b) can be rewritten:

$$\mathbf{C} = \operatorname{argmax}_{C_t - \gamma C_{t-1} > 0 \forall t} \sum_{t=1}^T -\frac{1}{2\sigma^2} (F_t - \alpha C_t - \beta)^2 - (C_t - \gamma C_{t-1}) \lambda \Delta \quad (1.12)$$

which is a sum of terms that are concave in C_t , so the whole right-hand-side is concave. Unfortunately, the integer constraint has been lost, i.e., the answer could include “partial” spikes. This disadvantage can be remedied by thresholding (ie, setting $n_t = 1$ for all n_t

CHAPTER 1. FAST-OOPSI

greater than some threshold, and the rest setting to zero), or by considering the magnitude of a partial spike at time t as an indication of the probability of a spike occurring during frame t . Note that replacing a Poisson with an exponential is a common approximation technique in the machine learning literature [26, 27], as the exponential distribution is the closest log-concave relaxation to its non-log-concave counterpart, the Poisson distribution. More specifically, the probability mass function of a Poisson distributed random variable with low rate is very similar to the probability density function of a random variable with an exponential distribution. While this convex relaxation makes the problem tractable, the “sharp” threshold imposed by the non-negativity constraint prohibits the use of standard gradient ascent techniques. This may be rectified by dropping the sharp threshold, and adding a barrier term which must approach $-\infty$ as n_t approaches zero (this approach is often called an “interior-point” method). Iteratively reducing the weight of the barrier term guarantees convergence to the correct solution. Thus, the goal is to efficiently solve:

$$\hat{\mathbf{C}}_z = \underset{\mathbf{C}}{\operatorname{argmax}} \sum_{t=1}^T \left(-\frac{1}{2\sigma^2} (F_t - \alpha C_t - \beta)^2 - (C_t - \gamma C_{t-1}) \lambda \Delta + z \log(C_t - \gamma C_{t-1}) \right). \quad (1.13)$$

where $\log(\cdot)$ is the “barrier term”, and z is the weight of the barrier term. Iteratively solving for $\hat{\mathbf{C}}_z$ for z going from one down to nearly zero, guarantees convergence to $\hat{\mathbf{C}}$ [27]. The concavity of Eq. (1.13) facilitates utilizing any number of techniques guaranteed to find the global maximum. Because the argument of Eq. (1.13) is twice analytically differentiable, one can use the Newton-Raphson technique [28]. The special tridiagonal structure of the Hessian enables each Newton-Raphson step to be very efficient (as described below). To

CHAPTER 1. FAST-OOPSI

proceed, Eq. (1.13) can be rewritten in matrix notation. Note that:

$$\mathbf{MC} = \begin{bmatrix} -\gamma & 1 & 0 & 0 & \cdots & 0 \\ 0 & -\gamma & 1 & 0 & \cdots & 0 \\ \vdots & \ddots & \ddots & \ddots & \ddots & \vdots \\ 0 & \cdots & 0 & -\gamma & 1 & 0 \\ 0 & \cdots & 0 & 0 & -\gamma & 1 \end{bmatrix} \begin{bmatrix} C_1 \\ C_2 \\ \vdots \\ C_{T-1} \\ C_T \end{bmatrix} = \begin{bmatrix} n_1 \\ n_2 \\ \vdots \\ n_{T-1} \end{bmatrix}, \quad (1.14)$$

where $\mathbf{M} \in \mathbb{R}^{(T-1) \times T}$ is a bidiagonal matrix. Then, letting $\mathbf{1}$ be a $T - 1$ dimensional column vector, $\boldsymbol{\beta}$ be a T dimensional column vector of β 's, and $\boldsymbol{\lambda} = \lambda \Delta \mathbf{1}$ yields the objection function, Eq. (1.13), in more compact matrix notation:

$$\hat{\mathbf{C}}_z = \underset{\mathbf{MC} \geq \mathbf{0}}{\operatorname{argmax}} -\frac{1}{2\sigma^2} \|\mathbf{F} - \alpha \mathbf{C} - \boldsymbol{\beta}\|_2^2 - (\mathbf{MC})^\top \boldsymbol{\lambda} + z \log(\mathbf{MC})^\top \mathbf{1}, \quad (1.15)$$

where $\mathbf{MC} \geq \mathbf{0}$ indicates that every element of \mathbf{MC} is greater than or equal to zero, $\log(\cdot)$ indicates an element-wise logarithm, and $\|x\|_2$ is the standard L_2 norm, i.e., $\|x\|_2^2 = \sum_i x_i^2$. When using Newton-Raphson to ascend a surface, one iteratively computes both the gradient (first derivative) and Hessian (second derivative) of the argument to be maximized, with respect to the variables of interest (\mathbf{C} here). Then, the estimate is updated using $\mathbf{C}_z \leftarrow \mathbf{C}_z + s\mathbf{d}$, where s is the step size and \mathbf{d} is the step direction obtained by solving $\mathbf{H}\mathbf{d} = \mathbf{g}$. The gradient, \mathbf{g} , and Hessian, \mathbf{H} , for this model, with respect to \mathbf{C} , are given by:

$$\mathbf{g} = -\frac{\alpha}{\sigma^2} (\mathbf{F} - \alpha \mathbf{C} - \boldsymbol{\beta}) + \mathbf{M}^\top \boldsymbol{\lambda} - z \mathbf{M}^\top (\mathbf{MC})^{-1} \quad (1.16a)$$

$$\mathbf{H} = \frac{\alpha^2}{\sigma^2} \mathbf{I} + z \mathbf{M}^\top (\mathbf{MC})^{-2} \mathbf{M} \quad (1.16b)$$

CHAPTER 1. FAST-OOPSI

where the exponents on the vector \mathbf{MC} indicate element-wise operations. The step size, s , is found using “backtracking line searches”, which finds the maximal s that increases the posterior and is between zero and one [28].

Typically, implementing Newton-Raphson requires inverting the Hessian, i.e., solving $\mathbf{d} = \mathbf{H}^{-1}\mathbf{g}$, a computation that scales *cubically* with T (requires on the order of T^3 operations). Already, this would be a drastic improvement over the most efficient algorithm assuming Poisson spikes, which would require k^T operations (where k is the maximum number of spikes per frame). Here, because \mathbf{M} is bidiagonal, the Hessian is tridiagonal, so the solution may be found in about T operations, via standard banded Gaussian elimination techniques (which can be implemented efficiently in Matlab using $\mathbf{H} \setminus \mathbf{g}$, assuming \mathbf{H} is represented as a sparse matrix) [26]. In other words, the above approximation and inference algorithm reduces computations from *exponential* time to *linear* time. Appendix A.1 contains pseudocode for this algorithm, including learning the parameters, as described below.

1.2.4 Learning the parameters

We assumed above that the parameters governing the model, $\boldsymbol{\theta} = \{\alpha, \beta, \sigma, \gamma, \lambda\}$, were known, but in practice they are typically unknown. An algorithm to estimate the most likely parameters, $\hat{\boldsymbol{\theta}}$, could proceed as follows: (i) initialize some estimate of the parameters, $\hat{\boldsymbol{\theta}}$, then (ii) recursively compute $\hat{\mathbf{n}}$ using those parameters, and update $\hat{\boldsymbol{\theta}}$ given the new $\hat{\mathbf{n}}$, until some convergence criteria is met. Below, details are provided for each step.

1.2.4.1 Initializing the parameters

Because the model introduced above is linear, the scale of \mathbf{F} relative to \mathbf{n} is arbitrary. Therefore, before filtering, \mathbf{F} is linearly “squashed” between zero and one, ie $\mathbf{F} \leftarrow (\mathbf{F} - F_{min})/(F_{max} - F_{min})$, where F_{min} and F_{max} are the observed minimum and maximum of \mathbf{F} , respectively. Given this normalization, α is set to one. Because spiking is assumed to be sparse, \mathbf{F} tends to be around baseline, so β is initialized to be the median of \mathbf{F} , and σ is initialized as the median absolute deviation of \mathbf{F} , i.e., $\sigma = \text{median}_t(|F_t - \text{median}_s(F_s)|)/K$, where $\text{median}_i(X_i)$ indicates the median of X with respect to index i , and $K = 1.4785$ is the correction factor when using median absolute deviation as a robust estimator of the standard deviation. Because in these data, the posterior tends to be relatively flat along the γ dimension, i.e., large changes in γ result in relatively small changes in the posterior, estimating γ is difficult. Further, previous work has shown that results are somewhat robust to minor variations in time constant [29]; therefore γ is initialized at $1 - \Delta/(1\text{sec})$, which is fairly typical [30]. Finally, λ is initialized at 1 Hz, which is between typical baseline and evoked spike rate for these data.

1.2.4.2 Estimating the parameters given $\hat{\mathbf{n}}$

Ideally, one could integrate out the hidden variables, to find the most likely parameters:

$$\hat{\boldsymbol{\theta}} = \underset{\boldsymbol{\theta}}{\text{argmax}} \int P[\mathbf{F}, \mathbf{C}|\boldsymbol{\theta}]d\mathbf{C} = \underset{\boldsymbol{\theta}}{\text{argmax}} \int P[\mathbf{F}|\mathbf{C}; \boldsymbol{\theta}]P[\mathbf{C}|\boldsymbol{\theta}]d\mathbf{C}. \quad (1.17)$$

CHAPTER 1. FAST-OOPSI

However, evaluating those integrals is not particularly tractable. Therefore, Eq. (1.17) is approximated by simply maximizing the parameters given the MAP estimate of the hidden variables:

$$\hat{\boldsymbol{\theta}} \approx \operatorname{argmax}_{\boldsymbol{\theta}} P[\mathbf{F}, \hat{\mathbf{C}}|\boldsymbol{\theta}] = \operatorname{argmax}_{\boldsymbol{\theta}} P[\mathbf{F}|\hat{\mathbf{C}}; \boldsymbol{\theta}] P[\hat{\mathbf{n}}|\boldsymbol{\theta}] = \operatorname{argmax}_{\boldsymbol{\theta}} \{\log P[\mathbf{F}|\hat{\mathbf{C}}; \boldsymbol{\theta}] + \log P[\hat{\mathbf{n}}|\boldsymbol{\theta}]\}, \quad (1.18)$$

where $\hat{\mathbf{C}}$ and $\hat{\mathbf{n}}$ are determined using the above described inference algorithm. The approximation in Eq. (1.18) is good whenever most of the mass in the integral in Eq. (1.18) is around the MAP sequence, $\hat{\mathbf{C}}$.² The argument from the right-hand-side of Eq. (1.18) may be expanded:

$$\log P[\mathbf{F}|\hat{\mathbf{C}}; \boldsymbol{\theta}] + \log P[\hat{\mathbf{n}}|\boldsymbol{\theta}] = \sum_{t=1}^T \log P[F_t|\hat{C}_t; \alpha, \beta, \sigma] + \sum_{t=1}^T \log P[\hat{n}_t|\lambda]. \quad (1.19)$$

Note that the two terms in the right-hand-side of Eq. (1.19) may be optimized separately. The maximum likelihood estimate (MLE) for the observation parameters, $\{\alpha, \beta, \sigma\}$, is therefore given by:

$$\{\hat{\alpha}, \hat{\beta}, \hat{\sigma}\} = \operatorname{argmax}_{\alpha, \beta, \sigma > 0} \sum_{t=1}^T \log P[F_t|\hat{C}_t; \beta, \sigma] = \operatorname{argmax}_{\beta, \sigma > 0} -\frac{1}{2}(2\pi\sigma^2) - \frac{1}{2} \left(\frac{F_t - \alpha\hat{C}_t - \beta}{\sigma} \right)^2. \quad (1.20)$$

Note that a rescaling of α may be offset by a complementary rescaling of \mathbf{C} and β . Therefore, because the scale of \mathbf{C} is arbitrary, α can be set to one without loss of generality. Plugging $\alpha = 1$ into Eq. (1.20), and maximizing with respect to β yields:

$$\hat{\beta} = \operatorname{argmax}_{\beta > 0} \sum_{t=1}^T -(F_t - \hat{C}_t - \beta)^2. \quad (1.21)$$

²Eq. (1.18) may be considered a first-order Laplace approximation [31].

CHAPTER 1. FAST-OOPSI

Computing the gradient with respect to β , setting the answer to zero, and solving for $\hat{\beta}$, yields $\hat{\beta} = \frac{1}{T} \sum_t (F_t - \hat{C}_t)$. Similarly, computing the gradient of Eq. (1.20) with respect to σ , setting it to zero, and solving for $\hat{\sigma}$ yields:

$$\hat{\sigma} = \sqrt{\frac{1}{T} \sum_t (F_t - \hat{C}_t - \hat{\beta})^2}, \quad (1.22)$$

which is simply the root-mean-square of the residual error. Finally, the MLE of $\hat{\lambda}$ is given by solving:

$$\hat{\lambda} = \operatorname{argmax}_{\lambda > 0} \sum_t (\log(\lambda \Delta) - \hat{n}_t \lambda \Delta), \quad (1.23)$$

which, again, computing the gradient with respect to λ , setting it to zero, and solving for $\hat{\lambda}$, yields $\hat{\lambda} = T / (\Delta \sum_t \hat{n}_t)$, which is the inverse of the inferred average firing rate.

Iterations stop whenever (i) the iteration number exceeds some upper bound, or (ii) the relative change in likelihood does not exceed some lower bound. In practice, parameters tend to converge after several iterations, given the above initializations.

1.2.5 Spatial filtering

In the above, we assumed that the raw movie of fluorescence measurements collected by the experimenter had undergone two stages of preprocessing before filtering. First, the movie was segmented, to determine regions-of-interest (ROIs), yielding a vector, $\vec{F}_t = (F_{1,t}, \dots, F_{N_p,t})$, which corresponded to the fluorescence intensity at time t for each of the N_p pixels in the ROI (note that we use the \vec{X} throughout this section to indicate row vectors in space, versus \mathbf{X} to indicate column vectors in time). Second, at each time t , that vector

CHAPTER 1. FAST-OOPSI

was projected into a scalar, yielding F_t , the assumed input to the filter. In this section, the optimal projection is determined by considering a more general model:

$$F_{x,t} = \alpha_x C_t + \beta_x + \sigma \varepsilon_{x,t}, \quad \varepsilon_{x,t} \stackrel{iid}{\sim} \mathcal{N}(0, 1) \quad (1.24)$$

where α_x scales each pixel, from which some number of photons are contributed due to calcium fluctuations, C_t , and others due to baseline fluorescence, β . Further, the noise is assumed to be both spatially and temporally white, with standard deviation, σ , in each pixel (this assumption can easily be relaxed, by modifying the covariance matrix of $\varepsilon_{x,t}$). Performing inference in this more general model proceeds in a nearly identical manner as before. In particular, the maximization, gradient, and Hessian become:

$$\hat{C}_z = \operatorname{argmax}_{MC \geq 0} -\frac{1}{2\sigma^2} \left\| \vec{F} - C\vec{\alpha} - \mathbf{1}_T \vec{\beta} \right\|_F^2 - (MC)^\top \lambda + z \log(MC)^\top \mathbf{1}, \quad (1.25)$$

$$\mathbf{g} = (\vec{F} - C\vec{\alpha} - \mathbf{1}_T \vec{\beta})^\top \frac{\vec{\alpha}^\top}{\sigma^2} - M^\top \lambda + z M^\top (MC)^{-1} \quad (1.26)$$

$$\mathbf{H} = -\frac{\vec{\alpha} \vec{\alpha}^\top}{\sigma^2} \mathbf{I} - z M^\top (MC)^{-2} M \quad (1.27)$$

where \vec{F} is an $N_p \times T$ element matrix, where $\mathbf{1}_T$ is a column vector of ones with length T , \mathbf{I} is an $N_p \times N_p$ identity matrix, and $\|x\|_F$ indicates the Frobenius norm, i.e. $\|x\|_F^2 = \sum_{i,j} x_{i,j}^2$. Note that to speed up computation, one can first project the $N_c \times T$ dimensional movie onto the spatial filter, $\vec{\alpha}$, yielding a one-dimensional time series, \mathbf{F} , reducing the problem to evaluating a $T \times 1$ vector norm, as in Eq. (1.15).

Typically, the parameters $\vec{\alpha}$ and $\vec{\beta}$ are unknown, and therefore must be estimated from the data. Following the strategy developed in the last section, we first initialize the parameters. Let the initial spatial filter be the median image frame, i.e., $\hat{\alpha}_x = \operatorname{median}_t(F_{x,t})$,

CHAPTER 1. FAST-OOPSI

and the initial offset be uniform, with magnitude equal to the total movie median, $\hat{\beta}_x = \text{median}_{x,t}(F_{x,t})$ for all x . Given these robust initializations, the maximum likelihood estimator for each α_x is given by:

$$\hat{\alpha}_x = \underset{\alpha_x}{\operatorname{argmax}} P[\mathbf{F}_x | \hat{\mathbf{C}}] = \underset{\alpha_x}{\operatorname{argmax}} \sum_t \log P[F_{x,t} | \hat{C}_t] \quad (1.28a)$$

$$= \underset{\alpha_x}{\operatorname{argmax}} \sum_t \left\{ -\frac{1}{2}(2\pi\sigma^2) - \frac{1}{2\sigma^2} \left(F_{x,t} - \alpha_x \hat{C}_t - \hat{\beta}_x \right)^2 \right\} = \underset{\alpha_x}{\operatorname{argmax}} \sum_t -(F_{x,t} - \alpha_x \hat{C}_t - \hat{\beta}_x)^2, \quad (1.28b)$$

which is solved by regressing $\hat{\mathbf{C}}$ onto $(\mathbf{F}_x - \hat{\beta}_x \mathbf{1}_T)$. In other words, by computing the gradient of Eq. (1.28b) with respect to α_x and setting to zero, one obtains (using Matlab notation): $\hat{\alpha}_x = \hat{\mathbf{C}} \setminus (\mathbf{F}_x - \hat{\beta}_x \mathbf{1}_T)$. Computing the gradient of Eq. (1.28) with respect to each $\hat{\beta}_x$, setting the result to zero, and solving for $\hat{\beta}_x$, yields:

$$\hat{\beta}_x = \frac{1}{T} \sum_{t=1}^T \frac{F_{x,t} - \hat{\alpha}_x \hat{C}_t}{\hat{\alpha}_x^2}. \quad (1.29)$$

Iterating these two steps results in a coordinate ascent approach to estimate $\vec{\alpha}$ and $\vec{\beta}$ [27]. As in the scalar F_t case, we iterate estimating the parameters of this model, $\boldsymbol{\theta} = \{\vec{\alpha}, \vec{\beta}, \sigma, \gamma, \lambda\}$, and the spike train, \mathbf{n} . Because of the free scale term discussed in section 1.2.4, the absolute magnitude of $\vec{\alpha}$ is not identifiable. Thus, convergence is defined here by the “shape” of the spike train converging, i.e., the norm of the difference between the inferred spike trains from subsequent iterations, both normalized such that $\max(\hat{n}_t) = 1$. In practice, this procedure converged after several iterations.

1.2.6 Overlapping spatial filters

It is not always possible to segment the movie into pixels containing only fluorescence from a single neuron. Therefore, the above model can be generalized to incorporate multiple neurons within an ROI. Specifically, letting the superscript i index the N_c neurons in this ROI yields:

$$\vec{F}_t = \sum_{i=1}^{N_c} \vec{\alpha}^i C_t^i + \vec{\beta} + \sigma \vec{\varepsilon}_t, \quad \vec{\varepsilon}_t \stackrel{iid}{\sim} \mathcal{N}(\mathbf{0}, \mathbf{I}) \quad (1.30)$$

$$C_t^i = \gamma^i C_{t-1}^i + n_t^i, \quad n_t^i \stackrel{iid}{\sim} \text{Poisson}(n_t^i; \lambda_i \Delta) \quad (1.31)$$

where each neuron is implicitly assumed to be independent, and each pixel is conditionally independent and identically distributed with standard deviation σ , given the underlying calcium signals. To perform inference in this more general model, let $\mathbf{1}$ and $\mathbf{0}$ correspond to an $N_c \times 1$ row vector of ones, and zeros, respectively, and $\mathbf{n}_t = [n_t^1, \dots, n_t^{N_c}]$, $\mathbf{C}_t = [C_t^1, \dots, C_t^{N_c}]$, and $\mathbf{\Gamma} = [-\gamma^1, \dots, -\gamma^{N_c}]^\top$, yielding:

$$\mathbf{M}\mathbf{C} = \begin{bmatrix} -\mathbf{\Gamma} & \mathbf{1} & \mathbf{0} & \mathbf{0} & \cdots & \mathbf{0} \\ \mathbf{0} & -\mathbf{\Gamma} & \mathbf{1} & \mathbf{0} & \cdots & \mathbf{0} \\ \vdots & \ddots & \ddots & \ddots & \ddots & \vdots \\ \mathbf{0} & \cdots & \mathbf{0} & -\mathbf{\Gamma} & \mathbf{1} & \mathbf{0} \\ \mathbf{0} & \cdots & \mathbf{0} & \mathbf{0} & -\mathbf{\Gamma} & \mathbf{1} \end{bmatrix} \begin{bmatrix} \mathbf{C}_1 \\ \mathbf{C}_2 \\ \vdots \\ \mathbf{C}_{T-1} \\ \mathbf{C}_T \end{bmatrix} = \begin{bmatrix} \mathbf{n}_1 \\ \mathbf{n}_2 \\ \vdots \\ \mathbf{n}_{T-1} \end{bmatrix}, \quad (1.32)$$

and proceed as above. Note that Eq. (1.32) is very similar to Eq. (1.14), except that \mathbf{M} is no longer tridiagonal, but rather, block tridiagonal (and \mathbf{C}_t and \mathbf{n}_t are vectors instead of scalars). Importantly, the Thomas algorithm, which is a simplified form of Gaussian

CHAPTER 1. FAST-OOPSI

elimination, finds the solution to linear equations with block tridiagonal matrices in linear time, so the efficiency gained from utilizing the tridiagonal structure above is maintained for this block tridiagonal structure [28].

If the parameters are unknown, they must be estimated. Define $\alpha_x = [\alpha_x^1, \dots, \alpha_x^{N_c}]^T$. Initialize $\vec{\beta}$ as above. To initialize $\vec{\alpha} = [\vec{\alpha}_1, \dots, \vec{\alpha}_{N_c}]$, the goal is to be able to represent the baseline subtracted matrix, $\vec{F} - \mathbf{1}_T \vec{\beta}$, as the sum of only N_c time-varying components, also known as a *low-rank* approximation. Singular value decomposition is a tool known to find the low-rank approximation to a matrix, with the smallest mean-square-error of all possible low-rank approximations [32]. Because the “singular values” are equivalent to the “principal components” of the covariance of the movie, a natural initial estimate for the N_c $\vec{\alpha}$ vectors are the N_c first principal components. While other methods to initialize the spatial filters (such as “independent component analysis” [33]) could also work, because fast algorithms for computing the first few principal components are readily available [34], PCA was both sufficiently effective and efficient. Given these initializations, estimating $\vec{\alpha}$ follows very similarly as in Eqs. (1.28):

$$\hat{\alpha}_x = \underset{\alpha_x}{\operatorname{argmin}} \sum_{t=1}^T \left(F_{x,t} - \hat{\beta}_x - \sum_{i=1}^{N_c} \alpha_x^i \hat{C}_t^i \right)^2 \quad (1.33)$$

where Eq. (1.33) is solved efficiently in Matlab exactly as in Eq. (1.28). Convergence of parameters and spike trains in this model behaved similarly to the scenario described in section 1.2.5, assuming the spikes were sufficiently uncorrelated and observations had a sufficiently high SNR.

1.2.7 Experimental Methods

1.2.7.1 Slice Preparation and Imaging

All animal handling and experimentation was done according to the National Institutes of Health and local Institutional Animal Care and Use Committee guidelines. Somatosensory thalamocortical or coronal slices 350-400 μm thick were prepared from C57BL/6 mice at age P14 as described [35]. Neurons were filled with 50 μM Oregon Green Bapta 1 hexapotassium salt (OGB-1; Invitrogen, Carlsbad, CA) through the recording pipette or bulk loaded with Fura-2 AM (Invitrogen, Carlsbad, CA). Pipette solution contained 130 mM K-methylsulfate, 2 mM MgCl_2 , 0.6 mM EGTA, 10 mM HEPES, 4 mM ATP-Mg, and 0.3 mM GTP-Tris, pH 7.2 (295 mOsm). After cells were fully loaded with dye, imaging was done by using a modified BX50-WI upright microscope (Olympus, Melville, NY). Image acquisition was performed with the C9100-12 CCD camera from Hamamatsu Photonics (Shizuoka, Japan) with arclamp illumination with excitation and emission bandpass filters at 480-500 nm and 510-550 nm, respectively (Chroma, Rockingham, VT) for Oregon Green. Imaging of Fura-2 loaded slices was performed with a confocal spinning disk (Solumere Technology Group, Salt Lake City, UT) and an Orca CCD camera from Hamamatsu Photonics (Shizuoka, Japan). Images were saved and analyzed using custom software written in Matlab (Mathworks, Natick, MA).

1.2.7.2 Electrophysiology

All recordings were made using the Multiclamp 700B amplifier (Molecular Devices, Sunnyvale, CA), digitized with National Instruments 6259 multichannel cards and recorded using custom software written using the LabView platform (National Instruments, Austin, TX) . Square pulses of sufficient amplitude to yield the desired number of action potentials were given as current commands to the amplifier using the LabView and National Instruments system.

1.2.7.3 Fluorescence preprocessing

Traces were extracted using custom Matlab scripts to (i) segment the mean image into ROIs, and then (ii) average all the pixels within the ROI. The Fura-2 fluorescence traces were inverted. As some slow drift was sometimes present in the traces, each trace was Fourier transformed, and all frequencies below 0.5 Hz were set to zero (0.5 Hz was chosen by eye), and the resulting fluorescence trace was then normalized to be between zero and one.

1.3 Results

1.3.1 Main Result

The main result of this paper is that the fast filter can find the approximately most likely spike train, \hat{n} , very efficiently, and that this approach yields more accurate spike train estimates than optimal linear deconvolution. Fig. 1.2 depicts a simulation showing this result. Clearly, the fast filter’s inferred “spike train” (third panel) more closely resembles the true spike train (second panel) than the optimal linear deconvolution’s inferred spike train (bottom panel; Wiener filter). Note that neither filter results in an integer sequence, but rather, each infers a real number at each time.

The Wiener filter implicitly approximates the Poisson spike rate with a Gaussian spike rate (see Appendix A.2 for details). A Poisson spike rate indicates that in each frame, the number of possible spikes is an integer, 0, 1, 2, The Gaussian approximation, however, allows for any real number of spikes in each frame, including both partial spikes, e.g., 1.4, and *negative* spikes, e.g., -0.8. While a Gaussian well approximates a Poisson distribution when rates are about 10 spikes per frame, this example is very far from that regime, so the Gaussian approximation performs relatively poorly. More specifically, the Wiener filter exhibits a “ringing” effect. Whenever fluorescence drops rapidly, the most likely underlying signal is a proportional drop. Because the Wiener filter does not impose a non-negative constraint on the underlying signal (which, in this case, is a spike train), it infers such a drop. After such a drop has been inferred, since no corresponding drop

CHAPTER 1. FAST-OOPSI

occurred in the true underlying signal here, a complementary jump is often then inferred, to “re-align” the inferred signal with the observations. This oscillatory behavior results in poor inference quality. The non-negative constraint imposed by the fast filter prevents this because the underlying signal never drops below zero, so the complementary jump never occurs either.

The inferred “spikes”, however, are still not binary events when using the fast filter. This is a by-product of approximating the Poisson distribution on spikes with an exponential (cf. Eq. (1.11a)), because the exponential is a *continuous* distribution, versus the Poisson, which is discrete. The height of each spike is therefore proportional to the inferred calcium jump size, and can be thought of as a proxy for the confidence with which the algorithm believes a spike occurred. Importantly, by utilizing the Gaussian elimination and interior-point methods, as described in the Methods section, the computational complexity of fast filter is the same as an efficient implementation of the Wiener filter.

Although in Figure 1.2 the model parameters were provided, in the general case, the parameters are unknown, and must therefore be estimated from the observations (as described in section 1.2.4). Importantly, this algorithm does not require “training” data, i.e., there is no need for joint imaging and electrophysiological experiments to estimate the parameters governing the relationship between the two. Figure 1.3 shows another simulated example; in this example, however, the parameters are estimated from the observed fluorescence trace alone. Again, it is clear that the fast filter far outperforms the Wiener filter.

Given the above two results, the fast filter was applied to real data. More specifically, by

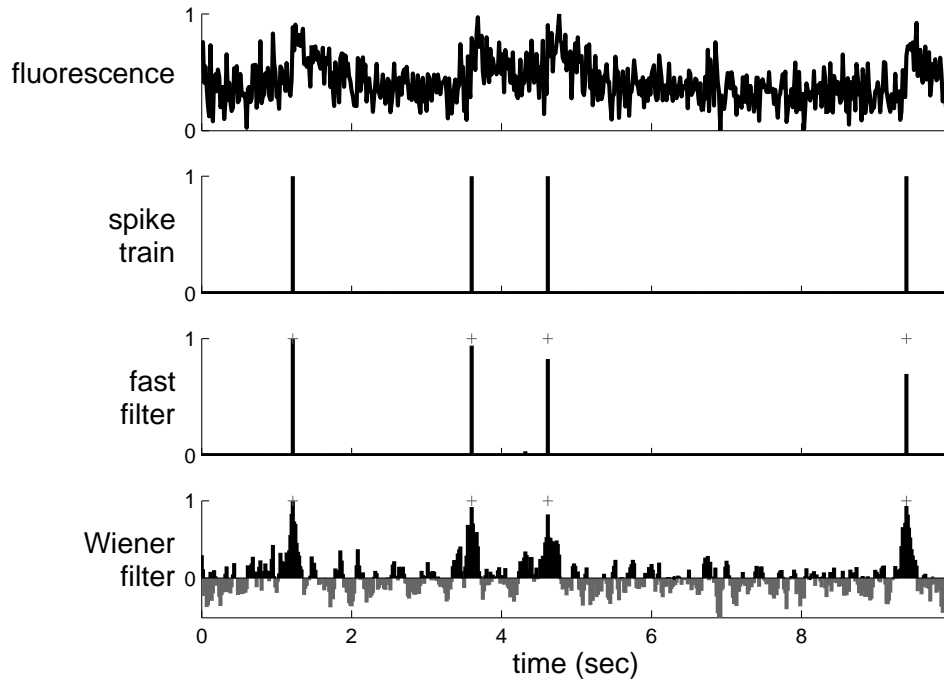


Figure 1.2: The fast filter’s inferred spike train is significantly more accurate than the output of the optimal linear deconvolution (Wiener filter) on typical simulated data. Note that neither filter constrains the inference to be a sequence of integers; rather, the fast filter relaxes the constraint to allow all non-negative numbers, and the Wiener filter allows for all real numbers. The restriction of the fast filter to exclude negative numbers eliminates the ringing effect seen in the Wiener filter output, resulting in a much cleaner inference. Note that the magnitude of the inferred spikes in the fast filter output is proportional to the inferred calcium jump size. Top panel: fluorescence trace. Second panel: spike train. Third panel: fast filter inference. Bottom panel: Wiener filter inference. Note that the gray bars in the bottom panel indicate *negative* spikes. Black ‘+’s in bottom two panels indicate true spike times. Simulation details: $T \approx 3000$ time steps, $\Delta = 5$ msec, $\alpha = 1$, $\beta = 0$, $\sigma = 0.3$, $\tau = 1$ sec, $\lambda = 1$ Hz. Conventions for other figures as above, unless otherwise indicated.

jointly recording electrophysiologically and imaging, the true spike times are known, and the accuracy of the two filters can be compared. Figure 1.4 shows a result typical of the 12 joint electrophysiological and imaging experiments conducted. Although it is difficult to see in this figure, the first four “events” are actually pairs of spikes, which is reflected by

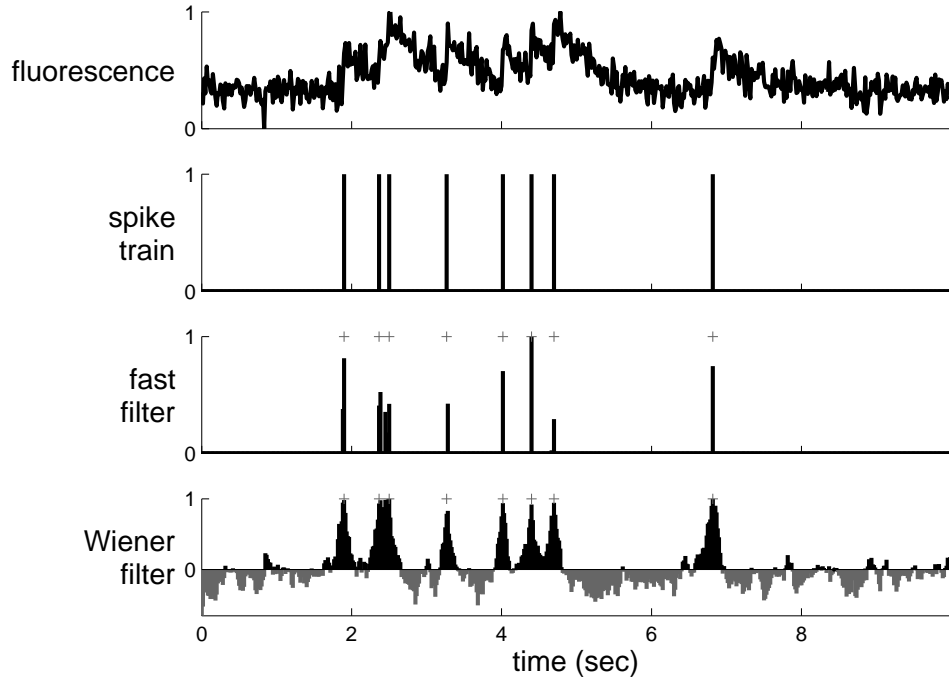


Figure 1.3: The fast filter significantly outperforms the Wiener filter, even when the parameters unknown. For both filters, the appropriate parameters were estimated using only the data shown above, unlike Figure 1.2, in which the true parameters were provided to the filters. Simulation details as in Figure 1.2.

the width and height of the corresponding inferred spikes when using the fast filter. This suggests that although the scale of n is arbitrary, the fast filter can correctly ascertain the number of spikes within spike events.

Figure 1.5 further evaluates this claim. While recording and imaging, the cell was forced to spike once, twice, or thrice, for each spiking event. Naïvely, this would suggest that an algorithm based on a purely linear model would struggle to resolve spike fidelity in this high frequency spiking regime. However, the fast filter infers the correct number of spikes in each event. On the contrary, there is no obvious way to count the number of

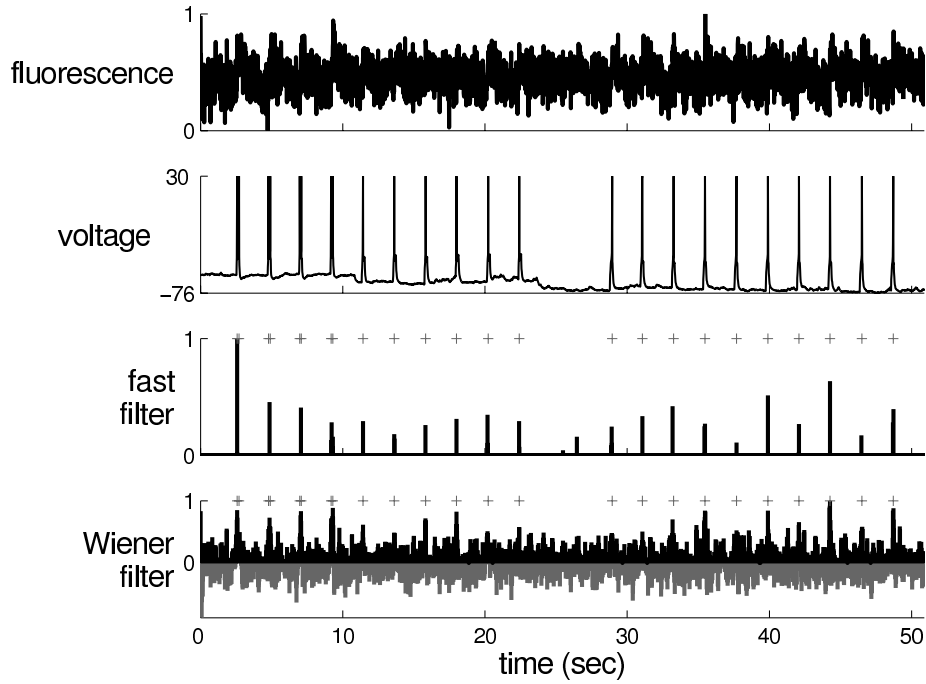


Figure 1.4: The fast filter significantly outperforms the Wiener filter on typical *in vitro* data, using OGB-1. Note that all the parameters for both filters were estimated only from the fluorescence data in the top panel (ie, not considering the voltage data at all). Again, '+'s denote true spike times extracted from the patch data, not inferred spike times from F .

spikes within each event when using the Wiener filter.

1.3.2 Online analysis of spike trains using the fast filter

A central aim for this work was the development of an algorithm that infers spikes fast enough to use online while imaging a large population of neurons (eg, ≈ 100). Figure 1.6 shows a segment of the results of running the fast filter on 136 neurons, recorded simultaneously, as described in section 1.2.7. Note that the filtered fluorescence signals show

CHAPTER 1. FAST-OOPSI

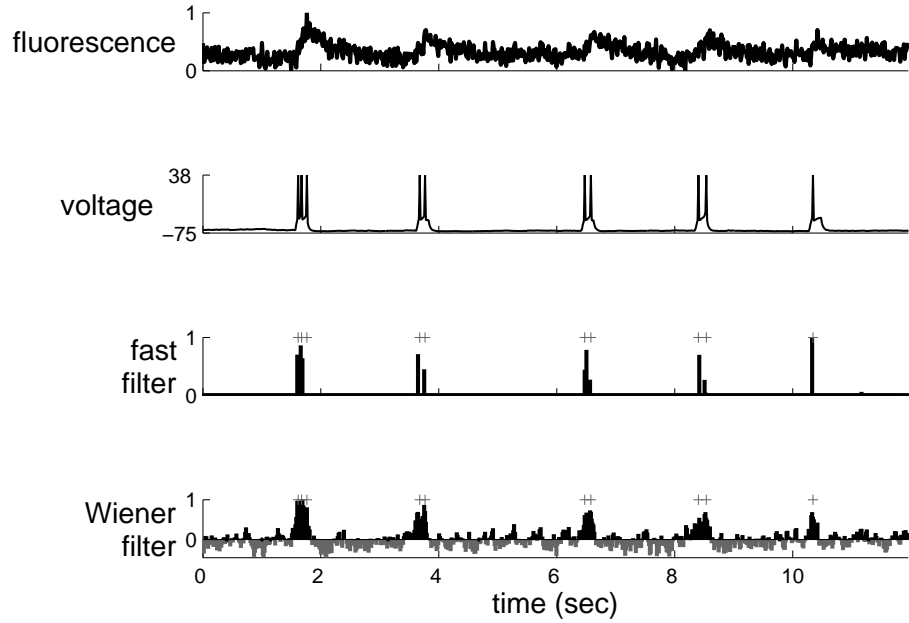


Figure 1.5: The fast filter can often resolve the correct number of spikes within each spiking event, while imaging using OGB-1, given sufficiently high SNR. It is difficult, if not impossible, to count the number of spikes given the Wiener filter output. Recording and fitting parameters as in Figure 1.4. Note that the parameters were estimated using a 60 sec long recording, of which only a fraction is shown here, to more clearly depict the number of spikes per event.

fluctuations in spiking much more clearly than the unfiltered fluorescence trace. These spike trains were inferred in less than imaging time, meaning that one could infer spike trains for the past experiment while conducting the subsequent experiment. More specifically, a movie with 5,000 frames of 100 neurons can be analyzed in about ten seconds on a standard desktop computer. Thus, if that movie was recorded at 50 Hz, while collecting the data required 100 seconds, inferring spikes only required ten seconds, a ten-fold improvement over real-time.

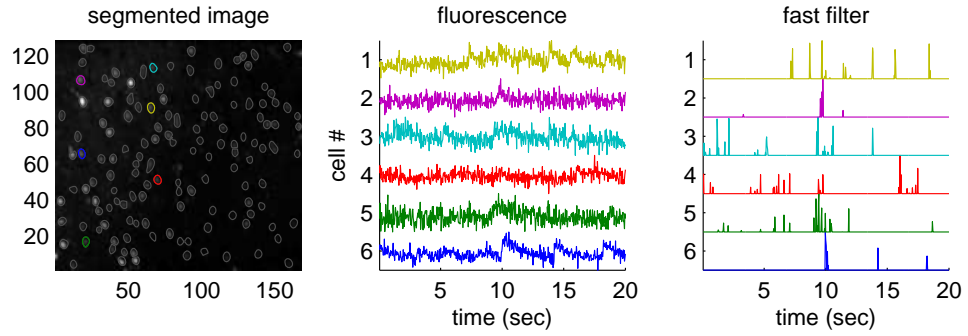


Figure 1.6: The fast filter infers spike trains from a large population of neurons imaged simultaneously *in vitro*, using Fura-2, faster than real-time. Specifically, inferring the spike trains from this 400 sec long movie including 136 neurons requires only about 40 sec on a standard laptop computer. The inferred spike trains much more clearly convey neural activity than the raw fluorescence traces. Although no intracellular “ground truth” is available on this population data, the noise seems to be reduced, consistent with the other examples with ground truth. Left panel: Mean image field, segmented into ROIs each containing a single neuron. Middle panel: example fluorescence traces. Right panel: fast filter output corresponding to each associated trace. Note that neuron identity is indicated by color across the three panels.

1.3.3 Extensions

Section 2.2 describes a simple principled first-order model relating the spike trains to the fluorescence trace. A number of the simplifying assumptions can be straightforwardly relaxed, as described below.

1.3.3.1 Replacing Gaussian observations with Poisson

In the above, observations were assumed to have a Gaussian distribution. The statistics of photon emission and counting, however, suggest that a Poisson distribution would be

CHAPTER 1. FAST-OOPSI

more natural, especially for two-photon data [36], yielding:

$$F_t \stackrel{iid}{\sim} \text{Poisson}(\alpha C_t + \beta). \quad (1.34)$$

One additional advantage to this model over the Gaussian model, is that the variance parameter, σ^2 , no longer exists, which might make learning the parameters simpler. Importantly, the log-posterior is still concave in \mathbf{C} , as the prior remains unchanged, and the new log-likelihood term is a sum of terms concave in \mathbf{C} :

$$\log P[\mathbf{F}|\mathbf{C}] = \sum_{t=1}^T \log P[F_t|C_t] = \sum_{t=1}^T \{F_t \log(\alpha C_t + \beta) - (\alpha C_t + \beta) - \log(F_t!)\}. \quad (1.35)$$

The gradient and Hessian of the log-posterior can therefore be computed analytically by substituting the above likelihood terms for those implied by Eq. (1.1). In practice, however, modifying the filter for this model extension did not seem to significantly improve inference results in any simulations or data (not shown).

1.3.3.2 Allowing for a time-varying prior

In Eq. (1.4), the rate of spiking is a constant. Often, additional knowledge about the experiment, including external stimuli, or other neurons spiking, can provide strong time-varying prior information [18]. A simple model modification can incorporate that feature:

$$n_t \stackrel{iid}{\sim} \text{Poisson}(\lambda_t \Delta), \quad (1.36)$$

where λ_t is now a function of time. Approximating this time-varying Poisson with a time-varying exponential with the same time-varying mean (similar to Eq. (1.11a)), and letting

$\lambda = [\lambda_1, \dots, \lambda_T]^\top \Delta$, yields an objective function identical to Eq. (1.15), so log-concavity is maintained, and the same techniques may be applied. However, as above, this model extension did not yield any significantly improved filtering results (not shown).

1.3.3.3 Saturating fluorescence

Although all the above models assumed a *linear* relationship between F_t and C_t , the relationship between fluorescence and calcium is typically better approximated by the non-linear Hill equation [30]. Modifying Eq. (1.1) to reflect this change yields:

$$F_t = \alpha \frac{C_t}{C_t + k_d} + \beta + \sigma \varepsilon_t, \quad \varepsilon_t \stackrel{iid}{\sim} \mathcal{N}(0, 1). \quad (1.37)$$

Importantly, log-concavity of the posterior is no longer guaranteed in this nonlinear model, meaning that converging to the global maximum is no longer guaranteed. Assuming a good initialization can be found, however, if this model is more accurate, then ascending the gradient for this model might yield improved inference results. In practice, initializing with the inference from the fast filter assuming a linear model (eg, Eq. (1.30)) often resulted in nearly equally accurate inference, but inference assuming the above nonlinearity was far less robust than the inference assuming the linear model (not shown).

1.3.3.4 Using the fast filter to initialize the sequential Monte Carlo filter

A sequential Monte Carlo (SMC) method to infer spike trains can incorporate this saturating nonlinearity, as well as the other model extensions discussed above [18]. However, this SMC filter is not nearly as computationally efficient as the fast filter proposed here. Like the fast filter, the SMC filter estimates the model parameters in a completely unsupervised fashion, i.e., from the fluorescence observations, using an expectation-maximization algorithm (which requires iterating between computing the expected value of the hidden variables — C and n — and updating the parameters). In [18], parameters for the SMC filter were initialized based on other data. While effective, this initialization was often far from the final estimates, and therefore, required a relatively large number of iterations (eg, 20–25) before converging. Thus, it seemed that the fast filter could be used to obtain an improvement to the initial parameter estimates, given an appropriate rescaling to account for the nonlinearity, thereby reducing the required number of iterations to convergence. Indeed, Figure 1.7 shows how the SMC filter outperforms the fast filter on biological data, and only required 3–5 iterations to converge on this data, given the initialization from the fast filter (which was typical). Note that the first few events of the spike train are individual spikes, resulting in relatively small fluorescence fluctuations, whereas the next events are actually spike doublets or triplets, causing a much larger fluorescence fluctuation. Only the SMC filter picks up the individual spikes in this trace, a result typical when the effective signal-to-noise ratio (SNR) is poor. Thus, these two inference algorithms are complemen-

CHAPTER 1. FAST-OOPSI

tary: the fast filter can be used for rapid, online inference, and for initializing the SMC filter, which can then be used to further refine the spike train estimate. Importantly, although the SMC filter often outperforms the fast filter, the fast filter is more robust, meaning that it more often works “out-of-the-box.”

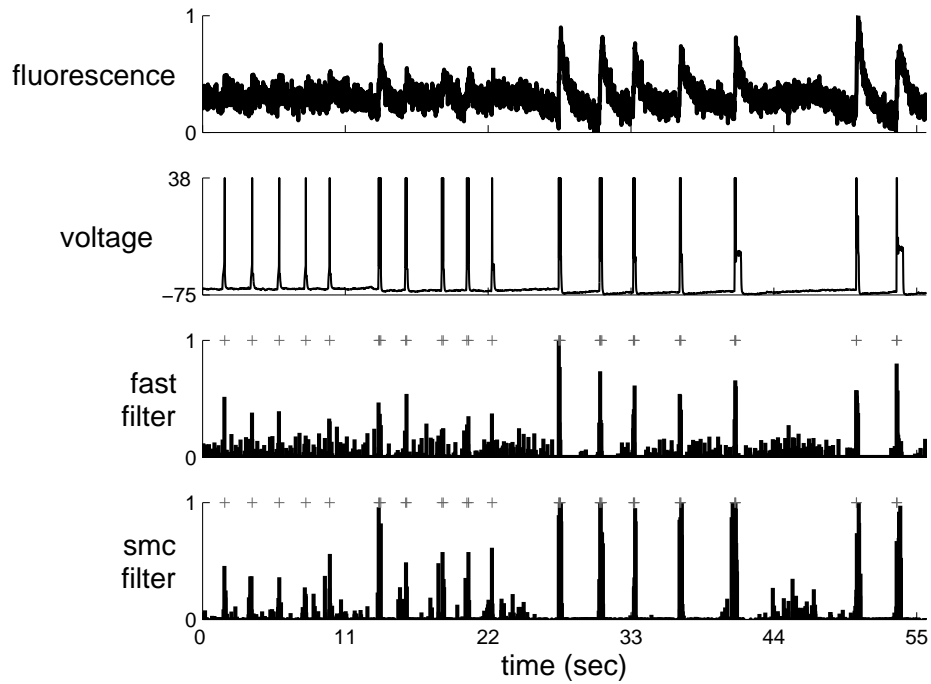


Figure 1.7: The fast filter effectively initializes the parameters for the SMC filter, significantly reducing the number of expectation-maximization iterations to convergence, on typical *in vitro* data, using OGB-1. Note that while the fast filter clearly infers the spiking events in the end of the trace, those in the beginning of the trace are less clear. On the other hand, the SMC filter more clearly separates non-spiking activity from true spikes. Also note that the ordinate on the bottom panel corresponds to the inferred probability of a spike having occurred in each frame.

1.3.4 Spatial filter

In the above, the filters operated on one-dimensional fluorescence traces. Typically, the data are time-series of images which are first segmented into regions-of-interest (ROI), and then (usually) averaged to obtain F_t . In theory, one could improve the effective SNR of the fluorescence trace by scaling each pixel relative to one another. In particular, pixels not containing any information about calcium fluctuations can be ignored, and pixels that are partially anti-correlated with one another could have weights with opposing signs.

Figure 1.8 demonstrates the potential utility of this approach. The top row shows different depictions of an ROI containing a single neuron. On the far left panel is the true spatial filter for this neuron. This particular spatial filter was chosen based on experience analyzing both *in vitro* and *in vivo* movies; often, it seems that the pixels immediately around the soma are anti-correlated with those in the soma. This effect is possibly due to the influx of calcium from the extracellular space immediately around the soma. The simulated movie (not shown) is relatively noisy, as indicated by the second panel, which depicts an exemplary image frame. The standard approach, given such a noisy movie, would be to first segment the movie to find an ROI corresponding to the soma of this cell, and then spatially average all the pixels found to be within this ROI. The third panel shows this standard “boxcar spatial filter”. The fourth panel shows the mean frame. Clearly, this mean frame is very similar to the true spatial filter.

The bottom panels of Figure 1.8 depict the effect of using the true spatial filter, versus the typical one. The left side shows the fluorescence trace and its associated spike inference

CHAPTER 1. FAST-OOPSI

obtained from using the typical spatial filter. The right side shows the same when using the true spatial filter. Clearly, the true spatial filter results in a much cleaner fluorescence trace and spike inference. When the true spatial filter is a single Gaussian, the boxcar spatial filter works about as well as the true spatial filter (not shown).

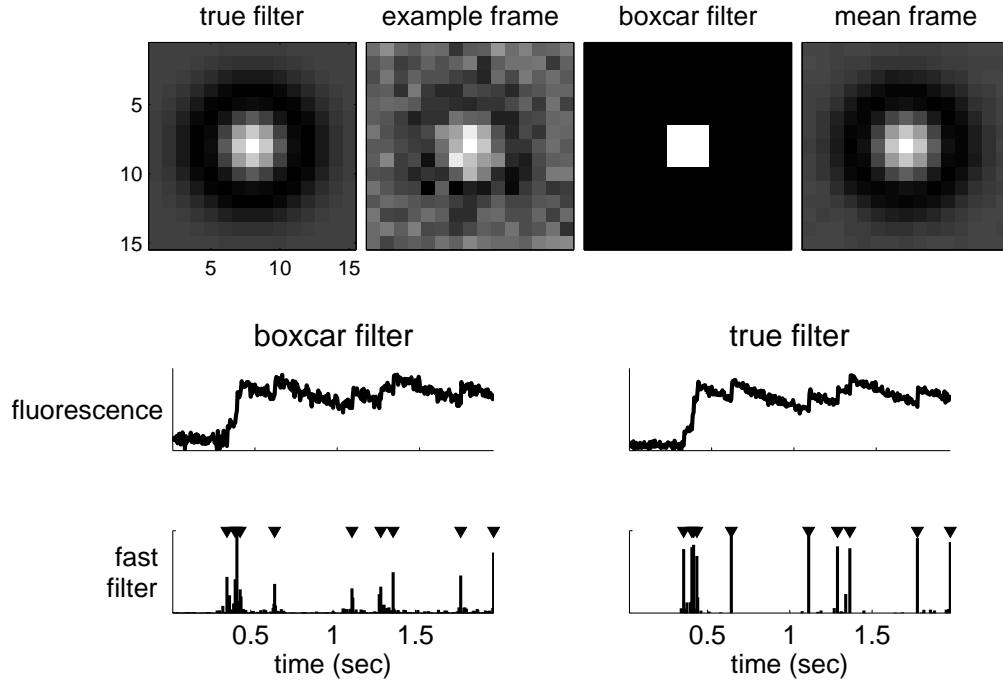


Figure 1.8: A simulation demonstrating that using a better spatial filter can significantly enhance the effective SNR. The true spatial filter was a difference of Gaussians: a positively weighted Gaussian of small width, and a negatively weighted Gaussian with larger width (both with the same center). Top row far left: true spatial filter. Top row second from left: example movie frame. Top row second from right: typical spatial filter. Top row far right: mean frame. Middle row left: fluorescence trace using the boxcar spatial filter. Bottom row left: fast filter output using the boxcar spatial filter. Middle row right: fluorescence trace using true spatial filter. Bottom right: fast filter output using true spatial filter. Simulation details: $\vec{\alpha} = \mathcal{N}(\mathbf{0}, 2\mathbf{I}) - 1.1\mathcal{N}(\mathbf{0}, 2.5\mathbf{I})$ where $\mathcal{N}(\boldsymbol{\mu}, \boldsymbol{\Sigma})$ indicates a two-dimensional Gaussian with mean $\boldsymbol{\mu}$ and covariance matrix $\boldsymbol{\Sigma}$, $\vec{\beta} = \mathbf{0}$, $\tau = 0.85$ sec, $\lambda = 5$ Hz.

1.3.5 Overlapping spatial filters

The above shows that if a ROI contains only a single neuron, the effective SNR can be enhanced by spatially filtering. However, this analysis assumes that only a single neuron is in the ROI. Often, ROIs are overlapping, or nearly overlapping, making the segmentation problem more difficult. Therefore, it is desirable to have an ability to crudely segment, yielding only a few neurons in each ROI, and then spatially filter within each ROI to pick out the spike trains from each neuron. This may be achieved in a principled manner by generalizing the model as described in section 1.2.6. Figure 1.9 shows how this approach can separate the two signals, assuming that the spatial filters of the two neurons are known.

Typically, the true spatial filters of the neurons in the ROI will be unknown, and thus, must be estimated from the data. This problem may be considered a special case of blind source separation [33, 37]. Figure 1.10 shows that multiple signals can be separated, with reasonable assumptions on correlations between the signals, and SNR. Note that separation occurs even though the signal is overlapping in several pixels (top left panel), leading to a “bleed-through” effect in the one-dimensional fluorescence projections (bottom left panel). The inferred filters (top middle and right panels) are not the true filters, but rather, their sum is linearly related to the sum of the true filters. Regardless, the inferred spike trains are well separated (bottom middle and right panels).

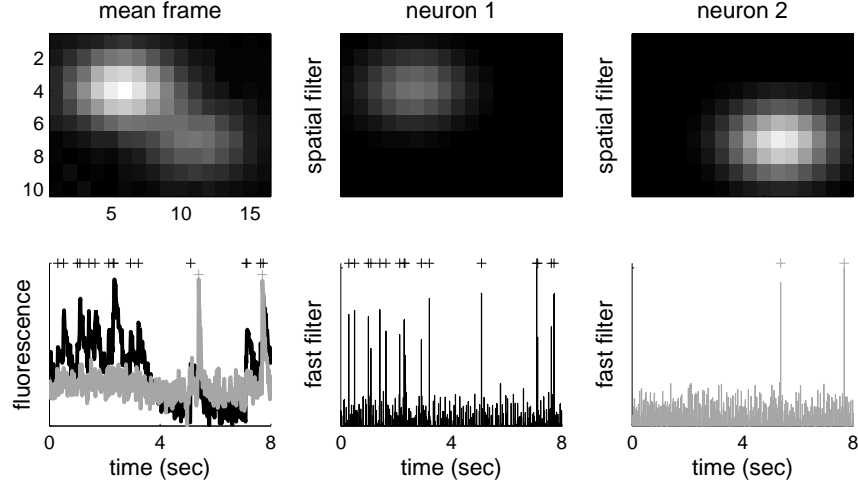


Figure 1.9: Simulation showing that even when two neurons’ spatial filters are overlapping, one can separate the two spike trains by spatial filtering. Top left panel: mean frame from the movie. Bottom left: optimal one-dimensional fluorescence projections for the neuron 1 (black line) and neuron 2 (gray line), and their respective spike trains (black and gray ‘+’ symbols, respectively). Top middle panel: the true spatial filter for neuron 1. Bottom middle panel: inferred (black line) and true (black ‘+’ symbols) spike trains. Top right panel: the true spatial filter for neuron 2. Bottom right panel: inferred (gray line) and true (gray ‘+’ symbols) spike trains. Simulation details: $\vec{\alpha}^1 = \mathcal{N}([-1.8, 1.8]^\top, 2\mathbf{I})$ $\vec{\alpha}^2 = \mathcal{N}([1.8, -1.8]^\top, 5\mathbf{I})$, $\vec{\beta} = \mathbf{0}$, $\tau = [0.5, 0.5]^\top$ sec, $\lambda = [1.5, 1.5]^\top$ Hz.

1.4 Discussion

This work describes an algorithm that approximates the *maximum a posteriori* (MAP) spike train, given a calcium fluorescence movie. The approximation is required because finding the actual MAP estimate is not currently computationally tractable. Replacing the assumed Poisson distribution on spikes with an exponential distribution yields a log-concave optimization problem, which can be solved using standard gradient ascent techniques (such as Newton-Raphson). This exponential distribution has an advantage over a Gaussian distribution by restricting spikes to be positive, which improves inference quality (cf. Figure 1.2), and is a better approximation to a Poisson distribution with low rate.

CHAPTER 1. FAST-OOPSI

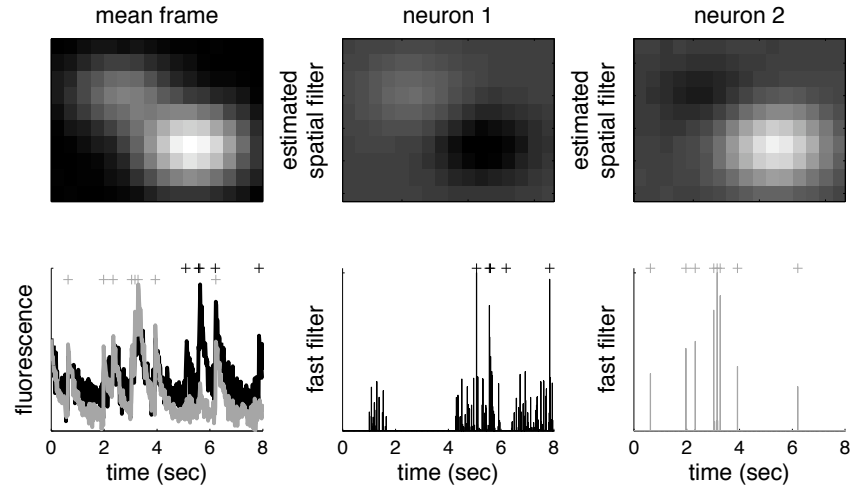


Figure 1.10: Simulation showing that even when two neurons’ spatial filters are largely overlapping, spatial filters that together are linearly related to the true spatial filters can be inferred, to separate the two signals. Simulation details as above. Note that the spatial fields are sufficiently overlapping to cause significant “bleed-through” between the two signals. In particular, this is clear from the rise in the black line in the first few seconds of the bottom left panel, which should be fluorescence due to neuron 1, but is in fact due to spiking from neuron 2. Regardless, the spike trains are accurately inferred here. Simulation parameters as in Figure 1.9.

Furthermore, by utilizing the special banded structure of the Hessian matrix of the log-posterior, this approximate MAP spike train can be inferred fast enough on standard computers to use it for online analyses. Finally, all the parameters can be estimated from only the fluorescence observations, obviating the need for joint electrophysiology and imaging (cf. Figure 1.3). This approach is robust, in that it works “out-of-the-box” on all the *in vivo* and *in vitro* data analyzed (cf. Figure 1.4).

Ideally, one could compute the full joint posterior of entire spike trains, conditioned on the fluorescence data. This distribution is analytically intractable, due to the Poisson assumption on spike trains. A Bayesian approach could use Markov Chain Monte Carlo methods to recursively sample spikes until a whole sample spike train is obtained [38,

CHAPTER 1. FAST-OOPSI

39]. Because a central aim here was computational expediency, a “greedy” approach is natural: i.e., recursively sample the most likely spike, update the posterior, and repeat until the posterior stops increasing. Template matching, projection pursuit regression [40], and matching pursuit [41] are examples of such a greedy approach (Greenberg et al’s algorithm [15] could also be considered a special case of such a greedy approach). Both the greedy methods, and the one developed here, aim to optimize a similar objective function. While greedy methods reduce the computational burden by restricting the search space of spike trains, here analytic approximations are made. The advantage of the greedy approaches relative to this one is that they result in a spike train (ie, a binary sequence). However, because of the numerical approximations and restrictions, one can never be sure whether the algorithm finds the *most* likely possible spike train. On the other hand, the approach developed herein is guaranteed to quickly find the most likely spike “train”, but now the inferred spike train allows for partial spikes. One interesting future direction might be to explore whether greedy methods could be improved by initializing with a thresholded version of the fast filter output.

Further, the fast filter is based on a biophysical model capturing key features of the data, and may therefore be straightforwardly generalized in several ways to improve accuracy. Unfortunately, some of these generalizations do not improve inference accuracy, perhaps because of the exponential approximation. Instead, the fast filter output can be used to initialize the more general SMC filter [18], to further improve inference quality (cf. Figure 1.7). Another model generalization allows incorporation of spatial filtering of the raw

CHAPTER 1. FAST-OOPSI

movie into this approach (cf. Figure 1.8).

A number of extensions follow from this work. First, pairing this filter with a crude but automatic segmentation tool to obtain ROIs would create a completely automatic algorithm that converts raw movies of populations of neurons into populations of spike trains. Second, combining this algorithm with recently developed connectivity inference algorithms on this kind of data [39], could yield very efficient connectivity inference.

Appendix A

Wiener filter

APPENDIX A. WIENER FILTER

A.1 Pseudocode

ass

APPENDIX A. WIENER FILTER

Algorithm 1 Pseudocode for inferring the approximately most likely spike train, given fluorescence data. Note that $\xi_i \ll 1$ for $i \in \{1, 2\}$; the algorithm is robust to small variations in each. The equations listed below refer to the most general equations in the text (simpler equations could be substituted when appropriate). Curly brackets, $\{\cdot\}$, indicate comments.

- 1: initialize parameters, θ (section 1.2.4.1)
 - 2: **while** convergence criteria not met **do**
 - 3: **for** $z = 1, 0.1, 0.01, \dots, \xi_1$ **do** $\{\text{interior point method to find } \widehat{C}\}$
 - 4: Initialize $n_t = \xi_2$ for all $t = 1, \dots, T$, $C_1 = 0$ and $C_t = \gamma C_{t-1} + n_t$ for all $t = 2, \dots, T$.
 - 5: let C_z be the initialized calcium, and \mathcal{P}_z , be the posterior given this initialization
 - 6: **while** $\mathcal{P}_{z'} < \mathcal{P}_z$ **do** $\{\text{Newton-Raphson with backtracking line searches}\}$
 - 7: compute g using Eq. (1.26)
 - 8: compute H using Eq. (1.27)
 - 9: compute d using $H \backslash g$ $\{(\text{block-}) \text{tridiagonal Gaussian elimination}\}$
 - 10: let $C_{z'} = C_z + s d$, where s is between 0 and 1, and $\mathcal{P}_{z'} > \mathcal{P}_z$ $\{\text{backtracking line search}\}$
 - 11: **end while**
 - 12: **end for**
 - 13: check convergence criteria
 - 14: update $\vec{\alpha}$ using Eq. (1.33) $\{\text{only if spatial filtering}\}$
 - 15: update $\vec{\beta}$ using Eq. (1.29)
 - 16: let σ be the root-mean square of the residual
 - 17: let $\lambda = \frac{1}{T} \sum_t \widehat{n}_t$
 - 18: **end while**
-

A.2 Wiener Filter

The Poisson distribution in Eq. (1.4) can be replaced with a Gaussian instead of a Poisson distribution, ie, $n_t \stackrel{iid}{\sim} \mathcal{N}(\lambda\Delta, \lambda\Delta)$, which, when plugged into Eq. (1.7) yields:

$$\hat{\mathbf{n}} = \underset{n_t}{\operatorname{argmax}} \sum_{t=1}^T \left(\frac{1}{2\sigma^2} (F_t - \alpha C_t - \beta)^2 + \frac{1}{2\lambda\Delta} (n_t - \lambda\Delta)^2 \right). \quad (\text{A.1})$$

Note that since fluorescence integrates over Δ , it makes sense that the mean scales with Δ . Further, since the Gaussian here is approximating a Poisson with high rate [36], the variance should scale with the mean. Using the same tridiagonal trick as above, Eq. (1.11b) can be solved using Newton-Raphson once (because this expression is quadratic in \mathbf{n}). Writing the above in matrix notation, substituting $C_t - \gamma C_{t-1}$ for n_t , and letting $\alpha = 1$ yields:

$$\hat{\mathbf{C}} = \underset{\mathbf{C}}{\operatorname{argmax}} -\frac{1}{2\sigma^2} \|\mathbf{F} - \mathbf{C} - \beta \mathbf{1}_T\|^2 - \frac{1}{2\lambda\Delta} \|\mathbf{M}\mathbf{C} - \lambda\Delta \mathbf{1}\|^2, \quad (\text{A.2})$$

which is quadratic in \mathbf{C} . The gradient and Hessian are given by:

$$\mathbf{g} = -\frac{1}{\sigma^2}(\mathbf{C} - \mathbf{F} - \beta \mathbf{1}_T) - \frac{1}{\lambda\Delta}((\mathbf{M}\hat{\mathbf{C}})^\top \mathbf{M} + \lambda\Delta \mathbf{M}^\top \mathbf{1}), \quad (\text{A.3})$$

$$\mathbf{H} = \frac{1}{\sigma^2} \mathbf{I} + \frac{1}{\lambda\Delta} \mathbf{M}^\top \mathbf{M}. \quad (\text{A.4})$$

Note that this solution is the optimal linear solution, under the assumption that spikes follow a Gaussian distribution, and is often referred to as the Wiener filter, regression with a smoothing prior, or ridge regression [27]. Estimating the parameters for this model follows similarly as described in section 1.2.4.

Chapter 2

smc-oopsi: a sequential Monte Carlo expectation-maximization algorithm for inferring the posterior mean spike train¹

2.1 Introduction

Recently, advances in the development of calcium indicators, delivery techniques, and microscopy technologies have facilitated imaging a wide array of preparations [4]. In particular, calcium sensitive organic dyes [42,43] have been targeted to populations of neurons both *in vivo* and *in vitro* using bulk loading [43–45] and electroporation [7, 46]. Similarly, viral infection, transgenics, and knock-ins have been used to genetically target neurons

¹Note that the data in this chapter was collected by Brendon O. Watson in Rafael Yuste’s laboratory

CHAPTER 2. SMC-OOPSI

with fluorescent proteins [47–49] . In conjunction with the development of improved calcium indicators and loading techniques, the advent of 2-photon microscopy now enables the visualization of neurons deep within scattering tissue [50–53].

Thus, using calcium sensitive fluorescence to study neural dynamics is becoming increasingly popular in a wide variety of neural substrates, including individual spines [54–57], dendrites [58–60], boutons [61, 62], neurons [63–65], and populations of neurons [5–7, 43, 66–72]. While the data collected from these experiments are fluorescence movies, the signals of interest are the precise spike times and/or the intracellular calcium concentrations, $[Ca^{2+}]$, of the observable neurons.

Inferring the spike trains and calcium concentrations from a fluorescence signal, however, is a difficult problem for a number of reasons. First, observations are noisy. This is a problem unlikely to be solved in the near future, as a major noise source is photon shot noise [36], which reflects the quantal nature of light emission and detection. Second, observations may have poor temporal resolution. While this problem may be partially mitigated by faster cameras and scanning systems [53, 73–75], faster imaging tends to exacerbate the noise problem, as fewer photons can be collected per image frame [36]. Third, the relationship between fluorescence observations and $[Ca^{2+}]$ is nonlinear, especially for fluorescent proteins [30, 76]. This has placed undesirable and unnecessary restrictions on the calcium indicators used for analysis, as the standard analytical tools assume a linear relationship between $[Ca^{2+}]$ and fluorescence [29, 36, 77, 78] (though see [79] for an exception). Fourth, the parameters governing the calcium and fluorescence dynamics are typically unknown a

CHAPTER 2. SMC-OOPSI

priori, and must be inferred from the data.

Nevertheless, there has been some significant recent progress. For instance, Smetters et al. [5] demonstrated reliable detection of single action potentials and spike trains by imaging bulk loaded fluorescent calcium dyes *in vitro*. Kerr et al. [80] — motivated by the observation that neurons in the rat motor and somatosensory cortices exhibit sparse spiking — developed a custom template-matching algorithm to detect the presence of single spikes *in vivo* using only fluorescence signals (and more recently further refined this approach [15]). The following year, Yaksi and Friedrich [29] — aided by the observation that neurons in the intact zebrafish olfactory bulb tend to respond to different odors with different time-varying firing rates — developed a linear smoothing convolution kernel that effectively inferred the time varying firing rate for an explant of an intact zebrafish brain. More recently, Sato et al. [71] designed a clustering algorithm using only *in vivo* calcium sensitive fluorescence signals to determine whether whisker stimulation successfully induced a spike. Earlier this year, Holekamp et al. [16] applied the optimal linear filter for deconvolving a fluorescence signal from anesthetized mice. Finally, Sasaki et al. developed a nonparametric approach to infer spikes from somatic calcium fluctuations [17].

The present work differs from previous efforts in several key aspects. We start by constructing a well defined probabilistic “forward model” of the signals of interest and the imaging process. Then, utilizing a sequential Monte Carlo expectation maximization framework, we design a particle filter smoother (PFS) to optimally infer the spike times and calcium transients, given the observed fluorescence signals and the model. Even for

relatively simple scenarios, the PFS outperforms optimal linear deconvolution by providing both a better inference and errorbars. The forward model may be generalized to account for a number of features present in typical data sets. Specifically, by incorporating saturation and signal dependent noise sources, we can perform inference on typical *in vitro* data sets. Furthermore, by allowing for intermittent observations (typical of 2-photon scanning experiments), we can perform superresolution inference, i.e., detect not just whether a spike occurs within a particular image frame, but also when within that frame the spike occurred. By also introducing stimulus and spike history dependence into the model, we can further refine our estimate. Moreover, estimating the parameters requires only a few seconds of fluorescence observations and a small number of spikes (e.g., 5 – 40), and does not require tedious simultaneous electrophysiology and imaging experiments. We close by discussing further generalizations of the model that may be required to apply a PFS to other experimental preparations, such as *in vivo* imaging. All code is available from the corresponding author upon request.

2.2 Model

The data sets of interest are sequences of images corresponding to the calcium sensitive fluorescence signals of some neural activity. We aim here to construct the simplest forward model that permits one to satisfactorily infer the spike trains and calcium transients underlying these images. By forward model, we mean a complete characterization of the proba-

CHAPTER 2. SMC-OOPSI

bility distributions governing the hidden dynamics and noisy observations, going “forward” from the spike train to the images. To infer the spike trains from the observations, we then invert our model. Below, we introduce a very simple model used to explain the mathematical formalism developed to infer the spike trains. Many of the simplifying assumptions are then relaxed in the Results section to improve our estimates when using *in vitro* data.

First, we assume a single-compartmental, equipotential model of the imaged neuron, over which the fluorescence signal may be spatially averaged, yielding a one-dimensional time varying fluorescence signal for each image frame, F_t . This assumption is justified by the observation that the calcium dynamics within the neuron are relatively fast [58, 81]. Next, we assume that the fluorescence at any time is a noisy linear function of $[\text{Ca}^{2+}]$ at that time:

$$F_t = \alpha[\text{Ca}^{2+}]_t + \beta + \sigma_F \varepsilon_{F,t}, \quad (2.1)$$

where α and β set the scale and offset for the fluorescence signal, respectively, σ_F is the standard deviation of the noise, and $\varepsilon_{.,t}$ denotes a standard normal Gaussian throughout this text.

Modeling $[\text{Ca}^{2+}]_t$ requires some additional assumptions. First, after each spike, $[\text{Ca}^{2+}]_t$ jumps instantaneously. This approximation is justified by the observation that calcium rise time is quick relative to the decay time [77, 82]. Second, each jump is the same size, A ; that is, for now we neglect $[\text{Ca}^{2+}]_t$ saturation effects due to channel inactivation and buffering [83]. Third, $[\text{Ca}^{2+}]_t$ decays exponentially with time constant τ , to a baseline calcium concentration, $[\text{Ca}^{2+}]_b$; i.e., we lump the myriad calcium extrusion and endogenous buffer-

CHAPTER 2. SMC-OOPSI

ing mechanisms and assume a single average time constant. Fourth, the $[\text{Ca}^{2+}]_t$ dynamics themselves have some Gaussian noise source, scaled by σ_c . Taken together, these assumptions imply the following model:

$$[\text{Ca}^{2+}]_t - [\text{Ca}^{2+}]_{t-1} = -\frac{\Delta}{\tau}([\text{Ca}^{2+}]_{t-1} - [\text{Ca}^{2+}]_b) + An_t + \sigma_c\sqrt{\Delta}\varepsilon_{c,t}, \quad (2.2)$$

where $\Delta = 1/(\text{frame rate})$ is the time step size (the variance is scaled by Δ to ensure that the noise statistics are independent of the frame rate), n_t is the number of spikes that occurred in the t -th frame, and σ_c scales the noise. Note that because we have assumed here a linear observation model (i.e., Eq. 2.1 states that F_t is a linear function of $[\text{Ca}^{2+}]_t$), our model is overparameterized. More precisely, both A and α set the scale, and $[\text{Ca}^{2+}]_b$ and β set the offset. Furthermore, because the noise is not signal dependent, both σ_F^2 and α set the effective signal-to-noise ratio (SNR). Therefore, in the following, we let $\alpha = 1$, $\beta = 0$, and $\sigma_F^2 = 1$, without loss of generality (later, we deal with this overparameterization by introducing a nonlinear observation model).

To model the spike train, we let n_t be a Bernoulli (binary) random variable, which spikes in each time step with probability $p\Delta$:

$$n_t \sim \mathcal{B}(n_t; p\Delta), \quad (2.3)$$

where $\mathcal{B}(n_t; p\Delta)$ indicates that $n_t = 1$ with probability $p\Delta$, and $n_t = 0$ with probability $1 - p\Delta$ (where $0 < p\Delta < 1$). Eq. 2.3 therefore implies that spiking at time t is independent of other spikes and the intracellular calcium concentration. Fig. 2.1 depicts a spike train (top panel), the resulting calcium transients (second panel), and the fluorescence observations

(third panel), simulated according to this model.

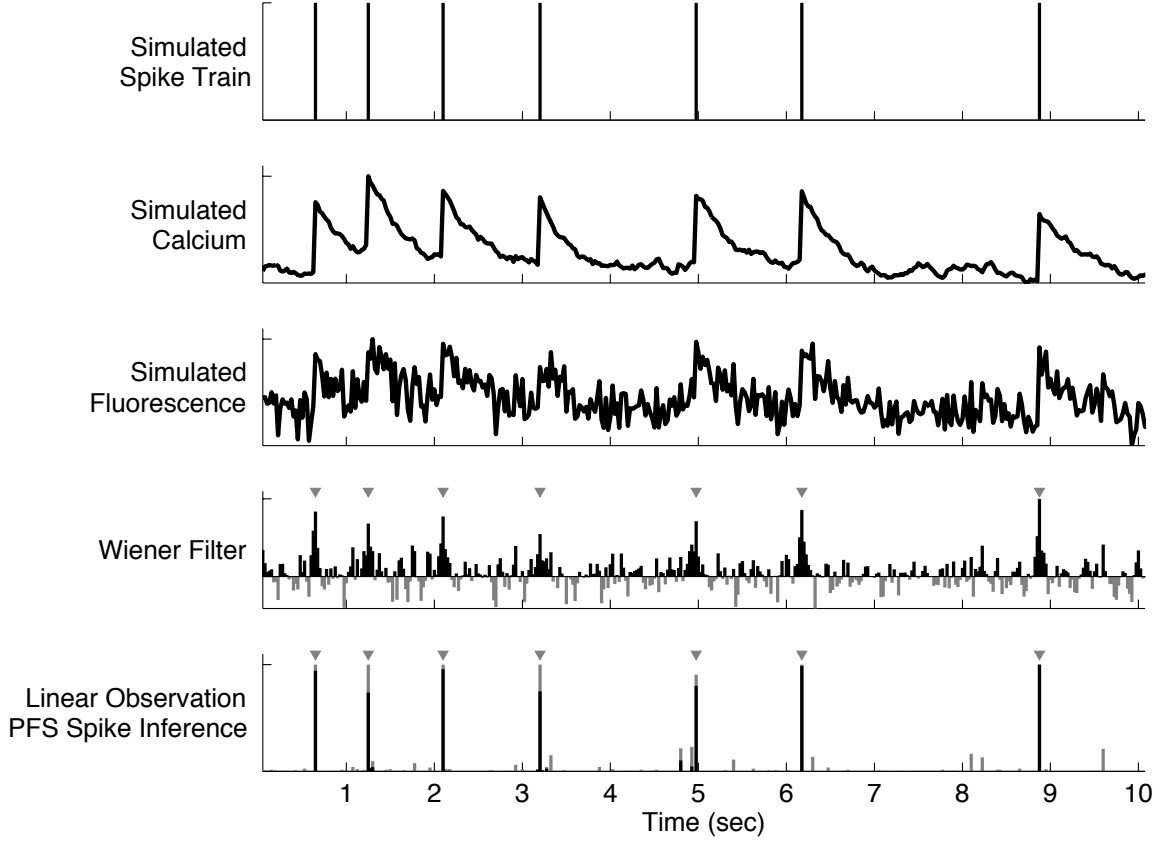


Figure 2.1: Inferring a spike train from calcium based fluorescence observations, simulated according to Eqs. 2.1 – 2.3. The optimal linear (Wiener) filter significantly smooths the observations, but fails to yield precise spike times. Our linear observation particle filter smoother (PFS), however, provides both a better estimate of the spike train, and errorbars indicating our confidence level. Top panel: Simulated spike train (# of spikes). Second panel: Simulated intracellular calcium concentration (μM). Third panel: Simulated (observed) fluorescence (a.u.). Fourth panel: Wiener filter (positive “spikes” in black, negative “spikes” in gray) (# of spikes). Bottom panel: Posterior mean (*black*) and variance (*gray*) of inferred spike train using the linear observation PFS (note the absence of negative spikes) (probability). Note that “posterior mean” indicates the posterior probability of a spike having occurred in the time bin, given the entire fluorescence trace, or, more colloquially, the algorithm’s “confidence” that a spike occurred in that bin. Gray triangles in bottom two panels indicate “true” simulated spike times. Conventions, units, and parameters are consistent throughout the figures unless otherwise indicated. Parameters: $\Delta = 25$ ms, $N = 100$ particles, $p = 0.7$, $\tau = 0.5$ s, $A = 5$ μM , $[\text{Ca}^{2+}]_b = 0.1$ μM , $\sigma_c = 1$ μM .

2.3 Mathematical Methods

Given the above model, our goal is to take the entire sequence of fluorescence observations, $F_{1:T} = [F_1, \dots, F_T]$ (where T indexes the final observation in the sequence), and infer the underlying spike train, $n_{1:T}$. More formally, we want to find $P_{\theta}(n_t|F_{1:T})$, the probability of the neuron spiking in each frame (which depends on the parameters, $\theta = \{\tau, [\text{Ca}^{2+}]_b, A, \sigma_c, p\}$), given all the fluorescence observations. We use a framework referred to as sequential Monte Carlo (using a PFS) to find these probabilities [84], embedded within an expectation maximization algorithm [85] to estimate the parameters. As this approach is becoming relatively common within neuroscience [86–92] — and it may be thought of as a generalization of either (i) the Baum-Welch algorithm for Hidden Markov Models [93], or (ii) the Kalman filter smoother for state-space models [94] — we relegate the details to the Appendices, and simply state the general procedure here.

We must first define a number of terms. Our model consists of a number of time-varying states, each governed by a set of parameters (which are constant). The states may be subdivided into *observation states*, denoted by \mathbf{O}_t , and *hidden states*, denoted by \mathbf{H}_t . Together, the states comprise the complete likelihood, which may be simplified, given our model assumptions, as follows [93]:

$$P_{\theta}(\mathbf{O}_{1:T}, \mathbf{H}_{1:T}) = P_{\theta}(\mathbf{H}_0) \prod_{t=1}^T P_{\theta}(\mathbf{H}_t|\mathbf{H}_{t-1})P_{\theta}(\mathbf{O}_t|\mathbf{H}_t), \quad (2.4)$$

where $P_{\theta}(\mathbf{H}_0)$ is the initial distribution distribution of hidden states, $P_{\theta}(\mathbf{O}_t|\mathbf{H}_t)$ is the *observation distribution* and $P_{\theta}(\mathbf{H}_t|\mathbf{H}_{t-1})$ is the *transition distribution*. For this model,

CHAPTER 2. SMC-OOPSI

the observation state is the fluorescence measurement, $\mathbf{O}_t = F_t$; and the hidden states are whether or not the neuron spiked, and the magnitude of the intracellular calcium concentration, $\mathbf{H}_t = \{n_t, [\text{Ca}^{2+}]_t\}$. We typically take the initial distribution to be baseline values, i.e., the initial calcium is $[\text{Ca}^{2+}]_b$ and initial value for the spike train is 0. The observation distribution is defined for the above model as:

$$\begin{aligned} P_{\boldsymbol{\theta}}^L(\mathbf{O}_t | \mathbf{H}_t) &\stackrel{\text{def}}{=} P_{\boldsymbol{\theta}}(F_t | [\text{Ca}^{2+}]_t, n_t) = P_{\boldsymbol{\theta}}(F_t | [\text{Ca}^{2+}]_t) \\ &= \mathcal{N}(F_t; \alpha[\text{Ca}^{2+}]_t + \beta, \sigma_F^2) = \mathcal{N}(F_t; [\text{Ca}^{2+}]_t, 1), \end{aligned} \quad (2.5)$$

which follows from Eq. 2.1 and the discussion following (where $\stackrel{\text{def}}{=}$ indicates that $P_{\boldsymbol{\theta}}^L(\mathbf{O}_t | \mathbf{H}_t)$ is defined for this *linear* model). Similarly, the transition distribution for the above model is defined as:

$$\begin{aligned} P_{\boldsymbol{\theta}}^L(\mathbf{H}_t | \mathbf{H}_{t-1}) &\stackrel{\text{def}}{=} P_{\boldsymbol{\theta}}([\text{Ca}^{2+}]_t, n_t | [\text{Ca}^{2+}]_{t-1}, n_{t-1}) = P_{\boldsymbol{\theta}}([\text{Ca}^{2+}]_t | [\text{Ca}^{2+}]_{t-1}, n_t) P_{\boldsymbol{\theta}}(n_t) \\ &= \begin{cases} \mathcal{N}([\text{Ca}^{2+}]_t; \hat{\mu}(n_t), \sigma_c^2 \Delta) (p\Delta) & \text{if } n_t = 1 \\ \mathcal{N}([\text{Ca}^{2+}]_t; \hat{\mu}(n_t), \sigma_c^2 \Delta) (1 - p\Delta) & \text{otherwise,} \end{cases} \end{aligned} \quad (2.6)$$

where $\hat{\mu}(n_t) = [\text{Ca}^{2+}]_t - \Delta/\tau([\text{Ca}^{2+}]_{t-1} - [\text{Ca}^{2+}]_b) + An_t$, and the above equation follows from Eqs. 2.2 and 2.3.

Now the goal is to efficiently estimate $P_{\boldsymbol{\theta}}(\mathbf{H}_t | \mathbf{O}_{1:T}) = P_{\boldsymbol{\theta}}(n_t, [\text{Ca}^{2+}]_t | F_{1:T})$ for all t , the posterior distribution of the hidden signals, given all the observations. Estimating this distribution is problematic, because spike trains are inherently nonlinear. Therefore, linear filters (such as the Wiener filter), are inadequate, so nonlinear filters (such as particle filters), must be employed. We proceed by taking a particle filter-smoother (PFS) approach,

CHAPTER 2. SMC-OOPSI

which breaks this problem down into two recursions. In the forward recursion, we recursively estimate $P_{\theta}(n_t, [\text{Ca}^{2+}]_t \mid F_{1:t})$, the probability of spiking and $[\text{Ca}^{2+}]$ at time t , given the fluorescence observations from time 1 up to and including t . Upon reaching time T , we recurse backward until $t = 1$, to get $P_{\theta}(n_t, [\text{Ca}^{2+}]_t \mid F_{1:T})$, the probability of spiking and $[\text{Ca}^{2+}]$ at time t given *all* the fluorescence observations (i.e., both before and after t).

We use a particle filter to approximate the forward recursion. The key is that $P_{\theta}(\mathbf{H}_t \mid \mathbf{O}_{1:t})$ may be well approximated by generating a number of weighted samples (or “particles”) [84]:

$$P_{\theta}(\mathbf{H}_t \mid \mathbf{O}_{1:t}) \approx \sum_{i=1}^N w_t^{(i)} \delta(\mathbf{H}_t - \mathbf{H}_t^{(i)}), \quad (2.7)$$

where $w_t^{(i)}$ is the relative likelihood of the state at time t taking value $\mathbf{H}_t^{(i)}$, and $\delta(\cdot)$ is the Dirac delta function (i.e., $\delta(x) = 1$ when $x = 0$ and $\delta(x) = 0$ otherwise). Thus, at each time step, one samples N particles, and then computes the weight of each. It can be shown that the weights may be recursively computed by using [84],:

$$w_t^{(i)} \approx \frac{P_{\theta}(\mathbf{O}_t \mid \mathbf{H}_t^{(i)}) P_{\theta}(\mathbf{H}_t^{(i)} \mid \mathbf{H}_{t-1}^{(i)}) w_{t-1}^{(i)}}{q(\mathbf{H}_t)}, \quad (2.8)$$

where $q(\mathbf{H}_t)$, the *sampling distribution* (or sampler) is chosen to make the approximation in Eq. 2.7 as accurate as possible. In general, the sampler may depend on all the particle history and any observations (both past and future). The most common choice is the “prior sampler,” $q(\mathbf{H}_t) = P_{\theta}(\mathbf{H}_t^{(i)} \mid \mathbf{H}_{t-1}^{(i)})$, in which we sample directly from the transition distribution. The prior sampler is very simple to use, because we know how to sample from each of the distributions comprising the transition distribution for this model (given

CHAPTER 2. SMC-OOPSI

by Eq. 2.6). The next most common choice is the “one-observation-ahead sampler” [84],

$q(\mathbf{H}_t) = P_{\theta}(\mathbf{H}_t^{(i)} | \mathbf{H}_{t-1}^{(i)}, \mathbf{O}_t)$, which may be written explicitly in terms of our model:

$$\begin{aligned} q(\mathbf{H}_t) &= P_{\theta}(\mathbf{H}_t^{(i)} | \mathbf{H}_{t-1}^{(i)}, \mathbf{O}_t) = P_{\theta}(n_t^{(i)}, [\text{Ca}^{2+}]_t^{(i)} | n_{t-1}^{(i)}, [\text{Ca}^{2+}]_{t-1}^{(i)}, F_t) \\ &= P_{\theta}(F_t | [\text{Ca}^{2+}]_t^{(i)}) P_{\theta}([\text{Ca}^{2+}]_t^{(i)} | [\text{Ca}^{2+}]_{t-1}^{(i)}, n_t^{(i)}) P_{\theta}(n_t^{(i)}) / Z, \end{aligned} \quad (2.9)$$

where the equalities follow from our model assumptions, and Z acts as a normalizing constant that does not depend on $\{n_t, [\text{Ca}^{2+}]_t\}$. The one-observation-ahead sampler conditions directly on the next fluorescence observation, and therefore “anticipates” where to best place the next hidden samples (see Appendix A for details). In practice, the one-observation-ahead sampler is more efficient than the prior sampler, meaning that we can use fewer particles to obtain the same accuracy for the approximation in Eq. 2.7 [84]. Thus, all the particle filters developed here implement the one-observation-ahead sampler (or a close approximation to it).

When implementing either sampler, after iterating several time steps, the weights of some of the particles approach zero, making the representation in Eq. 2.7 degenerate, and therefore hurting the quality of the particle approximation. To remedy this situation, whenever the approximate effective number of particles drops below some threshold (typically taken to be $N/2$), the particles may be “resampled,” by sampling (with replacement) from the population of particles. The probability of resampling each particle is related to its weight [95] (see Appendix A for details of how to weight and resample from this distribution).

CHAPTER 2. SMC-OOPSI

One recursively repeats these three steps (sampling, computing weights, and resampling if necessary) for each time step, starting at $t = 1$, and continuing through $t = T$, thus completing the forward recursion (i.e., the particle filter), and yielding an approximation to $P_{\theta}(\mathbf{H}_t | \mathbf{O}_{1:t})$ for each time step. Upon reaching $t = T$, one initializes $P_{\theta}(\mathbf{H}_T^{(i)} | \mathbf{O}_{1:T}) = w_T^{(i)}$, and then uses the following backward recursion, going from $t = T$ to $t = 1$, to approximate $P_{\theta}(\mathbf{H}_t | \mathbf{O}_{1:T})$ for each time step:

$$P_{\theta}(\mathbf{H}_t^{(i)}, \mathbf{H}_{t-1}^{(j)} | \mathbf{O}_{1:T}) = P_{\theta}(\mathbf{H}_t^{(i)} | \mathbf{O}_{1:T}) \frac{P_{\theta}(\mathbf{H}_t^{(i)} | \mathbf{H}_{t-1}^{(j)}) w_{t-1}^{(j)}}{\sum_j P_{\theta}(\mathbf{H}_t^{(i)} | \mathbf{H}_{t-1}^{(j)}) w_{t-1}^{(j)}} \quad (2.10a)$$

$$P_{\theta}(\mathbf{H}_{t-1}^{(j)} | \mathbf{O}_{1:T}) = \sum_{i=1}^N P_{\theta}(\mathbf{H}_t^{(i)}, \mathbf{H}_{t-1}^{(j)} | \mathbf{O}_{1:T}). \quad (2.10b)$$

This backward recursion is often referred to as a “particle smoother,” and comprises the backward component of our PFS approach. Thus, our PFS provides the distributions in Eq. 2.10 (for a particular model). For instance, the *linear observation* particle filter provides the distributions in Eq. 2.10, when modeling the spiking, calcium, and fluorescence dynamics according to Eqs. 2.1 – 2.3 (cf. Fig. 2.1, bottom panel). Given the distributions in Eq. 2.10, we can perform various inferences. For example, the expected number of spikes at each time step, given all the observations, may be computed by:

$$E[n_t | F_{1:T}] = \sum_{i=1}^N n_t^{(i)} P_{\theta}(n_t^{(i)} | F_{1:T}) = \sum_{i=1}^N n_t^{(i)} P_{\theta}(\mathbf{H}_t^{(i)} | \mathbf{O}_{1:T}). \quad (2.11)$$

Other quantities of interest (such as the posterior variance, median, etc.) may be computed in a similar fashion, since we have computed the full posterior distribution, $P_{\theta}(n_t | F_{1:T})$ (which, hereafter, is referred to as the posterior mean of the spike train, or simply inferred spike train). All these computations require reasonable estimates of the parameters. By

using an expectation maximization approach [85], we can iterate inferring the distributions of interest (e.g., $P_{\theta}(n_t|F_{1:T})$), and learning the parameters. More precisely, we optimize the following expected loglikelihood [96]:

$$\begin{aligned} \hat{\theta} = \operatorname{argmax}_{\theta} \sum_{t=1}^T \sum_{i,j=1}^N & \left(P_{\theta'}(\mathbf{H}_t^{(i)}, \mathbf{H}_{t-1}^{(j)} | \mathbf{O}_{1:T}) \times \ln P_{\theta}(\mathbf{H}_t^{(i)} | \mathbf{H}_{t-1}^{(j)}) \right. \\ & \left. + \sum_{i=1}^N P_{\theta'}(\mathbf{H}_t^{(i)} | \mathbf{O}_{1:T}) \times \ln P_{\theta}(\mathbf{O}_t | \mathbf{H}_t^{(i)}) \right), \quad (2.12) \end{aligned}$$

where θ' is the estimate of the parameters from the previous iteration, i.e. those used to obtain the distributions in Eq. 2.10, which may be thought of as weights on the transition and observation log-densities. Importantly, the above loglikelihood for this model was constructed to ensure that all the parameters may be quickly estimated using standard gradient ascent techniques. Details may be found in Appendix B.

2.4 Experimental Methods

2.4.1 Slice Preparation and Imaging

All animal handling and experimentation was done according to the National Institutes of Health and local Institutional Animal Care and Use Committee guidelines. Somatosensory thalamocortical slices 400 μm thick were prepared from C57BL/6 mice at age P14 as described [35]. Neurons were filled with 50 μM Fura 2 pentapotassium salt (Invitro-

CHAPTER 2. SMC-OOPSI

gen, Carlsbad, CA) through the recording pipette. Pipette solution contained 130 mM K-methylsulfate, 2 mM MgCl_2 , 0.6 mM EGTA, 10 mM HEPES, 4 mM ATP-Mg, and 0.3 mM GTP-Tris, pH 7.2 (295 mOsm). After cells were fully loaded with dye, imaging was done by using a modified BX50-WI upright confocal microscope (Olympus, Melville, NY). Image acquisition was performed with the C9100-12 CCD camera from Hamamatsu Photonics (Shizuoka, Japan) with arclamp illumination at 385 nm and 510/60 nm collection filters (Chroma, Rockingham, VT). Images were saved and analyzed using custom software written in Matlab (Mathworks, Natick, MA).

2.4.2 Electrophysiology

All recordings were made using the Multiclamp 700B amplifier (Molecular Devices, Sunnyvale, CA), digitized with National Instruments 6259 multichannel cards and recorded using custom software written using the LabView platform (National Instruments, Austin, TX). Waveforms were generated using Matlab and were given as current commands to the amplifier using the LabView and National Instruments system. The shape of the waveforms mimicked excitatory (inhibitory) synaptic inputs, with a maximal amplitude of +70 pA (−70 pA).

2.5 Results

2.5.1 Main Result

The main result of this work is depicted in Fig. 2.1, which shows a spike train, calcium concentration, and resulting fluorescence observations (first through third panels, respectively) when simulated according to the simple *linear observation* model, Eqs. 2.1 – 2.3 (where linear observation refers to the relationship between $[\text{Ca}^{2+}]_t$ and F_t). For this model, we developed a linear observation particle filter smoother (PFS), to perform optimal inference of the spike train (see Appendix A.1 for details). While the optimal linear deconvolution (i.e., the Wiener filter; see [16] for a detailed discussion on using the Wiener filter to infer spikes from calcium imaging) performs reasonably well (fourth panel), even in this relatively simple example, the linear observation PFS (bottom panel) provides several advantages. First, the spike train inferred by the linear observation PFS (dark blue, bottom panel) is a better estimate of the actual spike train than the estimate using the Wiener filter (red and blue, fourth panel). This follows because the Wiener filter assumes that the spike train has a Gaussian distribution, and therefore admits both partial and negative spikes, neither of which are possible in our model. Second, the PFS provides not only the probability of a spike occurring in each time bin, but also the entire distribution (from which we may compute errorbars; light blue in bottom panel). An even more fundamental advantage of the PFS framework is its generalizability. Below, we address a number of important generalizations to the model, each of which requires just a minor modification of the dynamics

equations, sampling distribution, and particle filter (but the smoother remains the same).

We then apply each generalization to *in vitro* data to demonstrate its utility.

2.5.2 Saturation

The relationship between the fluorescence signal and $[\text{Ca}^{2+}]_t$ is often characterized by a nonlinear saturating function, $S([\text{Ca}^{2+}]_t)$:

$$F_t = \alpha S([\text{Ca}^{2+}]_t) + \beta + \eta_t. \quad (2.13)$$

The above equation states that at any time, the *expected value* of fluorescence is a nonlinear saturating function of the calcium signal. The gain (or slope), α , accounts for all the factors contributing to signal amplification, including the number of fluorophores in the neuron, the brightness of each fluorophore, the gain of the image acquisition system, etc. The offset, β , accounts for any factor leading to a constant background signal, such as baseline fluorescence. The nonlinear saturation function, $S([\text{Ca}^{2+}]_t)$, is often taken to be the Hill equation, i.e. $S(x) = x^n / (x^n + k_d)$, where n is the Hill coefficient, and k_d is the dissociation constant [77]. The variance, η_t , may be generalized similarly. Assuming the primary noise source is photon shot noise, it would be appropriate to model noise as a Poisson process, which could be well approximated by a Gaussian distribution for large photon counts [36]:

$$\eta_t = \sqrt{\xi S([\text{Ca}^{2+}]_t) + \sigma_F \varepsilon_{F,t}}, \quad (2.14)$$

where σ_F scales the signal-to-noise ratio (SNR). Note that there is no scale term for the saturated fluorescence component of the noise, as it would not be identifiable (α , β , and

CHAPTER 2. SMC-OOPSI

σ_F could be normalized by it without loss of generality). These assumptions change the observation distribution from Eq. 2.5 to:

$$P_{\theta}^{NL}(\mathbf{O}_t | \mathbf{H}_t) \stackrel{def}{=} \mathcal{N}(F_t; \alpha S([\text{Ca}^{2+}]_t) + \beta, \xi S([\text{Ca}^{2+}]_t) + \sigma_F). \quad (2.15)$$

To perform optimal inference on this model (i.e., Eqs. 2.2, 2.3, 2.13, and 2.14), we construct a *nonlinear observation* PFS (where nonlinear observation refers to the relationship between F_t and $[\text{Ca}^{2+}]_t$ given by Eq. 2.15). The nonlinear observation PFS is different from the linear observation PFS because the observation distributions for which the two filters were designed differ, thus the one-observation-ahead sampler ($q(\mathbf{H}_t) = P_{\theta}(\mathbf{H}_t^{(i)} | \mathbf{H}_{t-1}^{(i)}, \mathbf{O}_t)$) changes (See Appendix A.2 for details).

Fig. 2.2 shows an example of data simulated using the above model (Eqs. 2.2, 2.3, 2.13, and 2.14; top three panels). Two important differences between this model and the linear model are apparent. First, the nonlinear saturating function, $S([\text{Ca}^{2+}]_t)$, causes the fluorescence to decay more slowly than the calcium. Thus, if one were to simply deconvolve the spike trains from the raw fluorescence observations, the estimate of the spike train ($n_{1:T}$) and time constant (τ) would be biased. Second, as $[\text{Ca}^{2+}]$ accumulates, the fluorescence transients due to a spike become smaller. This reduces the effective SNR, obfuscating estimating the jump size, A . The Wiener filter (fourth panel), which cannot incorporate a nonlinearity, performs less well in this scenario than in the linear scenario. This may be evident from the observation that peaks in the Wiener filter output become smaller and closer to the noise when the signal approaches saturation. The nonlinear observation PFS, however, explicitly models this nonlinearity, and therefore can infer spikes very accurately

CHAPTER 2. SMC-OOPSI

even in the saturating regime (fifth panel). Furthermore, using the nonlinear observation PFS, we can reconstruct the unsaturated $[\text{Ca}^{2+}]_t$ (bottom panel) in addition to the spike train (when assuming Eq. 2.15 accurately describes the relationship between calcium and fluorescence). This is an absolute estimate of $[\text{Ca}^{2+}]_t$, meaning that we infer the baseline calcium concentration and jump size in real units (as opposed to only relative units), which follows because relative changes in fluorescence correspond with absolute changes in the *unsaturated* calcium concentration, due to the assumed nonlinear relationship between F_t and $[\text{Ca}^{2+}]_t$.

Fig. 2.3 shows an example of saturating fluorescence observations recorded *in vitro* (top panel). Within a burst, later spikes cause fluorescent transients that are smaller than the first few spikes. This is evident from the Wiener filter, in which the inferred spike size becomes much smaller in large bursts (second panel). The nonlinear observation PFS, however, accurately infers exactly one spike for each frame in which a spike occurred (third panel). Furthermore, we infer the underlying and non-saturating calcium transients (bottom panel), which is not possible using linear methods. Fig. 2.4 shows another example of a spike train recorded *in vitro*, but with far noisier observations and a more “naturalistic” spike train. As in Fig. 2.3, even though the effective SNR of the Wiener filter output deteriorates as the fluorescence signal saturates, the nonlinear observation PFS can accurately infer precise spike times.

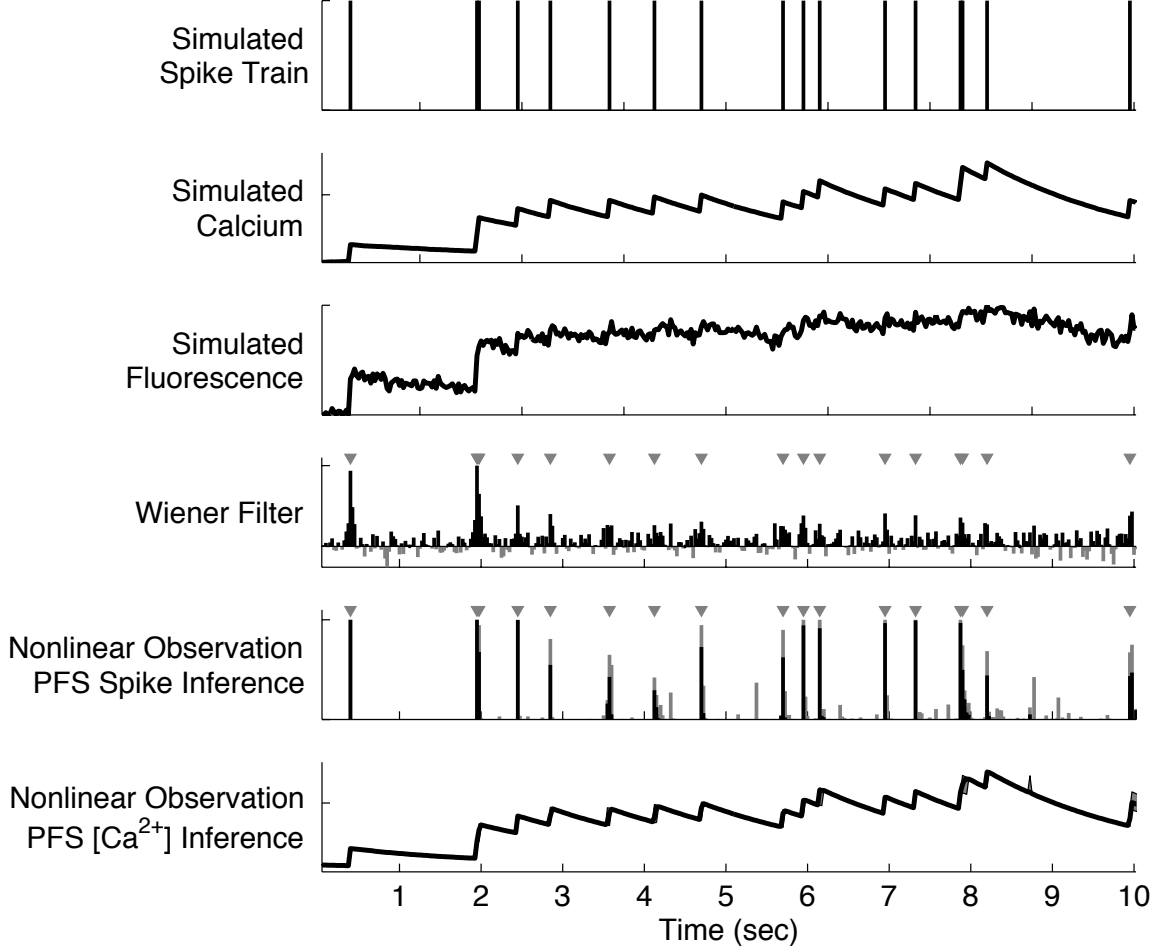


Figure 2.2: Inferring a simulated spike train upon incorporating a more realistic saturating observation and noise model (Eqs. 2.13 and 2.14, respectively). As the fluorescence signal approaches saturation, the effective SNR of the Wiener filter’s output degrades substantially. Our nonlinear observation PFS, however, accurately infers the precise spike times even when the signal is strongly saturating, and provides an estimate for the unsaturated calcium concentration (which is obtainable due to the assumed nonlinear relationship between calcium and fluorescence). Top four panels as in Fig. 2.1. Fifth panel: Posterior mean (*black*) and variance (*gray*) of inferred spike train using the nonlinear observation PFS (probability). Bottom panel: Posterior mean (*black*) and variance (*gray*) of calcium inference using the nonlinear observation PFS (μM). Tick mark at $200 \mu\text{M}$. Parameters different from Fig. 2.1: $p = 0.99$, $A = 50 \mu\text{M}$, $\tau = 2 \text{ s}$, $\xi = 4 \times 10^{-4} \text{ a.u.}$, $\sigma_F = 10^{-4} \text{ a.u.}$, $n = 1$, $k_d = 200 \mu\text{M}$.

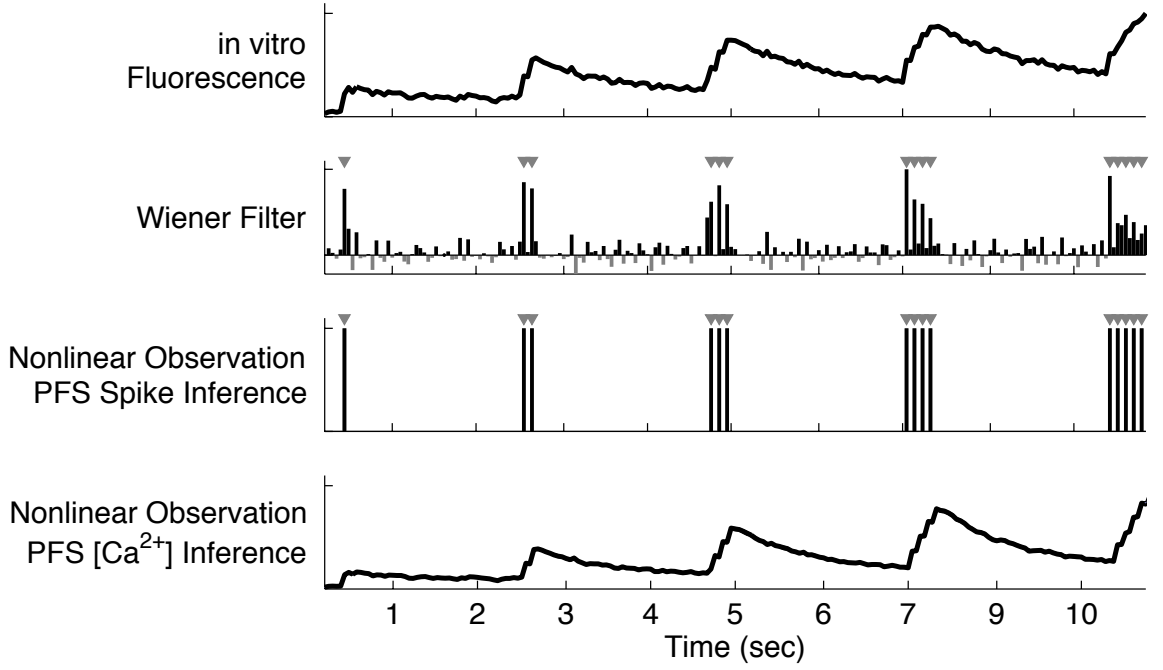


Figure 2.3: Using only strongly saturating *in vitro* fluorescence measurements to infer precise spike times within short bursts recorded *in vitro*. As the number of spikes in a burst increases, the fluorescence signal begins to saturate, drastically reducing the effective SNR of the Wiener filter output. The nonlinear observation PFS, however, correctly infers the precise timing of each spike, regardless of the number of spikes within a burst. Note that the parameters were initialized poorly (not shown), and the algorithm quickly converged to a set of parameters that accurately inferred the precise spike times, and provided an estimate of the non-saturating calcium transients, using only the data shown. Top panel: *in vitro* saturating fluorescence measurements. Second panel: Wiener filter. Third panel: nonlinear observation PFS spike train inference. Bottom panel: nonlinear observation PFS $[Ca^{2+}]$ inference. $\Delta \approx 50$ msec.

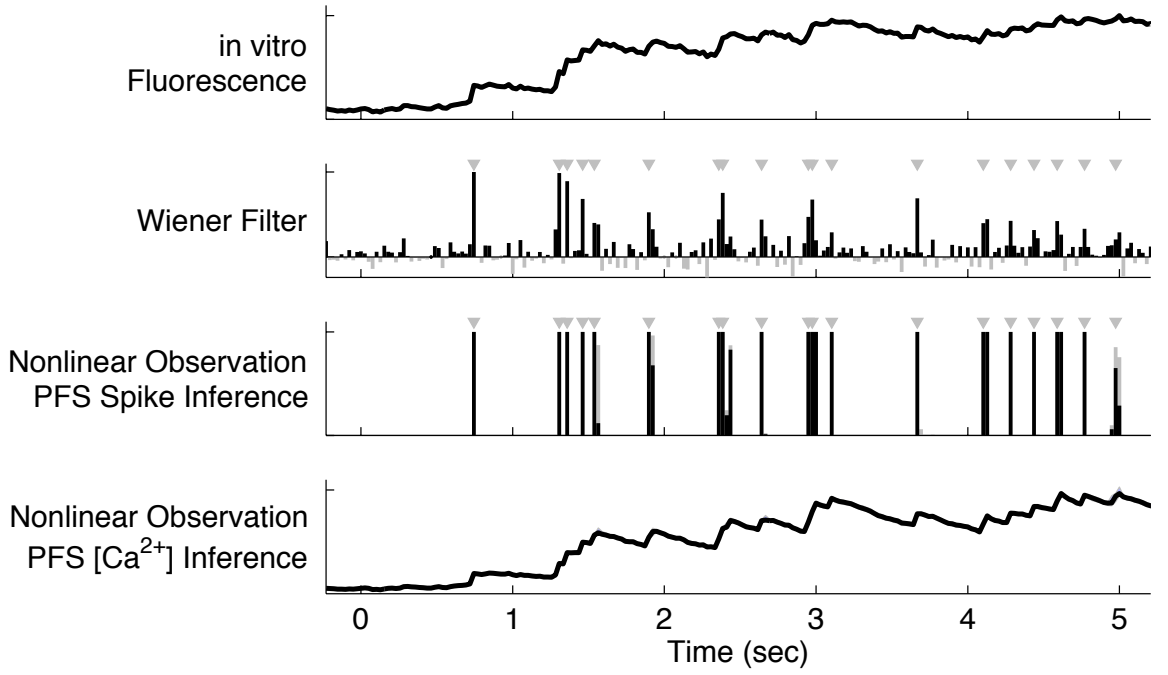


Figure 2.4: In vitro noisy saturation: Using only strongly saturating and very noisy *in vitro* fluorescence measurements to infer precise spike times in a “naturalistic” spike train recorded *in vitro*. As in Fig. 2.3, as the fluorescence signal approaches complete saturation, the effective SNR of the Wiener filter is substantially reduced, whereas our nonlinear observation PFS fares relatively well. Conventions as in Fig. 2.3. $\Delta \approx 25$ msec.

2.5.3 Superresolution

Technological limitations often impose an undesirable upper bound on the imaging frame rate. In this context, superresolution denotes the ability to infer spike trains with more precision than the frame rate. Our assumptions may be generalized for superresolution inference by modifying the observation model. First, we reduce the time step size by a factor, d , such that $\Delta = 1/(d \times \text{frame rate})$. Now we have two cases for the observation distribution: the case described by Eq. 2.15 (which now occurs every d time steps), and the “null” case, where no observation occurs (and therefore, $P_{\theta}(\mathbf{O}_t | \mathbf{H}_t) = 1$). To perform optimal inference given this more sophisticated observation distribution, we develop a *superresolution* PFS (see Appendix A.3 for details). Fig. 2.5 shows how the superresolution PFS inference precision scales with both imaging frame rate and observation noise. Importantly, the probability of spiking in each time step within an image is not uniform, but rather, tends to be higher around the actual spike time. As the noise is increased, the probabilities further spread and flatten, but still yield an accurate estimate of the total number of spikes per frame (assuming one tends to collect a large enough number of photons per pixel to be detected by the imaging system).

One interesting result of this analysis is that imaging faster, while increasing noise and *decreasing* SNR per frame [36], can actually increase fidelity (i.e., effective SNR). This may be seen by comparing panels arranged diagonally ascending to the right, which show how the inference performs upon increasing frame rate and noise proportionally. Although the SNR per frame decreases, because more information is available about the

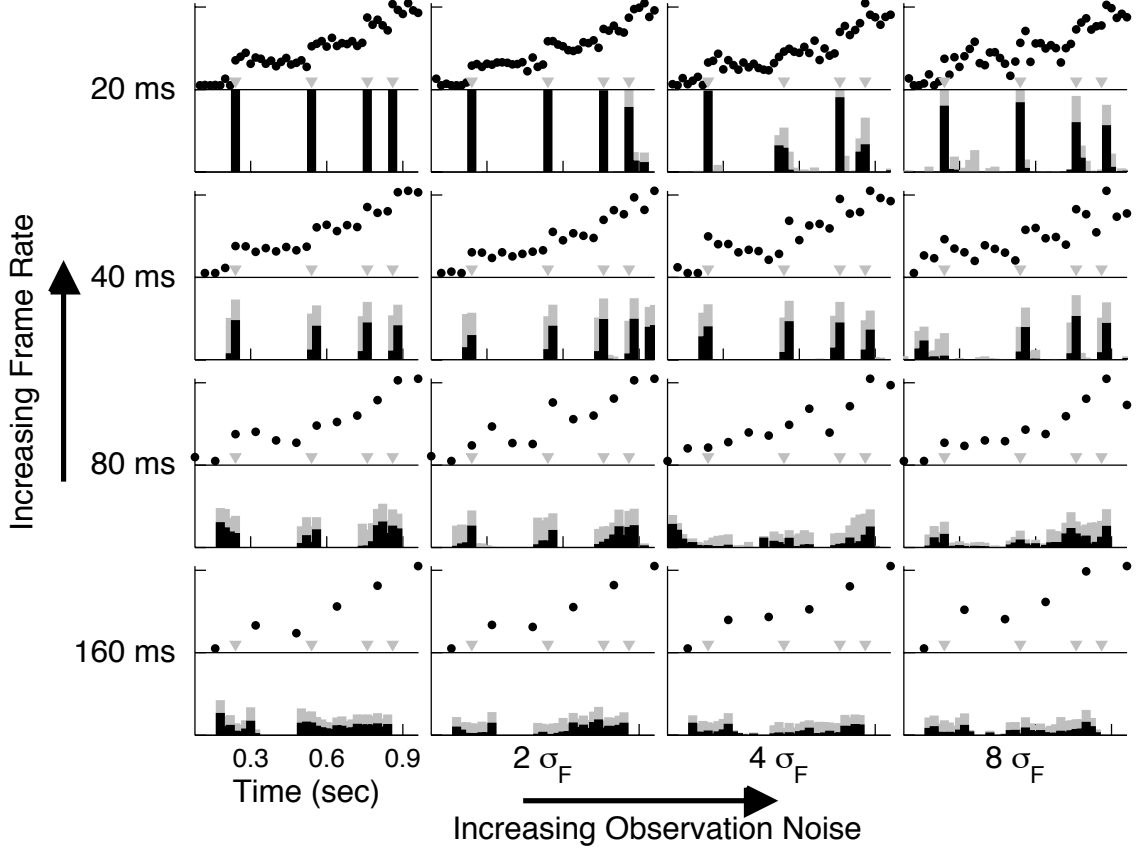


Figure 2.5: Array of inference capabilities when using the superresolution PFS. Although for these simulations, $\Delta = 20$ ms, observations are made only “intermittently” (i.e. once every d time steps), corresponding to a 2-photon scanning experiment, for instance. Depending on the effective SNR, the spike train inference can be better than the image frame rate would naïvely permit, achieving superresolution. Each panel shows fluorescence observations (*black dots*; a.u.), spike trains simulated using Eqs. 2.2, 2.3, 2.13, and 2.14 (*gray triangles*), and posterior mean and variance of spiking at each time (*black and gray*, respectively). Subsequent columns (rows) increase noise (frame rate) by a factor of two. Panels arranged diagonally upwards and rightwards therefore indicate how inference might improve by simply scanning faster (even though SNR per image frame degrades). Parameters different from Fig. 2.2: $p = 4$. $A = 20 \mu\text{M}$. $[\text{Ca}^{2+}]_b = 20 \mu\text{M}$.

decay, superior inference precision may be achieved. This suggests that given the option, it is always advantageous to image as quickly as possible, even at the expense of reduced SNR per frame.

2.5.4 Spike History and Stimulus Dependence

So far, we have assumed that our neuron generates spikes independent of both external stimuli and its own spike history (cf. Eq. 2.3). These two inputs (stimuli and spike histories) may be cf. into this framework by replacing p of Eq. 2.3 with a Generalized Linear Model (GLM) [97]. GLMs have recently been used extensively to model spike trains from a variety of different preparations and modalities (see, for example, [98]). While many GLMs could be applied here, to fit within the sequential Monte Carlo expectation maximization framework, we require that: (i) the loglikelihood is concave in the parameters of the GLM, and (ii) the dynamics are Markovian. To satisfy our first constraint (concavity), we propose to allow the probability of spiking, p_t , to be a time-varying nonlinear function of the input to the neuron, y_t :

$$p_t = 1 - e^{-f(y_t)\Delta}, \quad (2.16)$$

where $f(\cdot)$ is some convex and log-concave function (see [99] for more details on Eq. 2.16). In general, the input to the neuron, y_t , may be subdivided into a multidimensional stimulus, \mathbf{x}_t , and a set of spike history terms, $\mathbf{h}_t = \{h_{1,t}, \dots, h_{L,t}\}$, yielding:

$$y_t = \mathbf{k}'\mathbf{x}_t + \mathbf{w}'\mathbf{h}_t, \quad (2.17)$$

CHAPTER 2. SMC-OOPSI

where \mathbf{k} is a linear filter operating on the stimulus (which is closely related to the spike-triggered-average of the neuron [100]), \mathbf{w} weights the spike history terms [101], and $'$ denotes the transpose operation. To satisfy the second constraint above (Markovian dynamics), we use a set of exponentially decaying terms, each with a unique time constant:

$$h_{l,t} - h_{l,t-1} = -\frac{\Delta}{\tau_{h_l}} h_{l,t-1} + n_{t-1} + \sigma_{h_l} \sqrt{\Delta} \varepsilon_{l,t}, \quad (2.18)$$

implying that after each spike, each spike history term jumps, and then decays back to zero with time constant τ_{h_l} (and each process has noise with variance $\sigma_{h_l}^2 \Delta$). Eq. 2.18 is sufficiently general to account for most spike history effects, including refractoriness, burstiness, facilitation, adaptation, and oscillations [102]. To optimally infer spikes given this more sophisticated model (i.e., Eqs. 2.2, 2.13, 2.14, and 2.16 – 2.18), we modify our superresolution PFS to incorporate the above GLM, yielding a GLM PFS (see Appendix A.4 for details).

Fig. 2.6 shows a simulation using a model that incorporates saturation and signal dependent noise, as well as stimulus and spike history dependent spiking, with an unsatisfactorily slow frame rate (top six panels). Although the superresolution PFS accurately infers in which frame spikes occur (seventh panel), its superresolution abilities are limited due to saturation and low SNR. By contrast, the GLM PFS accurately infers spike times with superresolution precision by utilizing the input and spike history dependence (bottom panel). Note that even when multiple spikes occur within a single image frame, the GLM PFS correctly infers the number of spikes, and provides a good estimate for the precise timing of each spike (see simulated data and inference between 0.5 and 1 sec).

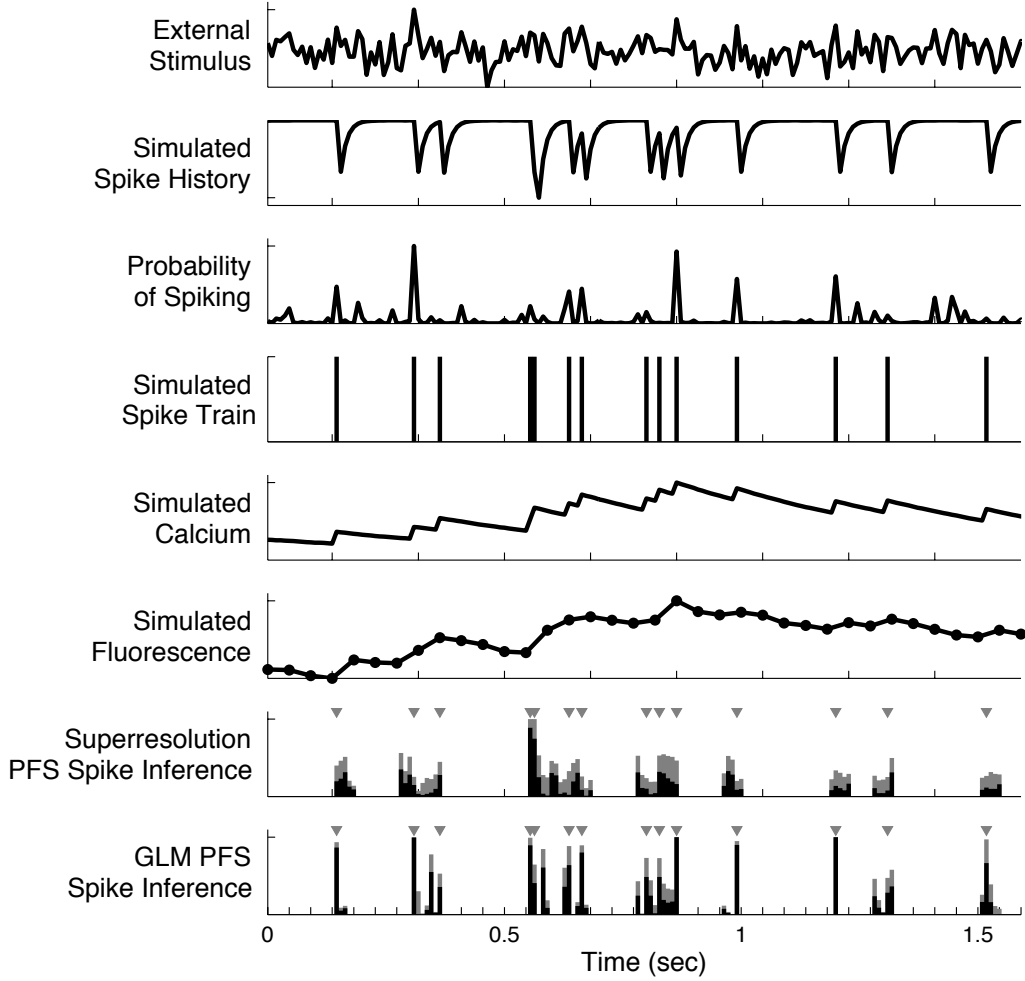


Figure 2.6: Generalized Linear Model Particle Filter Smoother (GLM PFS) permits refining spike inference precision by incorporating both stimulus and spike history dependence into the model and sampler. This highly saturating and noisy example was simulated using Eqs. 2.2, 2.13, 2.14, 2.16, 2.17, 2.18, and obtaining an observation only once per 5 time steps. While the superresolution PFS correctly identifies in which frames a spike occurs, only the GLM PFS — which not only samples spikes conditioned on the next observation, but also the spike history and stimulus — can achieve superresolution on this kind of data. Top panel: External stimulus (a.u.). Second panel: A single spike history term was simulated for this model (unitless). Third panel: Probability of spiking. Fourth panel: Simulated spike train. Fifth panel: Simulated $[Ca^{2+}]$. Sixth panel: Observations (dots indicates observation times, lines are merely linear interpolation for visualization purposes). Seventh panel: superresolution PFS spike inference. Bottom panel: GLM PFS spike inference. Parameters different from Fig. 2.5: $k = 1.7$. $\omega = -0.3$. $\tau_{h_i} = 50$ ms. $\sigma_{h_i} = 0.01$

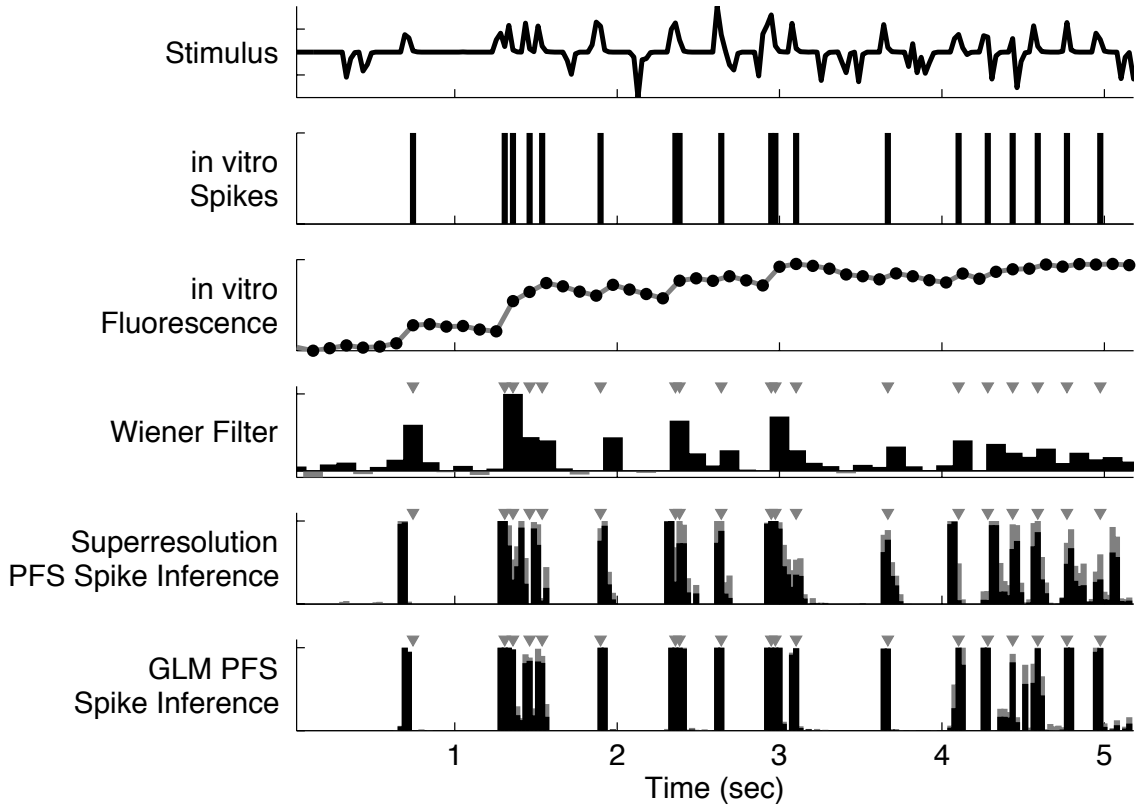


Figure 2.7: The GLM PFS can infer spikes from real data with superresolution using external stimulus and spike histories. While the Wiener filter provides bumps around frames in which a spike occurred, both the superresolution PFS and the GLM PFS correctly infer in which frame spikes occur. Only the GLM PFS, however, can resolve spike times with superresolution. Top panel: External stimulus. Second panel: Real spike train. Third panel: Real fluorescence. Fourth panel: Wiener filter. Fifth panel: Superresolution PFS spike inference. Bottom panel: GLM PFS spike inference. $\Delta \approx 100$ msec. $d = 4$.

Fig. 2.7 uses *in vitro* data to compare the Wiener filter, superresolution PFS, and GLM PFS. Here, a neuron under patch clamp (current clamp mode) was stimulated with a time-varying current (top panel). The exact spike times were recorded electrophysiologically (second panel), while simultaneously imaging the fluorescence signal (third panel). The Wiener filter (fourth panel) generates “bumps” near the frames in which spikes arrived, but generally fails to identify individual spike times.

The superresolution PFS succeeds in identifying the spikes, but with limited temporal resolution (fifth panel). By including stimulus information and spike history dependence, the GLM PFS further refines the temporal estimates beyond that of our sampling interval. From this data set, we could achieve a temporal precision of approximately 25 msec, even though observations were only obtained once per 100 msec (bottom panel).

2.5.5 Learning the parameters

All of the above results depend on our ability to estimate the parameters. The models were constructed to ensure that the loglikelihood functions were concave jointly in all the parameters, facilitating using standard gradient ascent techniques to find their maximum likelihood estimators. Table 2.1 shows the parameter estimates using only noisy fluorescence observations including very few spikes. As the number of spikes underlying the observations increases, our parameter estimates improve both in accuracy and precision. This suggests that upon learning the parameters from the *in vitro* data, our absolute calcium concentration estimates reflect the true values (which could be confirmed using ratiometric dyes or calibration experiments [77]). Importantly, these computations may be performed relatively quickly. More specifically, the number of computations scales linearly with T and quadratically with N (due to Eq. 2.10). In practice, for all the above examples (both simulated and real), a single iteration ran in approximately real time on a standard laptop computer (i.e., 5 s of data required 5 s of computation; requiring only ~ 100 particles to obtain sufficiently accurate approximations for all examples). Moreover, parameters typ-

ically converged in < 50 iterations, so inference on data collected during the day can be completed overnight.

Table 2.1: Mean (standard deviation) of calcium parameters estimated using only short fluorescence observations. The data were simulated assuming Eqs. 2.2, 2.3, 2.15, and 2.16 (i.e. no external stimulus or spike history effects). All parameters were initialized to be incorrect by a factor of two, which more than spans the typical physiological range [29]. The simulation parameters were chosen to reflect the noise statistics of the *in vitro* data from Figs. 2.3, 2.4, and 2.7. We simulated four cases, each corresponding to a different number of spikes underlying the observed fluorescence (i.e., 5, 10, 20, or 40). For each case, we ran between 5 and 10 simulations. Parameters converged either when the difference between the likelihoods in two subsequent iterations no longer exceeded a minimum threshold, or the number of iterations exceeded 50. The baseline calcium concentration, $[\text{Ca}^{2+}]_b$, is the most difficult parameter to learn because of the nonlinear saturation, which makes the likelihood along the $[\text{Ca}^{2+}]_b$ dimension relatively flat.

Parameter	True value	5 spikes	10 spikes	20 spikes	40 spikes	units
A	5	4.6 (1.4)	4.9 (0.36)	4.8 (0.82)	5.0 (0.16)	μM
τ	0.5	0.57 (0.35)	0.59 (0.12)	0.58 (0.12)	0.52 (0.036)	sec
$[\text{Ca}^{2+}]_b$	5	3.4 (3.8)	3.3 (3.2)	3.5 (1.7)	4.3 (0.92)	μM

2.6 Discussion

We started by constructing a very simple model relating spiking, calcium, and fluorescence observations, and showed that our linear observation PFS both improves inference accuracy over the optimal linear method, and provides errorbars (cf. Fig. 2.1). Then, we relaxed a number of the assumptions, to show how our method can be generalized. First, we postulated a more realistic observation model, by incorporating both saturation and signal dependent noise, and showed that a nonlinear observation PFS outperforms the Wiener

CHAPTER 2. SMC-OOPSI

filter (cf. simulated data in Fig. 2.2 and real data in Figs. 2.3 and 2.4). Then, we demonstrated superresolution capabilities, by inferring when within an image frame spikes occur, using our superresolution PFS (cf. Fig. 2.5). By incorporating a GLM to govern spiking activity in our model, we could also account for spike history and stimulus dependencies, utilizing our GLM PFS (cf. Fig. 2.6), and further enhance the inference precision using *in vitro* data (cf. Fig. 2.7). These results all depend on an ability to accurately estimate the model parameters, even when given only short ($\sim 5 - 10$ s and $5 - 50$ spikes) and noisy fluorescence observations. Importantly, estimating these parameters did not require any additional simultaneous electrophysiology or imaging experiments; rather, all inferences and parameter estimations were performed using only the fluorescence observations. Simultaneous imaging and electrophysiological experiments, however, for confirmation, would be desirable in novel preparations. Finally, as each iteration may be performed in real time, and the parameters converged in < 50 iterations, this analysis does not impose severe computational restrictions, and may be performed between experimental sessions, for instance (though see [18] for a complementary “online” algorithm). These examples demonstrate the power of the proposed particle filtering methods.

While the above generalizations were sufficient to infer the spikes in this data set, further generalizations may be necessary for other preparations. Perhaps most importantly, we ignored several prominent noise sources. For instance, the point spread function of a 2-photon microscope *in vivo* often spans several microns in the axial dimension, which is sufficiently large to capture activity in the surrounding neuropil [8]. Furthermore, tis-

CHAPTER 2. SMC-OOPSI

sue movement is often a problem, especially when imaging animals that are awake and/or behaving [103]. While both axial resolution and movement artifacts are currently being addressed experimentally, we could incorporate these additional noise sources into our model as well (by modifying our noise assumptions, Eq. 2.14).

The dynamics of each of the states could also be generalized in a number of ways. First, bleaching is often a problem, especially for *in vivo* settings. This could easily be incorporated in our framework by allowing the observation parameters, $\{\alpha, \beta, \sigma_F\}$, to decay with time constants that could be inferred directly. Second, while we implicitly assumed that fluorescence achieves steady-state instantaneously, we could instead include more realistic fluorescence dynamics, which may be necessary for slower indicators, such as the genetically encoded probes [76]. Third, the proposed model for calcium dynamics, Eq. 2.2, could be generalized in a number of ways. For instance, we could (i) enable the transient influx in $[\text{Ca}^{2+}]_t$ due to a spike be variable, or (ii) incorporate additional time constants, to facilitate a non-instantaneous rise time, adaptation, extrusion, or other more sophisticated calcium dynamics [104].

Finally, one of the major goals of large-scale calcium fluorescence imaging experiments is to understand the dynamics of neural populations [6, 43]. The proposed methodology could readily be implemented while imaging a heterogeneous population of neurons, by estimating the observation, calcium, and spiking dynamics parameters independently for each observable neuron. Alternately, an important aspect of our proposed model is the spike history terms, which here only cause effects in a single neuron. This model may

CHAPTER 2. SMC-OOPSI

easily be generalized to include not only the “self-coupling” spike history effects discussed here (cf. Fig. 2.6), but also “cross-coupling” terms, which model the effects that one neuron’s activity has upon other “target” neurons in the observed population [100,101,105]. Then, estimating these interneuronal spike history weights ω corresponds to estimating a functional connectivity matrix of the network. We will address the practical limitations of inference quality and parameter estimation accuracy for large populations of neurons in future work.

Appendix A

Details for constructing the particle filters

In this appendix, we provide details for sampling, computing the weights, and resampling. The simplest and most common sampling strategy is to let the sampling distribution be the prior (or transition) distribution, i.e., $q(\mathbf{H}_t) = P_{\theta}(\mathbf{H}_t^{(i)}|\mathbf{H}_{t-1}^{(i)})$. In general, when sampling from the prior transition distributions, the importance weights simplify:

$$\tilde{w}_t^{(i)} = \frac{P_{\theta}(\mathbf{O}_t|\mathbf{H}_t^{(i)})P_{\theta}(\mathbf{H}_t^{(i)}|\mathbf{H}_{t-1}^{(i)})w_{t-1}^{(i)}}{q(\mathbf{H}_t)} = P_{\theta}(\mathbf{O}_t|\mathbf{H}_t^{(i)})w_{t-1}^{(i)}, \quad (\text{A.1})$$

which follows from substituting $P_{\theta}(\mathbf{H}_t^{(i)}|\mathbf{H}_{t-1}^{(i)})$ for $q(\mathbf{H}_t)$, and then canceling this transition distribution from both the numerator and denominator. If the observation \mathbf{O}_t is significantly different from the value predicted by the observation distribution, $P_{\theta}(\mathbf{O}_t|\mathbf{H}_t^{(i)})$, then the prior sampler wastes most of its samples by choosing particles with values of \mathbf{H}_t that do not correspond to the observations. Thus, to construct an accurate approximation to

APPENDIX A. DETAILS FOR CONSTRUCTING THE PARTICLE FILTERS

the true underlying distribution, many particles would be required. Unfortunately, many of these particles would be relatively unlikely, and therefore, have their corresponding weights close to zero, i.e., $w_t^{(i)} \approx 0$. To mitigate this effect, one must resample frequently, to eliminate particles that are far from the observation, and replicate ones that are close. Note that it is only by virtue of resampling that the observations are incorporated into this sampler.

More efficient sampling can be achieved by using a sampling distribution that explicitly considers the observations. A common approach is to use the “one-observation-ahead” sampler [84], $q(\mathbf{H}_t) = P_{\theta}(\mathbf{H}_t^{(i)} | \mathbf{H}_{t-1}^{(i)}, O_t) \propto P_{\theta}(O_t | \mathbf{H}_t) P_{\theta}(\mathbf{H}_t | \mathbf{H}_{t-1}^{(i)})$. Because constructing the one-observation-ahead sampler is tractable for all the models considered in the main text, below we provide details for constructing such samplers.

A.1 Linear observation particle filter

For the linear observation model, we have:

$$q_{\theta}^L([\text{Ca}^{2+}]_t^{(i)}, n_t^{(i)}) \stackrel{\text{def}}{=} P_{\theta}^L(F_t | [\text{Ca}^{2+}]_t^{(i)}) \\ P_{\theta}([\text{Ca}^{2+}]_t^{(i)} | [\text{Ca}^{2+}]_{t-1}^{(i)}, n_t^{(i)}) P_{\theta}(n_t^{(i)}), \quad (\text{A.2})$$

where the L superscript indicates that this is the sampling distribution for the linear observation model, and the three distributions on the right-hand-side of Eq. A.2 are given by Eqs. 2.1 – 2.3 (note that $q_{\theta}^L(\cdot)$ is implicitly a function of both $[\text{Ca}^{2+}]_{t-1}^{(i)}$ and F_t). To sample spikes, we must compute $q_{\theta}^L(n_t^{(i)})$ by integrating out $[\text{Ca}^{2+}]_t^{(i)}$. Having sampled $n_t^{(i)}$

APPENDIX A. DETAILS FOR CONSTRUCTING THE PARTICLE FILTERS

for each particle, we may then sample from $q_{\theta}^L([\text{Ca}^{2+}]_t^{(i)})$. Below we provide details for sampling both n_t and $[\text{Ca}^{2+}]_t$, conditioned on the next observation.

A.1.1 Constructing $q_{\theta}^L(n_t^{(i)})$

We sample spikes from $q_{\theta}^L(n_t^{(i)})$, which we compute by integrating out $[\text{Ca}^{2+}]_t^{(i)}$ from Eq. A.2:

$$q_{\theta}^L(n_t^{(i)}) = \int q_{\theta}^L([\text{Ca}^{2+}]_t^{(i)}, n_t^{(i)}) d[\text{Ca}^{2+}]_t^{(i)} \quad (\text{A.3a})$$

$$\sim P_{\theta}(n_t^{(i)}) \int P_{\theta}([\text{Ca}^{2+}]_t^{(i)} | [\text{Ca}^{2+}]_{t-1}^{(i)}, n_t^{(i)}) P_{\theta}(F_t | [\text{Ca}^{2+}]_t^{(i)}) d[\text{Ca}^{2+}]_t^{(i)}, \quad (\text{A.3b})$$

which corresponds to the probability of particle i sampling a spike, given its previous value for calcium, $[\text{Ca}^{2+}]_{t-1}^{(i)}$, and the current observation, F_t . To evaluate the above integral, we first note that the observation distribution may be written as a Gaussian function of $[\text{Ca}^{2+}]_t^{(i)}$, i.e.:

$$P_{\theta}^L(F_t | [\text{Ca}^{2+}]_t^{(i)}) = \mathcal{N}(F_t; [\text{Ca}^{2+}]_t^{(i)}, 1) = \mathcal{N}([\text{Ca}^{2+}]_t^{(i)}; F_t, 1), \quad (\text{A.4})$$

which follows the fact that $\mathcal{N}(x; \mu, \sigma^2) = \mathcal{N}(\mu; x, \sigma^2)$. Now, given that both the distributions in the integral in Eq. A.3b can be written as Gaussian functions of $[\text{Ca}^{2+}]_t^{(i)}$, we use the fact that the integral of the product of two Gaussian functions of the same variable yields a Gaussian:

$$\begin{aligned} \int \frac{1}{\sqrt{2\pi}\sigma_1} \exp\left\{-\frac{1}{2}\left(\frac{x-\mu_1}{\sigma_1}\right)^2\right\} \times \frac{1}{\sqrt{2\pi}\sigma_2} \exp\left\{-\frac{1}{2}\left(\frac{x-\mu_2}{\sigma_2}\right)^2\right\} dx \\ = \frac{1}{\sqrt{2\pi}s} \exp\left\{-\frac{1}{2}\frac{(\mu_1-\mu_2)^2}{s}\right\}, \end{aligned} \quad (\text{A.5})$$

APPENDIX A. DETAILS FOR CONSTRUCTING THE PARTICLE FILTERS

where $s = \sigma_1^2 + \sigma_2^2$. We can therefore evaluate the integral in Eq. A.3b by plugging in the distributions given by Eqs. 2.1 and 2.2, and swapping terms as in Eq. A.4:

$$\int P_{\theta}([\text{Ca}^{2+}]_t^{(i)} \mid [\text{Ca}^{2+}]_{t-1}^{(i)}, n_t^{(i)}) P_{\theta}(F_t \mid [\text{Ca}^{2+}]_t^{(i)}) d[\text{Ca}^{2+}]_t^{(i)} = \mathcal{G}_{\theta}^L(n_t^{(i)} \mid F_t) \stackrel{\text{def}}{=} \frac{1}{Z} \frac{1}{\sqrt{2\pi(\sigma_F^2 + \sigma_c^2 \Delta)}} \exp \left\{ -\frac{1}{2} \frac{(F_t - C_t^{(i)})^2}{\sigma_F^2 + \sigma_c^2 \Delta} \right\}, \quad (\text{A.6})$$

where we let $C_t^{(i)} = (1 - \frac{\Delta}{\tau})[\text{Ca}^{2+}]_{t-1}^{(i)} + A n_t^{(i)} + \frac{\Delta}{\tau}[\text{Ca}^{2+}]_b$, which is implicitly a function of $n_t^{(i)}$. We compute $\mathcal{G}_{\theta}^L(n_t^{(i)} \mid F_t)$ for the two cases, $n_t^{(i)} = 0$ and $n_t^{(i)} = 1$, and then, for each particle, one samples from:

$$\tilde{q}_{\theta}^L(n_t^{(i)}) = \mathcal{B}(n_t^{(i)}; p\Delta) \mathcal{G}_{\theta}^L(n_t^{(i)} \mid F_t) \quad (\text{A.7a})$$

$$q_{\theta}^L(n_t^{(i)}) = \frac{\tilde{q}_{\theta}^L(n_t^{(i)})}{\sum_{n_t^{(i)} \in \{0,1\}} \tilde{q}_{\theta}^L(n_t^{(i)})}. \quad (\text{A.7b})$$

A.1.2 Constructing $q_{\theta}^L([\text{Ca}^{2+}]_t^{(i)})$

Having sampled spikes, we can plug them back into Eq. A.2, and integrate out $n_t^{(i)}$, to obtain the distribution from which we sample $[\text{Ca}^{2+}]_t$:

$$q_{\theta}^L([\text{Ca}^{2+}]_t^{(i)}) \sim \frac{1}{Z} P_{\theta}(F_t \mid [\text{Ca}^{2+}]_t^{(i)}) P_{\theta}([\text{Ca}^{2+}]_t^{(i)} \mid [\text{Ca}^{2+}]_{t-1}^{(i)}, n_t^{(i)}), \quad (\text{A.8})$$

which follows from having already sampled $n_t^{(i)}$ (as above, we have suppressed the explicit conditioning on $[\text{Ca}^{2+}]_{t-1}^{(i)}$ and F_t , for clarity). Using the rule that the product of two

APPENDIX A. DETAILS FOR CONSTRUCTING THE PARTICLE FILTERS

Gaussians results in a weighted Gaussian:

$$\begin{aligned} \frac{1}{\sqrt{2\pi}\sigma_1} \exp \left\{ -\frac{1}{2} \left(\frac{x - \mu_1}{\sigma_1} \right)^2 \right\} &\times \frac{1}{\sqrt{2\pi}\sigma_2} \exp \left\{ -\frac{1}{2} \left(\frac{x - \mu_2}{\sigma_2} \right)^2 \right\} \\ &= \frac{1}{Z} \frac{1}{\sqrt{2\pi}\varsigma} \exp \left\{ -\frac{1}{2} \frac{\left(x - \varsigma \left(\frac{\mu_1}{\sigma_1} + \frac{\mu_2}{\sigma_2} \right) \right)^2}{s} \right\}, \end{aligned} \quad (\text{A.9})$$

where $\varsigma = \left(\frac{1}{\sigma_1^2} + \frac{1}{\sigma_2^2} \right)^{-1}$, we obtain:

$$q_{\theta}^L([\text{Ca}^{2+}]_t^{(i)}) = \mathcal{N} \left([\text{Ca}^{2+}]_t^{(i)}; \Sigma_L^{(i)} \left(\frac{F_t}{1} + \frac{C_t^{(i)}}{\sigma_c \sqrt{\Delta}} \right), \Sigma_L^{(i)} \right), \quad (\text{A.10})$$

where $\Sigma_L^{(i)} = \left(1 + \frac{1}{\sigma_c^2 \Delta} \right)^{-1}$.

A.1.3 Computing the weights and resampling when sampling from $q_{\theta}^L([\text{Ca}^{2+}]_t^{(i)}, n_t^{(i)})$

At each time step, the weights are updated according to Eq. 2.8, which, for this model, may be expanded:

$$\tilde{w}_t^{(i)} = w_{t-1}^{(i)} P_{\theta}^L(F_t | [\text{Ca}^{2+}]_t^{(i)}) \frac{P_{\theta}([\text{Ca}^{2+}]_t^{(i)} | [\text{Ca}^{2+}]_{t-1}^{(i)}, n_t^{(i)}) P_{\theta}(n_t^{(i)})}{q_{\theta}^L(n_t^{(i)}) q_{\theta}^L([\text{Ca}^{2+}]_t^{(i)})}, \quad (\text{A.11})$$

where the three distributions in the numerator are given by Eqs. 2.1, 2.2, and 2.3. One resamples if the effective number of particles is too small (typically taken to be $N/2$ [84]):

$$\widehat{N_{eff}}^{-1} = \sum_{i=1}^N (w_t^{(i)})^2, \quad (\text{A.12})$$

which indicates whether too much of the weight is centered on too few particles [84].

A.2 Nonlinear observation particle filter

Replacing the linear observation distribution given by Eq. 2.5 with the nonlinear observation distribution given by Eq. 2.15 requires modifying $q(\mathbf{H}_t^{(i)})$. In particular, the rules governing the products of Gaussians cannot be used directly, as $P_\theta(F_t | [\text{Ca}^{2+}]_t)$ is not a Gaussian function of $[\text{Ca}^{2+}]_t$ (it is a Gaussian function of $S([\text{Ca}^{2+}]_t)$). Therefore, we approximate $P_\theta^{NL}(F_t | [\text{Ca}^{2+}]_t)$ using the standard Laplace approximation [31], to obtain:

$$P_\theta^{NL}(F_t | [\text{Ca}^{2+}]_t) \approx \mathcal{N}([\text{Ca}^{2+}]_t; \tilde{\mu}_t, \tilde{\sigma}_t^2), \quad (\text{A.13})$$

where $\tilde{\mu}$ and $\tilde{\sigma}^2$ denote the approximate mean and variance of this distribution. Having this approximation, we can then plug-in the approximate mean and variance into Eq. A.5 and A.9, to obtain $q_\theta^{NL}(n_t^{(i)})$ and $q_\theta^{NL}([\text{Ca}^{2+}]_t^{(i)})$ for this nonlinear observation model.

To generate the Laplace approximation to $P_\theta^{NL}(F_t | [\text{Ca}^{2+}]_t)$, we first compute a first-order Taylor series approximation of $g(x) = \alpha S([\text{Ca}^{2+}]_t) + \beta$, expanded around x :

$$g([\text{Ca}^{2+}]_t) \approx g(x) + ([\text{Ca}^{2+}]_t - x)g'(x) = F_t + ([\text{Ca}^{2+}]_t - x)g'(x), \quad (\text{A.14})$$

where $x = g^{-1}(F_t)$ and $g'(x) = dg(x)/dx$. Plugging this approximation into Eq. A.13, we have $\tilde{\mu}_t = g^{-1}(F_t)$ and $\tilde{\sigma}_t = (S([\text{Ca}^{2+}]_t) + \sigma_F)/g'(x)$, Plugging in the Hill function for $S(\cdot)$, and solving for x and $g'(x)$ yields:

$$x = g^{-1}(F_t) = \left(\frac{k_d(\beta - F_t)}{F_t - \beta - \alpha} \right)^{1/n} \quad (\text{A.15})$$

$$g'(x) = \left(\frac{k_d(\beta - F_t)}{F_t - \beta - \alpha} \right)^{1/n} \left(-\frac{k_d}{F_t - \beta - \alpha} - \frac{k_d(\beta - F_t)}{(F_t - \beta - \alpha)^2} \right) \frac{nk_d(\beta - F_t)}{F_t - \beta - \alpha}. \quad (\text{A.16})$$

APPENDIX A. DETAILS FOR CONSTRUCTING THE PARTICLE FILTERS

So, plugging Eqs. A.15 and A.16 into $\tilde{\mu}_t$ and $\tilde{\sigma}_t$, respectively, we can obtain a Gaussian function of $[\text{Ca}^{2+}]_t$ as in Eq. A.13. Note that this approximation holds whenever $[\text{Ca}^{2+}]_t$ is in some range, $lb < [\text{Ca}^{2+}]_t < ub$, where the lower and upper bounds (lb and ub , respectively) are functions of all the parameters: α , β , ξ , σ_F , n , and k_d . Given those parameters, we subjectively determine these limits. When the next observation is beyond those bounds, the likelihood function is approximately flat, so we sample according to the transition distribution, $P_\theta(\mathbf{H}_t | \mathbf{H}_{t-1})$ (i.e., use the prior sampler, ignoring the next observation). In practice, this is extremely rare.

Fig. A.1 shows the accuracy of this approximation, for a particular example. Importantly, this approximation need not be exact, as any distribution pushing the particles towards $P_\theta(\mathbf{H}_t | \mathbf{H}_{t-1}, \mathbf{O}_t)$ is an improvement over the prior sampler. We therefore use this approach to approximate $P_\theta^{NL}(F_t | [\text{Ca}^{2+}]_t)$.

A.2.1 Constructing $q_\theta^{NL}(n_t^{(i)})$

As for the linear case, we first evaluate the integral in Eq. A.3b, but we replace Eq. A.4 with Eq. A.13, yielding:

$$\mathcal{G}_\theta^{NL}(n_t^{(i)} | F_t) \stackrel{\text{def}}{=} \frac{1}{Z} \frac{1}{\sqrt{2\pi}(\tilde{\sigma}_t^2 + \sigma_c^2 \Delta)} \exp \left\{ -\frac{1}{2} \frac{(\tilde{\mu}_t - C_t^{(i)})^2}{(\tilde{\sigma}_t^2 + \sigma_c^2 \Delta)^2} \right\}. \quad (\text{A.17})$$

We may then construct $q_\theta^{NL}(n_t^{(i)})$ as we did for the linear case above, but replacing $\mathcal{G}_\theta^L(n_t^{(i)} | F_t)$ in Eq. A.7 with $\mathcal{G}_\theta^{NL}(n_t^{(i)} | F_t)$.

APPENDIX A. DETAILS FOR CONSTRUCTING THE PARTICLE FILTERS

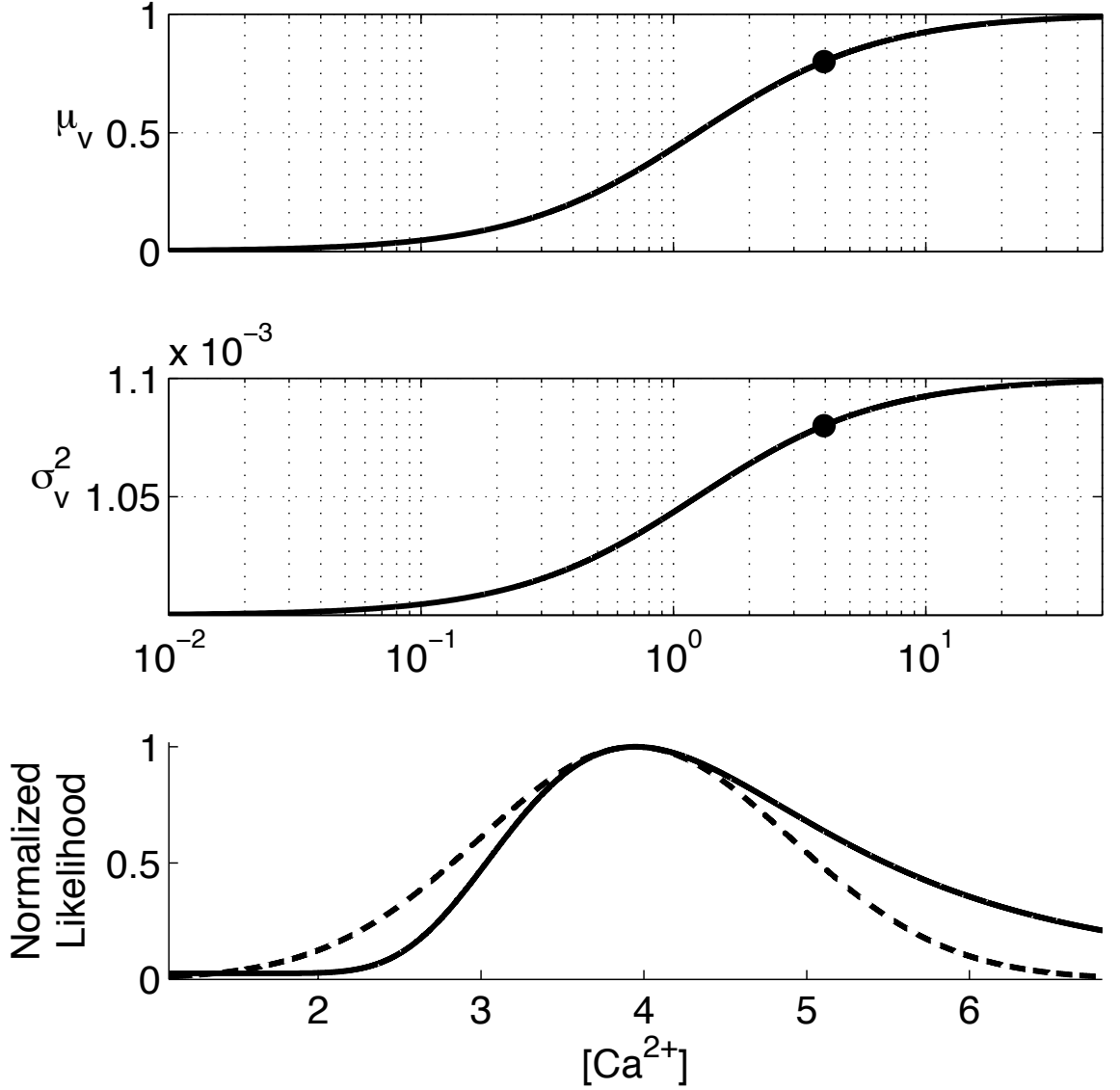


Figure A.1: Laplace approximation of observation distribution: Gaussian likelihood approximation when modeling the relationship between $[\text{Ca}^{2+}]_t$ and F_t using Eqs. 2.13 and 2.14. To sample conditioned on the next observation, we approximate the nonlinear observation distribution (Eq. 2.15) to be a Gaussian function of $[\text{Ca}^{2+}]_t$. Top panel: Expected F_t for a range of possible values of $\ln[\text{Ca}^{2+}]_t$ (solid line). Middle panel: Same as top panel but for variance. Bottom panel: Given a fluorescence observation, $F_t = 0.8$, the actual likelihood of $[\text{Ca}^{2+}]_t$ (solid line) and Gaussian approximation to it (dotted line), both normalized for comparison purposes. The circles in the top panel and middle panel show the μ_{F_v} and σ_{F_v} for $[\text{Ca}^{2+}]_v$ at the mean of the distribution plotted in the bottom panel.

A.2.2 Constructing $q_{\theta}^{NL}([\mathbf{Ca}^{2+}]_t^{(i)})$

Again, having the approximation in Eq. A.13, constructing $q_{\theta}^{NL}([\mathbf{Ca}^{2+}]_t^{(i)})$ follows directly from the linear case, by substituting Eq. A.13 for $P_{\theta}(F_t | [\mathbf{Ca}^{2+}]_t^{(i)})$ into Eq. A.8:

$$q_{\theta}^{NL}([\mathbf{Ca}^{2+}]_t^{(i)}) = \mathcal{N} \left([\mathbf{Ca}^{2+}]_t^{(i)}; \Sigma_{NL}^{(i)} \left(\frac{\tilde{\mu}_t}{\tilde{\sigma}_t} + \frac{C_t^{(i)}}{\sigma_c \sqrt{\Delta}} \right), \Sigma_{NL}^{(i)} \right), \quad (\text{A.18})$$

where $\Sigma_{NL}^{(i)} = \left(\frac{1}{\tilde{\sigma}_t^2} - \frac{1}{\sigma_c^2 \Delta} \right)^{-1}$.

A.2.3 Computing the weights and reweighting when sam-

pling from $q_{\theta}^{NL}([\mathbf{Ca}^{2+}]_t^{(i)}, n_t^{(i)})$

Computing the weights for the this nonlinear observation particle filter proceeds as in Eq. A.11, but replacing $q_{\theta}^L(\cdot)$ with $q_{\theta}^{NL}(\cdot)$. We again use Eq. A.12 to reweight when appropriate.

A.3 Superresolution particle filter

The goal of the superresolution particle filter is to sample spike times in such a way as to be able to infer when within each image frame a spike occurs, as opposed to simply whether a spike occurs within an image frame. Importantly, this requires a time discretization more fine than the image frame rate admits, i.e., we let $\Delta = 1/(d \times \text{frame rate})$, where d sets the number of time steps per image frame. This strategy might be desirable for a

APPENDIX A. DETAILS FOR CONSTRUCTING THE PARTICLE FILTERS

number of reasons. First, often the image capture hardware or software drops frames, so one would like to be able to handle dropped frames in a natural way. But perhaps more importantly, imaging is often the bottleneck for temporal resolution. When using 2-photon microscopy, imaging is “intermittent” due to scanning. This follows because scanning each line typically only takes about 2 msec, while scanning the entire frame takes on the order of 50 – 500 msec (depending on how many scan lines one chooses per frame). Thus, one might observe a particular cell for only 2 msec at a time every $d \times 2$ msec (assuming d scan lines, and the cell is only observed in 1 of those lines). In such a scenario, a reasonable model would be:

$$P_{\theta}^S(F_t | [\text{Ca}^{2+}]_t) \stackrel{\text{def}}{=} \begin{cases} \mathcal{N}(F_t; \mu_{2P}, \sigma_{2P}^2) & \text{if } t/d \in \mathbb{Z} \\ 1 & \text{otherwise,} \end{cases} \quad (\text{A.19})$$

where $\mu_{2P} = \alpha S([\text{Ca}^{2+}]_t) + \beta$, $\sigma_{2P} = \xi S([\text{Ca}^{2+}]_t) + \sigma_F$, and \mathbb{Z} is the set of all positive integers. Alternately, if one is using either epifluorescence or confocal imaging, images might not be intermittent, but rather, slow due to the relatively slow frame rates obtainable with today’s cameras (i.e., ~ 50 Hz). In such a scenario, while a similar discretization of time would be appropriate, the observation model (Eq. A.19), must be modified to reflect that the camera would be integrating the photons over the entire image frame time period. In particular, we would replace $S([\text{Ca}^{2+}]_t)$ with the integrated photon count since the previous observation, $\sum_{s=t}^{t+d} S([\text{Ca}^{2+}]_s)$. We therefore assume $P_{\theta}^S(\cdot)$ is defined as in Eq. A.19 below without loss of generality (note, however, that the below sampler is not optimal for non-scanned images).

APPENDIX A. DETAILS FOR CONSTRUCTING THE PARTICLE FILTERS

We could use the prior sampler, which would ignore Eq. A.19 when generating samples, and then weight the samples as before at observation time steps. This approach, however, becomes even more inefficient when subsampling the step size. Fig. A.2 shows an explanatory example of a single spontaneous spike underlying intermittent observations. Because the probability of generating a spike in any time bin is relatively low when using the prior sampler, no particles actually sampled a spike, and therefore the inferred distribution misses the spike. However, by conditioning on the next observation (i.e., using the one-observation-ahead sampler), particles sample spikes in the appropriate time bin, and the inferred distribution is then more accurate. Below, we provide details for constructing and implementing the one-observation-ahead sampler when observations are intermittent.

A.3.1 Superresolution one-observation-ahead sampling intuition

The key to one-observation-ahead sampling — when observations are intermittent — is to sample spikes between observations conditioned on the next observation. In other words, if v is the time of the next observation, we would like to sample from:

$$\begin{aligned} q(\mathbf{H}_t) &= P_{\boldsymbol{\theta}}(\mathbf{H}_t | \mathbf{H}_{t-1}^{(i)}, \mathbf{O}_v) \propto P_{\boldsymbol{\theta}}^S(\mathbf{O}_v | \mathbf{H}_t) P_{\boldsymbol{\theta}}(\mathbf{H}_t | \mathbf{H}_{t-1}^{(i)}) \\ q_{\boldsymbol{\theta}}^S([\text{Ca}^{2+}]_t^{(i)}, n_t^{(i)}) \\ &= P_{\boldsymbol{\theta}}^{NL}(F_v | [\text{Ca}^{2+}]_t^{(i)}) P_{\boldsymbol{\theta}}([\text{Ca}^{2+}]_t^{(i)} | [\text{Ca}^{2+}]_{t-1}^{(i)}, n_t^{(i)}) P_{\boldsymbol{\theta}}(n_t^{(i)}), \end{aligned} \quad (\text{A.20})$$

where Eq. A.20 only differs from Eq. A.2 by replacing $P_{\boldsymbol{\theta}}^L(F_t | [\text{Ca}^{2+}]_t)$ with $P_{\boldsymbol{\theta}}^{NL}(F_v |$

APPENDIX A. DETAILS FOR CONSTRUCTING THE PARTICLE FILTERS

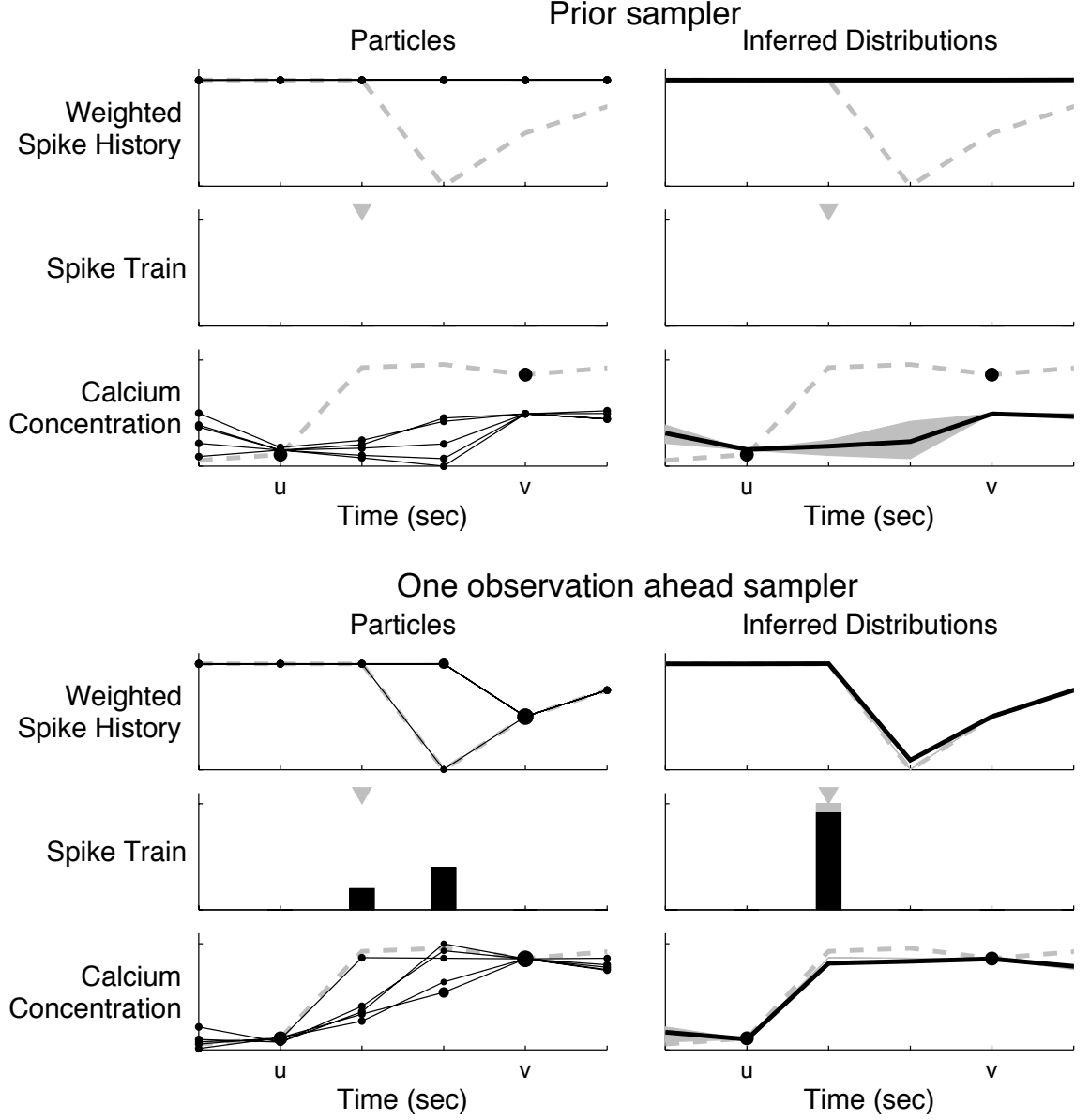


Figure A.2: Sampling strategies: the one-observation-ahead sampler outperforms the prior sampler. The top left panels show the prior sampler (i.e., sampling using the transition distribution, $P_{\theta}(\mathbf{H}_t | \mathbf{H}_{t-1})$). Observations were made essentially noise free at times u and v . At each time step, for each particle, a value for \mathbf{h}_t was sampled first (top panels; unitless), then n_t (second panels; # of spikes), then $[\text{Ca}^{2+}]_t$ (third panels; μM). The size of the dots is proportional to the weights for each particle at each time step. Note that for the prior sampler, they are all the same, which follows from Eq. A.1 and the fact the no observations are made between u and v . The height of the bars is proportional to the number of sampled spikes at that time. At observation times, one resamples according to the particle weights, $w_t^{(i)}$. The probability of sampling a spike was low here, so no spikes were actually sampled by the prior sampler at these times. The top right panels show the resulting mean and variances. The bottom left panels show that the one-observation-ahead sampler is more efficient. Particles sampled a spike at the actual spike time, resulting in an accurate spike time inference (right). No stimulus was present. Parameters as in Fig. 2.6.

APPENDIX A. DETAILS FOR CONSTRUCTING THE PARTICLE FILTERS

$[\text{Ca}^{2+}]_t$), which may be thought of as the probability of the next observation, F_v , given the current calcium concentration, $[\text{Ca}^{2+}]_t$. Thus, to sample from Eq. A.20, we must compute $P_{\theta}^{NL}(F_v \mid [\text{Ca}^{2+}]_t)$ for all t starting at the last observation, until v . We start by letting $t = v$, which is identical to the non-intermittent case. Then, we recurse backwards, computing $P_{\theta}^{NL}(F_v \mid [\text{Ca}^{2+}]_s)$ for s between $v - 1$ and $v - d$. Below, we fill in the details.

At time v , we can approximate $P_{\theta}^{NL}(F_v \mid [\text{Ca}^{2+}]_v)$ using Eqs. 2.13 and 2.14. Assuming we wish to use a nonlinear observation model as above, we approximate this distribution as a Gaussian function of $[\text{Ca}^{2+}]_t$, using Eq. A.13. At $t = v - 1$, the neuron could either have spiked or not. If the neuron did not spike, to move backward from $[\text{Ca}^{2+}]_v$ to $[\text{Ca}^{2+}]_{v-1}$, calcium should do the inverse of decay (cf. Eq. A.22). This is the standard backward recursion, familiar from the Hidden Markov Model literature [93]. However, if the neuron did spike, $[\text{Ca}^{2+}]_{v-1}$ should be $A \mu\text{M}$ below $[\text{Ca}^{2+}]_v$. In either case, because the noise on the $[\text{Ca}^{2+}]_t$ transitions is Gaussian, the distribution maintains its Gaussianity, and its variance slightly increases. Thus, the distribution of $[\text{Ca}^{2+}]_{v-1}$ is a *mixture of Gaussians*. At $v - 1$, we have a *2-component mixture*, one component for $n_{v-1} = 1$ and one for $n_{v-1} = 0$. The component coefficient (probability of being in that component), $a_{n,v-1}$, is the expected probability of spiking or not. The left panel of Fig. A.3 depicts the Gaussian mixture for several time steps preceeding an observation. At time $t = v$, $P_{\theta}^{NL}(F_v \mid [\text{Ca}^{2+}]_v)$ is approximated as a Gaussian. At time $t = v - 1$, the distribution is a mixture of two Gaussians. The top Gaussian's mean is centered around the mean of the Gaussian at $t = v$. This follows from the fact that the calcium time constant is much larger than the step size,

APPENDIX A. DETAILS FOR CONSTRUCTING THE PARTICLE FILTERS

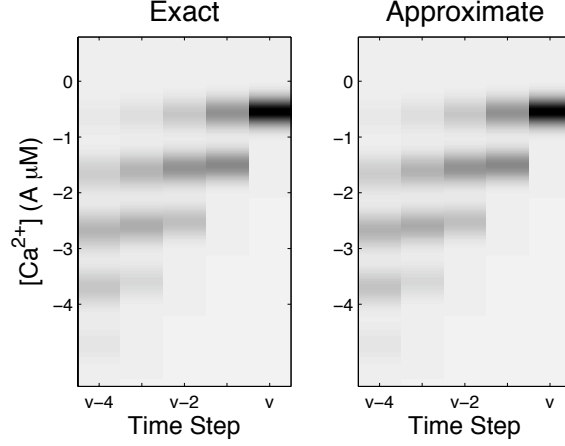


Figure A.3: Mixture approximation: approximate distribution closely matches exact (analytical) distribution. Approximating the 2^{v-u} component mixture with a $v - u + 1$ component mixture. Left panel: The exact distribution is a mixture, with 2^{v-u} components. Right panel: We approximate this mixture with only $v - u + 1$ -components. Note that the two panels are visually extremely similar.

$\tau \gg \Delta$; therefore, the amount of decay (or rather, inverse decay) in a few time steps is relatively small. The other Gaussian's mean is centered around $A \mu\text{M}$ below the top one, corresponding to where the calcium would be at $t = v - 1$ if a spike occurred at that time step, forcing $[\text{Ca}^{2+}]_t$ to jump up by $A \mu\text{M}$ in the next time step.

Recurring backward one more step yields a 4-component mixture, as each component in the mixture at $v - 1$ could have gotten there either from the neuron spiking or not at time $v - 2$. The coefficient for each of the 4 components is proportional to the expected probability of having that particular *sequence* of spikes, i.e., at $v - 2$, we have 4 possible sequences: (00), (01), (10), and (11), corresponding to no spikes, only spiking at time $v - 1$, only spiking at time $v - 2$ and spiking at both $v - 1$ and $v - 2$, respectively.

Note that at $v - 2$, two of the components nearly completely overlap. In fact, those two

APPENDIX A. DETAILS FOR CONSTRUCTING THE PARTICLE FILTERS

components correspond to (01) and (10), i.e., the sequences with exactly one spike. One can therefore approximate the two components corresponding to a single spike at $v - 2$ as just one Gaussian component. The right panel of Fig. A.3 shows this approximation: at $t = v - 2$, the distribution in the right panel is a mixture of only three Gaussians. The middle Gaussian has a mean and variance chosen to approximate the two Gaussians that are nearly overlapping at $t = v - 2$ (cf. Eqs. A.29 and A.30, below). It should be clear that this approximation is very accurate. Note that at $t = v$ and $t = v - 1$, the left and right panels are identical, as there need not be any approximation.

More generally, at any time $v - t$, all the components resulting from the same number of spikes between t and v can be combined into a single component. One must simply take care to modify the component weights, means, and variances appropriately. Upon doing so, at time t , instead of a mixture with 2^{v-t} components, we are left with a mixture of $v - t + 1$ components (i.e., one component per possible number of spikes until time v). For instance, assuming that $d = 20$, we obtain a $2^{20} \approx 10^6$ component mixture in the no-approximation situation, versus a 21 component mixture when using our approximation, a four order of magnitude reduction in computational load. Comparing the left and right panels for $t = v - 3$ and $t = v - 4$ shows the accuracy of this approximation going back 3 and 4 time steps, respectively. Because this approximation is so accurate, we use this approximation for $P_{\theta}^{NL}(F_v \mid [\text{Ca}^{2+}]_t)$.

A.3.2 Computing $P_{\theta}^{NL}(F_v \mid [\mathbf{Ca}^{2+}]_t)$ for all $t \in (u, v)$

A.3.2.1 Initializing $P_{\theta}^{NL}(F_v \mid [\mathbf{Ca}^{2+}]_v)$

If u is the time of the last observation, and v is the time of the next observation, we initialize $P_{\theta}^{NL}(F_v \mid [\mathbf{Ca}^{2+}]_v)$ using the same Laplace approximation as in the previous section:

$$P_{\theta}^{NL}(F_v \mid [\mathbf{Ca}^{2+}]_v) \approx \mathcal{N}([\mathbf{Ca}^{2+}]_v; \tilde{\mu}_v, \tilde{\sigma}_v^2). \quad (\text{A.21})$$

A.3.2.2 Recursing backwards

At $v - 1$, we use the following backward recursion:

$$P_{\theta}^{NL}(F_v \mid [\mathbf{Ca}^{2+}]_{v-1}) = \sum_{n=0,1} a_{n,v-1} \int P_{\theta}^{NL}(F_v \mid [\mathbf{Ca}^{2+}]_v) P_{\theta}([\mathbf{Ca}^{2+}]_v \mid [\mathbf{Ca}^{2+}]_{v-1}, n_v = n) d[\mathbf{Ca}^{2+}]_v, \quad (\text{A.22})$$

to generate the two-component Gaussian the mixture model corresponding to the neuron spiking or not at time $v - 1$. The component coefficients, $\{a_{1,v-1}, a_{0,v-1}\}$ are the expected probabilities of spiking or not, $E[n_{v-1}=1]$ and $E[n_{v-1}=0]$, respectively, given by Eq. 2.3. The transition distributions, $P_{\theta}([\mathbf{Ca}^{2+}]_v \mid [\mathbf{Ca}^{2+}]_{v-1}, n_v = n)$ for $n_v = 0$ and $n_v = 1$ are given by:

$$P_{\theta}([\mathbf{Ca}^{2+}]_v \mid [\mathbf{Ca}^{2+}]_{v-1}, n_v) = \mathcal{N}([\mathbf{Ca}^{2+}]_v; [\mathbf{Ca}^{2+}]_{v-1} - \Delta/\tau([\mathbf{Ca}^{2+}]_{v-1} - [\mathbf{Ca}^{2+}]_b) + An_v, \sigma_c^2 \Delta), \quad (\text{A.23})$$

APPENDIX A. DETAILS FOR CONSTRUCTING THE PARTICLE FILTERS

where either $n_v = 0$ or $n_v = 1$, which follows from Eq. 2.2. We now have all parts necessary to evaluate the integral in Eq. A.22, to get a Gaussian distribution in $[\text{Ca}^{2+}]_{v-1}$.

First, simply write down the integral, substituting in the known distributions:

$$\begin{aligned} & \int P_{\theta}^{NL}(F_v \mid [\text{Ca}^{2+}]_v) P_{\theta}([\text{Ca}^{2+}]_v \mid [\text{Ca}^{2+}]_{v-1}, n_v = n) d[\text{Ca}^{2+}]_v \\ &= \int \mathcal{N}([\text{Ca}^{2+}]_v; \tilde{\mu}_v, \tilde{\sigma}_v^2) \times \mathcal{N}([\text{Ca}^{2+}]_v; [\text{Ca}^{2+}]_{v-1} - \Delta/\tau([\text{Ca}^{2+}]_{v-1} - [\text{Ca}^{2+}]_b) + An_v, \sigma_c^2 \Delta). \end{aligned} \quad (\text{A.24})$$

Using the fact that the integral of two Gaussian functions of the same variable yields a Gaussian (cf. Eq. A.5), we can evaluate the integral in Eq. A.24:

$$\frac{1}{\sqrt{2\pi(\tilde{\sigma}_v^2 + \sigma_c^2 \Delta)}} \exp \left\{ -\frac{1}{2} \frac{(\tilde{\mu}_v - \chi(n_v))^2}{\tilde{\sigma}_v^2 + \sigma_c^2 \Delta} \right\}. \quad (\text{A.25})$$

where $\chi(n_v) = ([\text{Ca}^{2+}]_{v-1} - \frac{\Delta}{\tau}([\text{Ca}^{2+}]_{v-1} - [\text{Ca}^{2+}]_b) + An_v)$. Rewriting this as a Gaussian function of $[\text{Ca}^{2+}]_{v-1}$, we have:

$$\frac{1}{Z} \mathcal{N}([\text{Ca}^{2+}]_{v-1}; \tilde{\mu}_v^S(n), (\tilde{\sigma}_v^S)^2), \quad (\text{A.26})$$

where $\tilde{\mu}_v^S(n) = (\tilde{\mu}_v - An_v - \frac{\Delta}{\tau}[\text{Ca}^{2+}]_b)/(1 - \frac{\Delta}{\tau})$, $(\tilde{\sigma}_v^S)^2 = (\tilde{\sigma}_v^2 + \sigma_c^2 \Delta)/(1 - \frac{\Delta}{\tau})^2$, and Z is a normalization factor (which is only a function of τ and Δ). Plugging this result back into Eq. A.22 yields:

$$P_{\theta}^{NL}(F_v \mid [\text{Ca}^{2+}]_{v-1}) = \sum_{n=0,1} a_{n,v-1} \mathcal{N}([\text{Ca}^{2+}]_{v-1}; \tilde{\mu}_v^S(n), (\tilde{\sigma}_v^S)^2), \quad (\text{A.27})$$

where we have dropped Z because the component coefficients, $a_{1,v-1}$ and $a_{0,v-1}$, set the appropriate weights for the above mixture (and Z does not depend on the data or the mixture

APPENDIX A. DETAILS FOR CONSTRUCTING THE PARTICLE FILTERS

identity). This provides the intuition for a more general backward recursion:

$$P_{\theta}^{NL}(F_v \mid [\text{Ca}^{2+}]_{t-1}) = \sum_{n=0,1} a_{n,t-1} \sum_{m=1}^{2^{v-t}} a_{mt} \mathcal{N}([\text{Ca}^{2+}]_{t-1}; \tilde{\mu}_{mt}^S(n), (\tilde{\sigma}_t^S)^2), \quad (\text{A.28})$$

where m indexes one of the 2^{v-t} possible spike trains between t and v , corresponding to one component of the mixture, and $\tilde{\mu}_{mt}^S(n) = (\tilde{\mu}_{mt} - An_t - \frac{\Delta}{\tau}[\text{Ca}^{2+}]_b)/(1 - \frac{\Delta}{\tau})$. Each component coefficient, a_{mt} , is the probability of sampling the particular spike train indexed by m , at time t . Similarly, $\tilde{\mu}_{mt}$ is the expected value for $[\text{Ca}^{2+}]_t$ given F_v and a particular spike train indexed by m , computed recursively using Eq. A.28. The variance of each component is the same because the variance is not a function of the data or whether the neuron spikes.

A.3.2.3 Approximating the 2^{v-t} component mixture

To reduce this mixture from an intractable 2^{v-t} components to a tractable $v - t + 1$ components, we approximate all the components at time t conditioned on the same number of spikes as a single component:

$$\sum_{m \in \mathcal{M}} a_{mt} \mathcal{N}([\text{Ca}^{2+}]_t; \tilde{\mu}_{mt}^S(n), (\tilde{\sigma}_t^S)^2) \approx a_{m^*t} \mathcal{N}([\text{Ca}^{2+}]_t; \hat{\mu}_{m^*t}, \hat{\sigma}_{m^*t}^2), \quad (\text{A.29})$$

where $\mathcal{M} = \sum_{s=t}^v n_s = m^*$, $a_{m^*t} = \sum_m a_{mt}$, $\hat{\mu}_{m^*t} = \sum_m a_{mt} \tilde{\mu}_{mt}$, and $\hat{\sigma}_{m^*t}^2 = \hat{\sigma}_t^2 + \sum_m a_{mt} (\tilde{\mu}_{mt} - \hat{\mu}_{m^*t})^2$. Thus, we must compute these three terms for all $m^* = 0, \dots, v - t - 1$ and all $t = u + 1, \dots, v - 2$ to sample from these mixtures at each time step between observations (this approximation is only necessary when $t < v - 1$, because otherwise we simply keep the 2-mixture Gaussian). The approximation in Eq. A.29 is good

APPENDIX A. DETAILS FOR CONSTRUCTING THE PARTICLE FILTERS

because the distribution of calcium is governed largely by the number of spikes since the last observation, and only somewhat modulated by the particular spike train in that time period. Thus, in other words, for each time step, we approximate:

$$P_{\theta}^{NL}(F_v \mid [\text{Ca}^{2+}]_t) \approx \hat{P}_{\theta}(F_v \mid [\text{Ca}^{2+}]_t) = \sum_{m^*=0}^{v-t} a_{m^*t} \mathcal{N}([\text{Ca}^{2+}]_t; \hat{\mu}_{m^*t}, \hat{\sigma}_{m^*t}^2). \quad (\text{A.30})$$

A.3.3 Superresolution sampling details

Having constructed an approximation to $P_{\theta}^{NL}(F_v \mid [\text{Ca}^{2+}]_t)$, we may now plug that into Eq. A.20, to construct the distributions from which we actually sample each of the hidden states. The spike history terms are sampled from the transition distribution, because most of their variance derives from previous spikes, and not observations. So we need only construct a sampling distribution for n_t and $[\text{Ca}^{2+}]_t$.

A.3.3.1 Superresolution sampling spikes

Sampling spikes for the intermittent case follows from Eq. A.3b, but we replace $P_{\theta}(F_t \mid [\text{Ca}^{2+}]_t^{(i)})$ with $\hat{P}_{\theta}(F_v \mid [\text{Ca}^{2+}]_t)$:

$$\begin{aligned} q(n_t^{(i)}) &= \frac{1}{Z} P_{\theta}(n_t^{(i)}) \int P_{\theta}([\text{Ca}^{2+}]_t \mid [\text{Ca}^{2+}]_{t-1}^{(i)}, n_t^{(i)}) \\ &\quad \times \hat{P}_{\theta}(F_v \mid [\text{Ca}^{2+}]_t) d[\text{Ca}^{2+}]_t, \end{aligned} \quad (\text{A.31})$$

As in Eq. A.3b, one can compute the above integral using Eq. A.5, to generate a Gaussian

APPENDIX A. DETAILS FOR CONSTRUCTING THE PARTICLE FILTERS

for each component in the mixture of $\hat{P}_\theta(F_v | [\text{Ca}^{2+}]_t)$:

$$\mathcal{G}_\theta^{m^*}(n_t^{(i)} | F_v) \stackrel{\text{def}}{=} \frac{1}{\sqrt{2\pi(\hat{\sigma}_{m^*t}^2 + \sigma_c^2\Delta)}} \exp \left\{ -\frac{1}{2} \left(\frac{\hat{\mu}_{m^*t} - C_t^{(i)}}{\hat{\sigma}_{m^*t}^2 + \sigma_c^2\Delta} \right)^2 \right\}, \quad (\text{A.32})$$

which we compute for $n_t^{(i)} = 0$ and $n_t^{(i)} = 1$ (recalling that $C_t^{(i)}$ is implicitly a function of $n_t^{(i)}$, as defined in Eq. A.6). Thus, for each particle, one samples from:

$$\tilde{q}_\theta^S(n_t^{(i)}) = \mathcal{B}(n_t^{(i)}; p\Delta) \sum_{m^*=0}^{v-t} a_{m^*t} \mathcal{G}_\theta^{m^*}(n_t^{(i)} | F_v) \quad (\text{A.33a})$$

$$q_\theta^S(n_t^{(i)}) = \frac{\tilde{q}_\theta^S(n_t^{(i)})}{\sum_{n_t^{(i)}=\{0,1\}} \tilde{q}_\theta^S(n_t^{(i)})}. \quad (\text{A.33b})$$

where $q_\theta^S(n_t^{(i)})$ is implicitly conditioned on both $[\text{Ca}^{2+}]_{t-1}^{(i)}$ and F_v .

A.3.3.2 Superresolution sampling calcium

Sampling calcium in the intermittent case follows from Eq. A.8, but we replace $P_\theta(F_t | [\text{Ca}^{2+}]_t^{(i)})$ with $\hat{P}_\theta(F_v | [\text{Ca}^{2+}]_t)$:

$$\begin{aligned} [\text{Ca}^{2+}]_t^{(i)} \sim q_\theta^S([\text{Ca}^{2+}]_t^{(i)}) &= \hat{P}_\theta(F_v | [\text{Ca}^{2+}]_t) P_\theta([\text{Ca}^{2+}]_t^{(i)} | [\text{Ca}^{2+}]_{t-1}^{(i)}, n_t^{(i)}) \\ &= \sum_{m^*=n_t^{(i)}}^{v-t} a_{m^*t} \mathcal{N}([\text{Ca}^{2+}]_t; \mu_{cm^*t}^{(i)}, \sigma_{cm^*t}^2), \end{aligned} \quad (\text{A.34})$$

where $q_\theta^S([\text{Ca}^{2+}]_t^{(i)})$ is implicitly conditioned on $n_t^{(i)}$, $[\text{Ca}^{2+}]_{t-1}^{(i)}$, and F_v , and we let:

$$\sigma_{cm^*t}^{-2} = \hat{\sigma}_{m^*t}^{-2} + (\sigma_c^2\Delta)^{-2} \quad (\text{A.35})$$

$$\mu_{cm^*t}^{(i)} = \sigma_{cm^*t}^2 \left(\frac{\hat{\mu}_{m^*t}}{\hat{\sigma}_{m^*t}^2} + \frac{C_t^{(i)}}{\sigma_c^2\Delta} \right). \quad (\text{A.36})$$

To sample from this mixture, one first samples a component according to its coefficient a_{m^*t} , and then samples from the Gaussian corresponding to that component. Notice,

APPENDIX A. DETAILS FOR CONSTRUCTING THE PARTICLE FILTERS

however, that the sum in Eq A.34 starts at $n_t^{(i)}$, because if $n_t^{(i)} = 1$, then the component corresponding to *zero* spikes between t and v should not be considered for that particle.

A.3.3.3 Computing the weights and reweighting when sampling from

$$q_{\theta}^S([\mathbf{Ca}^{2+}]_t^{(i)}, n_t^{(i)})$$

Computing the weights for the this superresolution particle filter proceeds as in Eq. A.11, but replacing $q_{\theta}^L(\cdot)$ with $q_{\theta}^S(\cdot)$. We again use Eq. A.12 to reweight when appropriate.

A.4 GLM particle filter

Until now, we have assumed that the spiking probability was independent of both the stimulus and previous spikes. However, if we replace Eq. 2.3 with a GLM (such as described by Eqs. 2.16 – 2.18), we obtain a more general model. In such a scenario, the transition distribution becomes:

$$P_{\theta}(\mathbf{H}_t | \mathbf{H}_{t-1}^{(i)}) = P_{\theta}([\mathbf{Ca}^{2+}]_t | [\mathbf{Ca}^{2+}]_{t-1}^{(i)}, n_t^{(i)}) P_{\theta}(n_t^{(i)} | \mathbf{h}_t^{(i)}) P_{\theta}(\mathbf{h}_t^{(i)} | n_{t-1}^{(i)}, \mathbf{h}_{t-1}^{(i)}), \quad (\text{A.37})$$

Thus, the one-observation-ahead sampler must change to reflect the spike history terms. Specifically, now n_t depends on $\mathbf{h}_t^{(i)}$, which implies that $\mathbf{h}_t^{(i)}$ must be sampled *before* n_t . While one could sample the spike histories conditioned on the observations (i.e., from the one-observation-ahead sampler), because they are functions of n_{t-1} , the variance mostly

APPENDIX A. DETAILS FOR CONSTRUCTING THE PARTICLE FILTERS

comes from whether the neuron spiked in the previous time step. Thus, they can simply be sampled from their transition distributions without much loss of efficiency. Therefore, we sample each spike history term from $P_{\theta}(h_{l,t}|h_{l,t-1}^{(i)})$, which is given by Eq. 2.18.

Having sampled $\mathbf{h}_t^{(i)}$ for each particle, we must now sample n_t conditionally:

$$\tilde{q}_{\theta}^G(n_t^{(i)}) = \mathcal{B}\left(n_t^{(i)}; 1 - e^{f(b + \mathbf{k}'\mathbf{x}_t + \boldsymbol{\omega}'\mathbf{h}_t^{(i)})}\right) \sum_{m^*=0}^{v-t} \tilde{a}_{m^*t} \mathcal{G}_{\theta}^{m^*}(n_t^{(i)}|F_v) \quad (\text{A.38a})$$

$$q_{\theta}^G(n_t^{(i)}) = \frac{\tilde{q}_{\theta}^G(n_t^{(i)})}{\sum_{n_t^{(i)}=\{0,1\}} \tilde{q}_{\theta}^G(n_t^{(i)})}, \quad (\text{A.38b})$$

where $\mathcal{G}_{\theta}^{m^*}(n_t^{(i)}|F_v)$ is from Eq. A.32, and \tilde{a}_{m^*t} is an approximation to a_{m^*t} , necessary because the spike history terms make a_{m^*t} not analytically tractable (because they have not yet been sampled for times after t). Consider computing $a_{1,v-1}$ in the absence of spike history terms:

$$a_{1,v-1} = 1 - e^{-f(b + \mathbf{k}'\mathbf{x}_{v-1})\Delta}. \quad (\text{A.39})$$

The probability of not spiking is simply $a_{0,v-1} = 1 - a_{1,v-1}$. When spike history terms *are* present, $f(\cdot)$ would also be a function of \mathbf{h}_{v-1} , which has not yet been sampled. We therefore must recursively approximate the expected value for each spike history term using:

$$E[h_{l,t}] = E\left[(1 - \Delta/\tau_{hl})h_{l,t-1} + n_{t-1} + \sigma_h\sqrt{\Delta}\varepsilon_t\right] = (1 - \Delta/\tau_{hl})E[h_{l,t-1}] + E[n_{t-1}], \quad (\text{A.40})$$

for all $t \in (u, v)$, where u is the time of the previous observation. Then, we let

$$\tilde{a}_{1,t} \approx E[n_t = 1] \approx 1 - e^{f(b + \mathbf{k}'\mathbf{x}_t + \boldsymbol{\omega}'E[\mathbf{h}_t])\Delta}, \quad (\text{A.41})$$

APPENDIX A. DETAILS FOR CONSTRUCTING THE PARTICLE FILTERS

and $\tilde{a}_{0,t} = 1 - \tilde{a}_{1,t}$. By iterating between Eqs. A.40 and A.41 for $t = u, \dots, v$, we get the expected probability of the neuron spiking at any time.

Sampling calcium proceeds as in Eq. A.34, having now sampled the spikes conditioned on the spike history terms. Computing the weights proceeds as in the superresolution case, as both the numerator and denominator of Eq. A.11 get multiplied by $P_{\theta}(\mathbf{h}_t^{(i)} | \mathbf{h}_{t-1}^{(i)})$, so they cancel one another.

Appendix B

Learning the parameters

In this appendix, we describe how to estimate all of the parameters mentioned in the main text (i.e., including the generalizations). For brevity, we use the following notation:

$$J_{t,t-1}^{(i,j)} = P_{\theta}(\mathbf{H}_t^{(i)}, \mathbf{H}_{t-1}^{(j)} | \mathbf{O}_{1:T})$$

$$M_t^{(i)} = P_{\theta}(\mathbf{H}_t^{(i)} | \mathbf{O}_{1:T}).$$

For learning all the parameters governing the transition distribution, we make use of the following identity for our model:

$$\ln P_{\theta}(\mathbf{H}_t^{(i)} | \mathbf{H}_{t-1}^{(j)}) = \ln P_{\theta}([\text{Ca}^{2+}]_t^{(i)} | [\text{Ca}^{2+}]_{t-1}^{(j)}, n_t^{(i)}) + \ln P_{\theta}(n_t^{(i)} | \mathbf{h}_t^{(i)}) + \ln P_{\theta}(\mathbf{h}_t^{(i)} | \mathbf{h}_{t-1}^{(j)}), \quad (\text{B.1})$$

which follows from Eqs. 2.2 and 2.16 – 2.18. Therefore, we can maximize the likelihood with respect to the parameters governing any of the hidden states independently of the parameters governing the other hidden states. For example, maximizing the likelihood with respect to $\{b, \mathbf{k}, \mathbf{w}\}$ depends only on $P_{\theta}(n_t | \mathbf{h}_t)$.

B.1 Spike Rate Parameters

To compute the maximum likelihood estimates of the spike rate parameters, define \mathcal{F} be the set of index pairs, (i, t) , for which particle i spikes at time t . Then, by letting $y_t = b + \mathbf{k}'\mathbf{x}_t + \boldsymbol{\omega}'\mathbf{h}_t$, and plugging in Eqs. 2.16 and 2.18 into 2.12, and maximizing with respect to $\{b, \mathbf{k}, \boldsymbol{\omega}\}$, we have:

$$\begin{aligned} \{\widehat{b}, \widehat{\mathbf{k}}, \widehat{\boldsymbol{\omega}}\} &= \operatorname{argmax}_{\{b, \mathbf{k}, \boldsymbol{\omega}\}} \sum_{t=1}^T \sum_{i,j=1}^N J_{t,t-1}^{(i,j)} (\ln P_{\boldsymbol{\theta}}(n_t^{(i)} | \mathbf{h}_t^{(i)})) \\ &= \operatorname{argmax}_{b, \mathbf{k}, \boldsymbol{\omega}} \sum_{(i,t) \in \mathcal{F}} M_t^{(i)} \ln \left(1 - e^{f(b + \mathbf{k}'\mathbf{x}_t + \boldsymbol{\omega}'\mathbf{h}_t^{(i)})\Delta} \right) + \sum_{(i,t) \notin \mathcal{F}} M_t^{(i)} f(b + \mathbf{k}'\mathbf{x}_t + \boldsymbol{\omega}'\mathbf{h}_t^{(i)})\Delta, \end{aligned} \quad (\text{B.2})$$

where $\mathbf{H}_t^{(i)}$ has been integrated out of $J_{t,t-1}^{(i,j)}$ because $P_{\boldsymbol{\theta}}(n_t^{(i)} | \mathbf{h}_t^{(i)})$ is independent of the previous time step. For the likelihood of this function to have no non-global extrema (so that one can quickly estimate the parameters of the model using any gradient ascent technique), it is sufficient that $f(\cdot)$ be both convex and log-concave (a typical example is $f(\cdot) = -\exp(\cdot)$) [99]. Then, this maximization can be solved efficiently using any gradient ascent technique, such as Matlab's `fminunc`. To expedite the computational process, one can also provide the gradient and Hessian for this likelihood function, which are easily calculated here.

B.2 Calcium Parameters

By substituting Eq. 2.2 into Eq. 2.12 and maximizing with respect to $\{\tau, A, [\text{Ca}^{2+}]_b, \sigma_c\}$, we have:

$$\begin{aligned} \{\hat{\tau}, \hat{A}, [\hat{\text{Ca}}^{2+}]_b, \hat{\sigma}_c\} &= \underset{\tau, A, [\text{Ca}^{2+}]_b, \sigma_c}{\operatorname{argmax}} \sum_{t=1}^T \sum_{i,j=1}^N J_{t,t-1}^{(i,j)} \left(\ln P_{\theta}([\text{Ca}^{2+}]_t^{(i)} \mid [\text{Ca}^{2+}]_{t-1}^{(j)}, n_t^{(i)}) \right) \\ &= \underset{\tau, A, [\text{Ca}^{2+}]_b, \sigma_c}{\operatorname{argmax}} \sum_{t=1}^T \sum_{i,j=1}^N J_{t,t-1}^{(i,j)} \left(-\frac{1}{2} \ln(2\pi\sigma_c^2\Delta) - \frac{1}{2} \left(\frac{[\text{Ca}^{2+}]_t^{(i)} - \mu_{t,t-1}^{(i,j)}}{\sigma_c\sqrt{\Delta}} \right)^2 \right), \end{aligned} \quad (\text{B.3})$$

where $\mu_{t,t-1}^{(i,j)} = (1 - \frac{\Delta}{\tau})[\text{Ca}^{2+}]_{t-1}^{(j)} - An_t^{(i)} - \frac{\Delta}{\tau}[\text{Ca}^{2+}]_b$. Thus, we have a standard weighted Gaussian maximum likelihood estimation problem. Thus, solving for $\hat{\tau}$, \hat{A} , and $[\hat{\text{Ca}}^{2+}]_b$ is independent of $\hat{\sigma}_c$:

$$\{\hat{\tau}, \hat{A}, [\hat{\text{Ca}}^{2+}]_b\} = -\frac{1}{2} \underset{\tau, A, [\text{Ca}^{2+}]_b > 0}{\operatorname{argmax}} \sum_{t=1}^T \sum_{i,j=1}^N J_{t,t-1}^{(i,j)} \left([\text{Ca}^{2+}]_t^{(i)} - \mu_{t,t-1}^{(i,j)} \right)^2, \quad (\text{B.4})$$

which is a linearly constrained quadratic programming problem, efficiently solved by Matlab's `quadprog`, for instance. The constraints follow naturally from biophysical properties, e.g., time constants must be positive. To use `quadprog`, we must write this as:

$$\hat{\mathbf{x}} = \underset{\mathbf{x} > 0}{\operatorname{argmin}} \frac{1}{2} \mathbf{x}' \mathbf{Q} \mathbf{x} + \mathbf{L}' \mathbf{x}, \quad (\text{B.5})$$

which requires computing the sufficient statistics, \mathbf{Q} and \mathbf{L} . We therefore make the follow-

APPENDIX B. LEARNING THE PARAMETERS

ing substitutions:

$$\mathbf{C}_t^{(i,j)} = \begin{bmatrix} [\text{Ca}^{2+}]_{t-1}^{(j)} \Delta \\ -n_t^{(i)} \\ -\Delta \end{bmatrix}', \quad \mathbf{x} = \begin{bmatrix} 1/\tau \\ A \\ [\text{Ca}^{2+}]_b/\tau \end{bmatrix}, \quad d_t^{(i,j)} = [\text{Ca}^{2+}]_t^{(i)} - [\text{Ca}^{2+}]_{t-1}^{(j)}, \quad (\text{B.6})$$

which enables one to write Eq. B.4 as a constrained quadratic programming problem:

$$\hat{\mathbf{x}} = \frac{1}{2} \underset{\mathbf{x}_p \geq 0, \forall p}{\text{argmin}} \sum_{t=1}^T \sum_{i,j=1}^N J_{t,t-1}^{(i,j)} \left\| \mathbf{C}_t^{(i,j)} \mathbf{x} + d_t^{(i,j)} \right\|_2^2, \quad (\text{B.7})$$

where the constraint is that all the parameters must be non-negative ($p = 3$ here). We can compute \mathbf{Q} and \mathbf{L} :

$$\mathbf{Q} = \sum_{t=1}^T \sum_{i,j=1}^N J_{t,t-1}^{(i,j)} \mathbf{C}_t^{(i,j)'} \mathbf{C}_t^{(i,j)} \quad (\text{B.8})$$

$$\mathbf{L} = \sum_{t=1}^T \sum_{i,j=1}^N J_{t,t-1}^{(i,j)} \mathbf{C}_t^{(i,j)} d_t^{(i,j)}, \quad (\text{B.9})$$

and plug these quantities into a constrained quadratic program, which yields $\hat{\mathbf{x}}$, from which we obtain the parameters. One can then solve for the variance by plugging in $\hat{\tau}_c$, \hat{A} , and $[\hat{\text{Ca}}^{2+}]_b$ for τ , A , and $[\text{Ca}^{2+}]_b$ in Eq. B.3, evaluating its gradient, and then setting the gradient to zero, yielding:

$$\hat{\sigma}_c^2 = \underset{\sigma_c^2}{\text{argmax}} \sum_{t=1}^T \sum_{i,j=1}^N J_{t,t-1}^{(i,j)} \left(-\frac{1}{2} \ln(2\pi\sigma_c^2\Delta) - \frac{1}{2} \frac{([\text{Ca}^{2+}]_t^{(i)} - \mu_{t,t-1}^{(i,j)})^2}{\sigma_c^2\Delta} \right) \quad (\text{B.10a})$$

$$\Rightarrow \sum_{\substack{t=\{1,\dots,T\} \\ i,j \in \{1,\dots,N\}}} J_{t,t-1}^{(i,j)} \times \left(\frac{1}{\sigma_c} + \frac{([\text{Ca}^{2+}]_t^{(i)} - \mu_{t,t-1}^{(i,j)})^2}{\sigma_c^3\Delta} \right) = 0 \quad (\text{B.10b})$$

$$\hat{\sigma}_c^2 = \frac{1}{T\Delta} \sum_{t=1}^T \sum_{i,j=1}^N J_{t,t-1}^{(i,j)} ([\text{Ca}^{2+}]_t^{(i)} - \mu_{t,t-1}^{(i,j)})^2 = \frac{1}{T\Delta} \left(-\frac{1}{2} \hat{\mathbf{x}} \mathbf{Q} \hat{\mathbf{x}} + \mathbf{L}' \hat{\mathbf{x}} \right), \quad (\text{B.10c})$$

APPENDIX B. LEARNING THE PARAMETERS

where the normalization by T follows from the fact that $\sum_{i,j \in \{1, \dots, N\}} J_{t,t-1}^{(i,j)} = 1$ for all t . Note that it is by virtue of assuming a *nonlinear* relationship between $[\text{Ca}^{2+}]_t$ and F_t that A , σ_c , and $[\text{Ca}^{2+}]_b$ may be estimated exactly, as opposed to only being identifiable up to a scale and offset term. We note here that we could further constrain our parameter estimates by making use of known relationships between the above parameters [4].

B.3 Spike History Parameters

Each spike history term has dynamics similar to the $[\text{Ca}^{2+}]_t$ dynamics. However, the jump size is fixed at 1 for the spike history terms (as its effect is scaled by the spike history weight, ω). Also, we assume the time constants for these spike histories are known and fixed, as they comprise a basis set that spans the space of reasonable spike history effects. The only remaining parameters to estimate are the variances of the noise, which, like the variance for $[\text{Ca}^{2+}]_t$ noise, can be solved for analytically:

$$\hat{\sigma}_{h_l}^2 = \frac{1}{T\Delta} \sum_{t=1}^T \sum_{i,j=1}^N J_{t,t-1}^{(i,j)} \left(h_{l,t}^{(i)} - \left(1 - \frac{\Delta}{\tau_{h_l}}\right) h_{l,t-1}^{(j)} - n_t^{(j)} \right)^2. \quad (\text{B.11})$$

B.4 Observation Parameters

The observation likelihood is given by:

$$\ln P_{\theta}(F_t \mid [\text{Ca}^{2+}]_t) = -\frac{1}{2} \frac{(F_t - \alpha S([\text{Ca}^{2+}]_t) - \beta)^2}{\xi S([\text{Ca}^{2+}]_t) + \sigma_F} - \frac{1}{2} \ln (\xi S([\text{Ca}^{2+}]_t) + \sigma_F) + \kappa, \quad (\text{B.12})$$

APPENDIX B. LEARNING THE PARAMETERS

where κ is a constant independent of the parameters of interest. Maximizing likelihood functions of this form — a Gaussian likelihood whose variance depends on the mean — typically follows an iterative procedure [106]. First, perform a linear regression to estimate α and β , while holding ξ and σ_F fixed:

$$\{\widehat{\alpha}, \widehat{\beta}\} = \operatorname{argmin}_{\alpha, \beta \geq 0} \sum_{t=1}^T \sum_{i=1}^N \frac{(F_t - \alpha S([\text{Ca}^{2+}]_t) - \beta)^2}{\xi S([\text{Ca}^{2+}]_t) + \sigma_F} + \ln (\xi S([\text{Ca}^{2+}]_t) + \sigma_F), \quad (\text{B.13})$$

and then perform another on the residuals to get ξ and σ_F :

$$\{\widehat{\xi}, \widehat{\sigma_F}\} = \operatorname{argmin}_{\xi, \sigma_F \geq 0} (r_t - \xi S([\text{Ca}^{2+}]_t) - \sigma_F)^2, \quad (\text{B.14})$$

where r_t are the residuals from Eq. B.13. Since each of these steps increases the likelihood, iterating these two steps is guaranteed to converge [106].

Chapter 3

pop-oopsi: inferring the *maximum a posteriori* effective connectivity matrix given population observations using a factorization approximation

3.1 Introduction

Since Ramon y Cajal discovered that the brain is a rich and dense network of neurons [1, 107], neuroscientists have been intensely curious about the details of these networks, which are believed to be the biological substrate for memory, cognition, and perception. While we have learned a great deal in the last century about “macro-circuits”

CHAPTER 3. POP-OOPSI

(the connectivity between coarsely-defined brain areas), a number of key questions remain open about “micro-circuit” structure, i.e., the connectivity within populations of neurons at a fine-grained cellular level. Two complementary strategies for investigating micro-circuits have been pursued extensively. *Anatomical* approaches to inferring circuitry do not rely on observing neural activity; some recent exciting examples include array tomography [108], genetic “brainbow” approaches [109], and serial electron microscopy [110]. Our work, on the other hand, takes a *functional* approach: our aim is to infer micro-circuits by observing the simultaneous activity of a population of neurons, without making direct use of fine-grained anatomical measurements.

Experimental tools that enable simultaneous observations of the activity of many neurons are now widely available. While arrays of extracellular electrodes have been exploited for this purpose [111–115], the arrays most often used *in vivo* are inadequate for inferring monosynaptic connectivity in large populations of neurons, as the inter-electrode spacing is typically too large to record from closely neighboring neurons¹; importantly, neighboring neurons are more likely connected to one another than distant neurons [121, 122]. Alternately, calcium-sensitive fluorescent indicators allow us to observe the spiking activity of on the order of 10^3 neighboring neurons [4, 123–125] within a micro-circuit. Some organic dyes achieve sufficiently high signal-to-noise ratios (SNR) that individual action potentials (spikes) may be resolved [4], and bulk-loading techniques enable experimentalists to simultaneously fill populations of neurons with such dyes [45]. In addition, genetically

¹It is worth noting, however, that multielectrode arrays which have been recently developed for use in the retina [116–119] or in cell culture [120] are capable of much denser sampling.

CHAPTER 3. POP-OOPSI

encoded calcium indicators are under rapid development in a number of groups, and are approaching SNR levels of nearly single spike accuracy as well [12]. Microscopy technologies for collecting fluorescence signals are also rapidly developing. Cooled CCDs for wide-field imaging (either epifluorescence or confocal) now achieve a quantum efficiency of $\approx 90\%$ with frame rates up to 60 Hz or greater, depending on the field of view [126]. For *in vivo* work, 2-photon laser scanning microscopy can achieve similar frame rates, using either acoustic-optical deflectors to focus light at arbitrary locations in three-dimensional space [127–129], or resonant scanners [74]. Together, these experimental tools can provide movies of calcium fluorescence transients from large networks of neurons with adequate SNR, at imaging frequencies of 30 Hz or greater, in both *in vitro* and *in vivo* preparations.

Given these experimental advances in functional neural imaging, our goal is to develop efficient computational and statistical methods to exploit this data for the analysis of neural connectivity; see Figure 3.1 for a schematic overview. One major challenge here is that calcium transients due to action potentials provide indirect observations, and decay about an order of magnitude slower than the time course of the underlying neural activity [4, 130]. Thus, to properly analyze the network connectivity, we must incorporate methods for effectively deconvolving the observed noisy fluorescence signal to obtain estimates of the underlying spiking rates [15, 18, 29]. To this end we introduce a coupled Markovian state-space model that relates the observed variables (fluorescence traces from the neurons in the microscope’s field of view) to the hidden variables of interest (the spike trains and intracellular calcium concentrations of these neurons), as governed by a set of biophysical

parameters including the network connectivity matrix. As discussed in [18], this parametric approach effectively introduces a number of constraints on the hidden variables, leading to significantly better performance than standard blind deconvolution approaches. Given this state-space model, we derive a Monte Carlo Expectation Maximization algorithm for obtaining the maximum a posteriori estimates of the parameters of interest. This strategy enables us to accurately infer the connectivity matrix from large simulated neural populations, under realistic assumptions about the dynamics and observation parameters.

3.2 Methods

3.2.1 Model

We begin by detailing a parametric generative model for the (unobserved) joint spike trains of all N observable neurons, along with the observed calcium fluorescence data. Each neuron is modeled as a generalized linear model (GLM). This class of models is known to capture the statistical firing properties of individual neurons fairly accurately [119, 131–142]. We denote the i -th neuron’s activity at time t as $n_i(t)$: in continuous time, $n_i(t)$ could be modeled as an unmarked point process, but we will take a discrete-time approach here, with each $n_i(t)$ taken to be a binary random variable. We model the spiking probability of neuron i via an instantaneous nonlinear function, $f(\cdot)$, of the filtered and summed input to that neuron at that time, $J_i(t)$. This input is composed of: (i) some

CHAPTER 3. POP-OOPSI

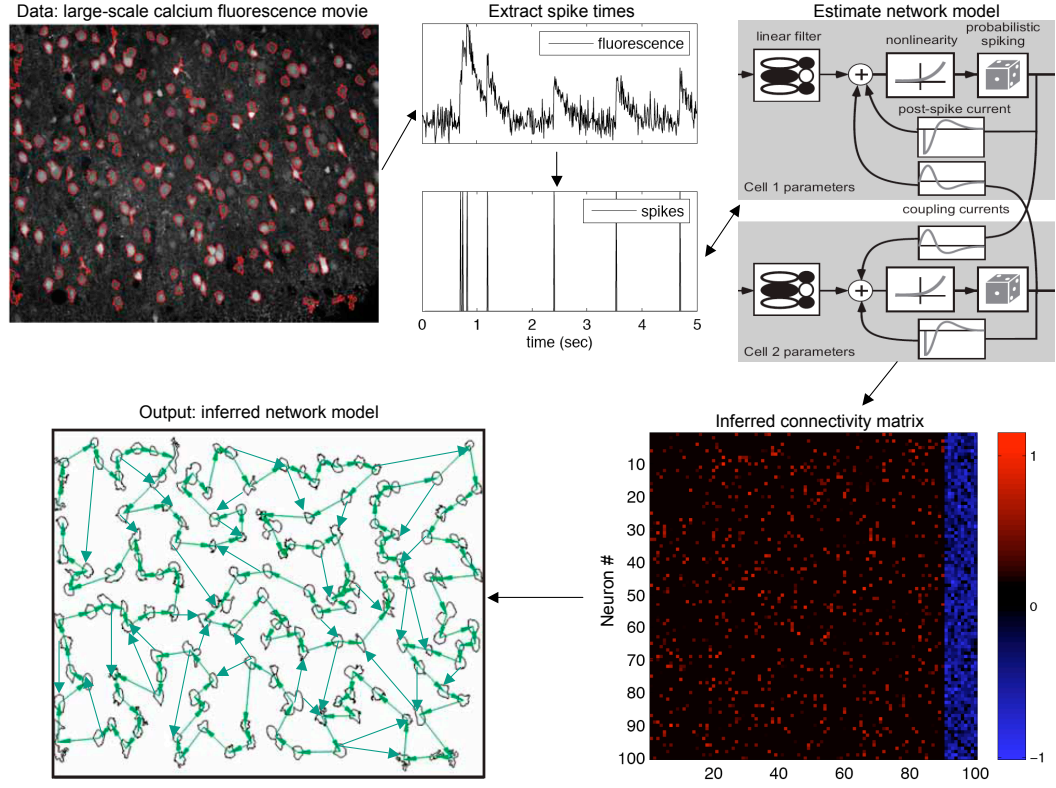


Figure 3.1: Schematic overview. The raw observed data is a large-scale calcium fluorescence movie, which is pre-processed to correct for movement artifacts and find regions-of-interest, i.e., putative neurons. (Note that we have omitted details of these important preprocessing steps in this paper; see, e.g., [103, 124] for further details.) Given the fluorescence traces $F_i(t)$ from each neuron, we estimate the underlying spike trains (i.e., the time series of neural activity) using statistical deconvolution methods. Then we estimate the parameters of a network model given the observed data. Our major goal is to obtain an accurate estimate of the network connectivity matrix, which summarizes the information we are able to infer about the local neuronal microcircuit. (We emphasize that this illustration is strictly schematic, and does not correspond directly to any of the results described below.) This figure adapted from personal communications with R. Yuste, B. Watson, and A. Packer.

baseline value, b_i ; (ii) some external vector stimulus, $S^{ext}(t)$, that is linearly filtered by k_i ; and (iii) spike history terms, $h_{ij}(t)$, encoding the influence on neuron i from neuron j ,

CHAPTER 3. POP-OOPSI

weighted by w_{ij} :

$$n_i(t) \sim \text{Bernoulli} [f(J_i(t))], \quad J_i(t) = b_i + k_i \cdot S^{ext}(t) + \sum_{j=1}^N w_{ij} h_{ij}(t). \quad (3.1)$$

To ensure computational tractability of the parameter inference problem, we must impose some reasonable constraints on the instantaneous nonlinearity $f(\cdot)$ (which plays the role of the inverse of the link function in the standard GLM setting) and on the dynamics of the spike-history effects $h_{ij}(t)$. First, we restrict our attention to functions $f(\cdot)$ which ensure the concavity of the spiking loglikelihood in this model [136, 143], as we will discuss at more length below. In this paper, we use

$$f(J) = P[n > 0 \mid n \sim \text{Pois}(e^J \Delta)] = 1 - \exp[-e^J \Delta] \quad (3.2)$$

(Figure 3.2), where the inclusion of Δ , the time step size, ensures that the firing rate scales properly with respect to the time discretization; see [143] for a proof that this $f(\cdot)$ satisfies the required concavity constraints. However, we should note that in our experience the results depend only weakly on the details of $f(\cdot)$ within the class of log-concave models [136, 144] (see also Section 3.3.4 below).

Second, because the algorithms we develop below assume Markovian dynamics, we model the spike history terms as autoregressive processes driven by the spike train $n_j(t)$:

$$h_{ij}(t) = (1 - \Delta/\tau_{ij}^h) h_{ij}(t - \Delta) + n_j(t - \Delta) + \sigma_{ij}^h \sqrt{\Delta} \epsilon_{ij}^h(t), \quad (3.3)$$

where τ_{ij}^h is a decay time constant, σ_{ij}^h is a standard deviation parameter, $\sqrt{\Delta}$ ensures that the statistics of this Markov process have a proper Ornstein-Uhlenbeck limit as $\Delta \rightarrow 0$,

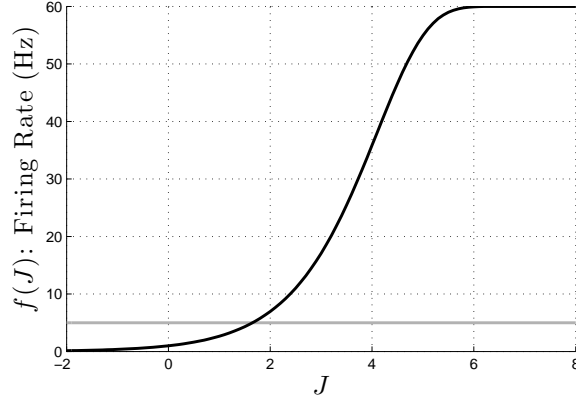


Figure 3.2: A plot of the firing rate nonlinearity $f(J)$ used in our simulations. Note that the firing rate saturates at $1/\Delta$, because of our Bernoulli assumption (i.e., the spike count per bin is at most one). Here the binwidth $\Delta = (60 \text{ Hz})^{-1}$. The horizontal gray line indicates 5 Hz, the baseline firing rate for most of the simulations discussed in the Results section.

and throughout this paper, ϵ denotes an independent standard normal random variable. Note that this model generalizes (via a simple augmentation of the state variable $h_{ij}(t)$) to allow each neuron pair to have several spike history terms, each with a unique time constant, which when weighted and summed allow us to model a wide variety of possible post-synaptic effects, including bursting, facilitating, and depressing synapses; see [18] for further details. We restrict our attention to the case of a single time constant τ_{ij}^h per synapse here, so the deterministic part of $h_{ij}(t)$ is a simple exponentially-filtered version of the spike train $n_j(t)$. Furthermore, we assume that τ_{ij}^h is the same for all neurons and all synapses, although in principle each synapse could be modeled with its unique τ_{ij}^h . We do that both for simplicity and also because we find that the detailed shape of the coupling terms $h_{ij}(t)$ had a limited effect on the inference of the connectivity matrix, as illustrated in Figure 3.12 below. Thus, we treat τ_{ij}^h and σ_{ij}^h as known synaptic parameters which are the same for each neuron pair (i, j) , and denote them as τ_h and σ_h hereafter. We chose

CHAPTER 3. POP-OOPSI

values for τ_h and σ_h in our inference based on experimental data [145]; see Table 1 below.

Therefore our unknown spiking parameters are $\{\mathbf{w}_i, k_i, b_i\}_{i \leq N}$, with $\mathbf{w}_i = (w_{i1}, \dots, w_{iN})$.

The problem of estimating the connectivity parameters $\mathbf{w} = \{\mathbf{w}_i\}_{i \leq N}$ in this type of GLM, given a fully-observed ensemble of neural spike trains $\{n_i(t)\}_{i \leq N}$, has recently received a great deal of attention; see the references above for a partial list. In the calcium fluorescent imaging setting, however, we do not directly observe spike trains; $\{n_i(t)\}_{i \leq N}$ must be considered a hidden variable here. Instead, each spike in a given neuron leads to a rapid increase in the intracellular calcium concentration, which then decays slowly due to various cellular buffering and extrusion mechanisms. We in turn make only noisy, indirect, and subsampled observations of this intracellular calcium concentration, via fluorescent imaging techniques [4]. To perform statistical inference in this setting, [18] proposed a simple conditional first-order hidden Markov model (HMM) for the intracellular calcium concentration $C_i(t)$ in cell i at time t , along with the observed fluorescence, $F_i(t)$:

$$C_i(t) = C_i(t - \Delta) + (C_i^b - C_i(t - \Delta)) \Delta / \tau_i^c + A_i n_i(t) + \sigma_i^c \sqrt{\Delta} \epsilon_i^c(t), \quad (3.4)$$

$$F_i(t) = \alpha_i S(C_i(t)) + \beta_i + \sqrt{(\sigma_i^F)^2 + \gamma_i S(C_i(t))} \epsilon_i^F(t). \quad (3.5)$$

This model can be interpreted as a simple driven autoregressive process: under nonspiking conditions, $C_i(t)$ fluctuates around the baseline level of C_i^b , driven by normally-distributed noise $\epsilon_i^c(t)$ with standard deviation $\sigma_i^c \sqrt{\Delta}$. Whenever the neuron fires a spike, $n_i(t) = 1$, the calcium variable $C_i(t)$ jumps by a fixed amount A_i , and subsequently decays with time constant τ_i^c . The fluorescence signal $F_i(t)$ corresponds to the count of photons collected at the detector per neuron per imaging frame. This photon count may be modeled with normal

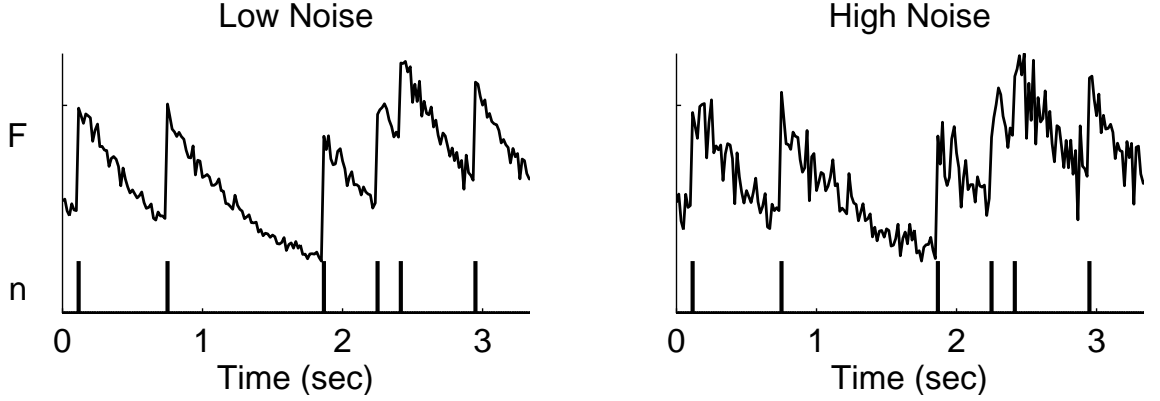


Figure 3.3: Two example traces of simulated fluorescence data, at different SNR levels, demonstrating the relationship between spike trains and observed fluorescence in our model. Note that both panels have the same underlying spike train. Simulation parameters: $k_i = 0.7$, $C_i^b = 1 \mu\text{M}$, $\tau_i^c = 500 \text{ msec}$, $A_i = 50 \mu\text{M}$, $\sigma_i^c = 0.1 \mu\text{M}$. $\gamma_i = 0.004$ (effective SNR ≈ 9 , as defined in Eq. (3.6); see also Figure 3.9 below) in the left panel and $\gamma_i = 0.016$ (eSNR ≈ 3) in the right panel, and $\sigma_i^F = 0$, $\Delta = (60 \text{ Hz})^{-1}$.

statistics, with the mean given by a saturating Hill-type function $S(C) = C/(C + K_d)$ [146] and the variance scaling with the mean; see [18] for further discussion. Because the parameter K_d effectively acts as a simple scale factor, and is a property of the fluorescent indicator, we assume throughout this work that it is known. Figure 3.3 shows a couple examples depicting the relationship between spike trains and observations. It will be useful to define an effective SNR as

$$\text{eSNR} = \frac{E[F_i(t) - F_i(t - \Delta) \mid n_i(t) = 1]}{E[(F_i(t) - F_i(t - \Delta))^2 / 2 \mid n_i(t) = 0]^{1/2}}, \quad (3.6)$$

i.e., the size of a spike-driven fluorescence jump divided by a rough measure of the standard deviation of the baseline fluorescence. For concreteness, the effective SNR values in Fig. 3.3 were 9 and 3 in the left and right panels, respectively.

To summarize, Eqs. (3.1-3.5) define a coupled HMM: the underlying spike trains

$\{n_i(t)\}_{i \leq N}$ and spike history terms $\{h_{ij}(t)\}_{i,j \leq N}$ evolve in a Markovian manner given the stimulus $S^{ext}(t)$. These spike trains in turn drive the intracellular calcium concentrations $\{C_i(t)\}_{i \leq N}$, which are themselves Markovian, but evolving at a slower timescale τ_i^c . Finally, we observe only the fluorescence signals $\{F_i(t)\}_{i \leq N}$, which are related in a simple Markovian fashion to the calcium variables $\{C_i(t)\}_{i \leq N}$.

3.2.2 Goal and general strategy

Our primary goal is to estimate the connectivity matrix, \mathbf{w} , given the observed set of calcium fluorescence signals $\mathbf{F} = \{\mathbf{F}_i\}_{i \leq N}$, where $\mathbf{F}_i = \{F_i(t)\}_{t \leq T}$. We must also deal with a number of intrinsic parameters², $\tilde{\boldsymbol{\theta}}_i$: the intrinsic spiking parameters³ $\{b_i, w_{ii}\}_{i \leq N}$, the calcium parameters $\{C_i^b, \tau_i^c, A_i, \sigma_i^c\}_{i \leq N}$, and the observation parameters $\{\alpha_i, \beta_i, \gamma_i, \sigma_i^F\}_{i \leq N}$. We addressed the problem of estimating these intrinsic parameters in earlier work [18]; thus our focus here will be on the connectivity matrix \mathbf{w} . A Bayesian approach is natural here, since we have a good deal of prior information about neural connectivity; see [137] for a related discussion. However, a fully-Bayesian approach, in which we numerically integrate over the very high-dimensional parameter space $\boldsymbol{\theta} = \{\boldsymbol{\theta}_i\}_{i \leq N}$, where $\boldsymbol{\theta}_i = \{\mathbf{w}_i, b_i, C_i^b, \tau_i^c, A_i, \sigma_i^c, \alpha_i, \beta_i, \gamma_i, \sigma_i^F\}$, is less attractive from a computational point of view. Thus, our compromise is to compute *maximum a posteriori* (MAP) estimates for the parameters via an expectation-maximization (EM) algorithm, in which the sufficient

²The intrinsic parameters for neuron i are all its parameters, minus the cross-coupling terms, i.e. $\tilde{\boldsymbol{\theta}}_i = \boldsymbol{\theta}_i \setminus \{w_{ij}\}_{i \neq j}$.

³To reduce the notational load, we will ignore the estimation of the stimulus filter k_i below; this term may be estimated with b_i and w_{ii} using very similar convex optimization methods, as discussed in [18].

CHAPTER 3. POP-OOPSI

statistics are computed by a sequential Monte Carlo (SMC) method. More specifically, we iterate the steps:

E step: Evaluate $Q(\boldsymbol{\theta}, \boldsymbol{\theta}^{(l)}) = E_{P[\mathbf{X}|\mathbf{F}; \boldsymbol{\theta}^{(l)}]} \ln P[\mathbf{F}, \mathbf{X}|\boldsymbol{\theta}] = \int P[\mathbf{X}|\mathbf{F}; \boldsymbol{\theta}^{(l)}] \ln P[\mathbf{F}, \mathbf{X}|\boldsymbol{\theta}] d\mathbf{X}$

M step: Solve $\boldsymbol{\theta}^{(l+1)} = \underset{\boldsymbol{\theta}}{\operatorname{argmax}} \left\{ Q(\boldsymbol{\theta}, \boldsymbol{\theta}^{(l)}) + \ln P(\boldsymbol{\theta}) \right\},$

where \mathbf{X} denotes the set of all hidden variables $\{C_i(t), n_i(t), h_{ij}(t)\}_{i,j \leq N, t \leq T}$ and $P(\boldsymbol{\theta})$ denotes a (possibly improper) prior on the parameter space $\boldsymbol{\theta}$. According to standard EM theory [147, 148], each iteration of these two steps is guaranteed to increase the log-posterior $\ln P(\boldsymbol{\theta}^{(l)}|\mathbf{F})$, and will therefore lead to at least a locally maximum a posteriori estimator.

Now, our major challenge is to evaluate the auxiliary function $Q(\boldsymbol{\theta}, \boldsymbol{\theta}^{(l)})$ in the E-step. Our model is a coupled HMM, as discussed in the previous section; therefore, as usual in the HMM setting [149], Q may be broken up into a sum of simpler terms:

$$\begin{aligned} Q(\boldsymbol{\theta}, \boldsymbol{\theta}^{(l)}) &= \sum_{it} \int \ln P[F_i(t)|C_i(t); \alpha_i, \beta_i, \gamma_i, \sigma_i^F] dP[C_i(t)|\mathbf{F}; \boldsymbol{\theta}^{(l)}] \\ &+ \sum_{it} \int \ln P[C_i(t)|C_i(t-\Delta), n_i(t); C_i^b, \tau_i^c, A_i, \sigma_i^c] dP[C_i(t), C_i(t-\Delta)|\mathbf{F}; \boldsymbol{\theta}^{(l)}] \\ &+ \sum_{it} \int \ln P[n_i(t)|\mathbf{h}_i(t); b_i, \mathbf{w}_i] dP[n_i(t), \mathbf{h}_i(t)|\mathbf{F}; \boldsymbol{\theta}^{(l)}], \end{aligned} \quad (3.7)$$

where $\mathbf{h}_i(t) = \{h_{ij}(t)\}_{j \leq N}$. Note that each of the three sums here corresponds to a different component of the model described in Eqs. (3.1-3.5): the first sum involves the fluorescent observation parameters, the second the calcium dynamics, and the third the spiking dynamics.

Thus we need only compute low-dimensional marginals of the full posterior distribution $P[\mathbf{X}|\mathbf{F}; \boldsymbol{\theta}]$; specifically, we need the pairwise marginals $P[C_i(t)|\mathbf{F}; \boldsymbol{\theta}]$, $P[C_i(t), C_i(t -$

$\Delta)|\mathbf{F}; \boldsymbol{\theta}]$, and $P[n_i(t), \mathbf{h}_i(t)|\mathbf{F}; \boldsymbol{\theta}]$. Details for calculating $P[C_i(t), C_i(t - \Delta)|\mathbf{F}_i; \tilde{\boldsymbol{\theta}}_i]$ and $P[C_i(t)|\mathbf{F}_i; \tilde{\boldsymbol{\theta}}_i]$ are found in [18], while calculating the joint marginal for the high dimensional hidden variable \mathbf{h}_i necessitates the development of approximations as described in Section 3.2.3. Once we have obtained these (approximate) marginals, the M-step breaks up into a number of independent optimizations that may be computed in parallel and which are therefore relatively straightforward (Section 3.2.5); see Section 3.2.6 for a pseudocode summary along with some specific implementation details.

3.2.3 Initialization of intrinsic parameters via sequential Monte Carlo methods

We begin by constructing relatively cheap, approximate preliminary estimators for the intrinsic parameters, $\tilde{\boldsymbol{\theta}}_i$. The idea is to initialize our estimator by assuming that each neuron is observed independently. Thus we want to compute $P[C_i(t), C_i(t - \Delta)|\mathbf{F}_i; \tilde{\boldsymbol{\theta}}_i]$ and $P[C_i(t)|\mathbf{F}_i; \tilde{\boldsymbol{\theta}}_i]$, and solve the M-step for each $\tilde{\boldsymbol{\theta}}_i$, with the connectivity matrix parameters held fixed. This single-neuron case is much simpler, and has been discussed at length in [18]; therefore, we only provide a brief overview here. The standard forward and backward recursions provide the necessary posterior distributions, in principle [106]:

$$P[X_i(t)|F_i(0:t)] \propto \int P[F_i(t)|X_i(t)] P[X_i(t)|X_i(t-\Delta)] P[X_i(t-\Delta)|F_i(0:t-\Delta)] dX_i(t-\Delta), \quad (3.8)$$

CHAPTER 3. POP-OOPSI

$$P[X_i(t), X_i(t - \Delta) | \mathbf{F}_i] = P[X_i(t) | \mathbf{F}_i] \frac{P[X_i(t) | X_i(t - \Delta)] P[X_i(t - \Delta) | F_i(0 : t - \Delta)]}{\int P[X_i(t) | X_i(t - \Delta)] P[X_i(t - \Delta) | F_i(0 : t - \Delta)] dX_i(t - \Delta)}, \quad (3.9)$$

where $F_i(s : t)$ denotes the time series \mathbf{F}_i from time points s to t , and we have dropped the conditioning on the parameters for brevity's sake. Eq. (3.8) describes the forward (filter) pass of the recursion, and Eq. (3.9) describes the backward (smoother) pass, providing both $P[X_i(t), X_i(t - \Delta) | \mathbf{F}_i]$ and $P[X_i(t) | \mathbf{F}_i]$ (obtained by marginalizing over $X_i(t - \Delta)$).

Because these integrals cannot be analytically evaluated for our model, we approximate them using a SMC (“marginal particle filtering”) method [150–152]. More specifically, we replace the forward distribution with a particle approximation:

$$P[X_i(t) | F_i(0 : t)] \approx \sum_{m=1}^M p_f^{(m)}(t) \delta[X_i(t) - X_i^{(m)}(t)], \quad (3.10)$$

where $m = 1, \dots, M$ indexes the M particles in the set (M was typically set to about 50 in our experiments), $p_f^{(m)}(t)$ corresponds to the relative “forward” probability of $X_i(t) = X_i^{(m)}(t)$, and $\delta[\cdot]$ indicates a Dirac mass. Instead of using the analytic forward recursion, Eq. (3.8), at each time step, we update the particle weights using the particle forward recursion

$$p_f^{(m)}(t) = P[F_i(t) | X_i^{(m)}(t)] \frac{P[X_i^{(m)}(t) | X_i^{(m)}(t - \Delta)] p_f^{(m)}(t - \Delta)}{q[X_i^{(m)}(t)]}, \quad (3.11)$$

where $q[X_i^{(m)}(t)]$ is the proposal density from which we sample the particle positions $X_i^{(m)}(t)$. In this work, we use the “one-step-ahead” sampler [18, 150], i.e., $q[X_i^{(m)}(t)] = P[X_i^{(m)}(t) | X_i^{(m)}(t - \Delta), F_i(t)]$. After sampling and computing the weights, we use strat-

CHAPTER 3. POP-OOPSI

ified resampling [153] to ensure the particles accurately approximate the desired distribution. Once we complete the forward recursion from $t = 0, \dots, T$, we begin the backwards pass from $t = T, \dots, 0$, using

$$r^{(m,m')}(t, t - \Delta) = p_b^{(m)}(t) \frac{P[X_i^{(m)}(t)|X_i^{(m')}(t - \Delta)]p_f^{(m)}(t - \Delta)}{\sum_{m'} P[X_i^{(m)}(t)|X_i^{(m')}(t - \Delta)]p_f^{(m')}(t - \Delta)} \quad (3.12)$$

$$p_b^{(m')}(t - \Delta) = \sum_{j=1}^M r^{(m,m')}(t, t - \Delta), \quad (3.13)$$

to obtain the approximation

$$P[X_i(t), X_i(t - \Delta)|F_i] \approx \sum_{m,m'} r_i^{(m,m')}(t, t - \Delta) \delta[X_i(t) - X_i^{(m)}(t)] \delta[X_i(t - \Delta) - X_i^{(m')}(t - \Delta)]; \quad (3.14)$$

for more details, see [18]. Thus equations (3.10-3.14) may be used to compute the sufficient statistics for estimating the intrinsic parameters $\tilde{\theta}_i$ for each neuron.

As discussed following Eq. (3.7), the M-step decouples into three independent sub-problems. The first term depends on only $\{\alpha_i, \beta_i, \gamma_i, \sigma_i\}$; since $P[F_i(t)|S(C_i(t)); \tilde{\theta}_i]$ is Gaussian, we can estimate these parameters by solving a weighted regression problem (specifically, we use a coordinate-optimization approach: we solve a quadratic problem for $\{\alpha_i, \beta_i\}$ while holding $\{\gamma_i, \sigma_i\}$ fixed, then estimate $\{\gamma_i, \sigma_i\}$ by the usual residual error formulas while holding $\{\alpha_i, \beta_i\}$ fixed). Similarly, the second term requires us to optimize over $\{\tau_i^c, A_i, C_i^b\}$, and then we use the residuals to estimate σ_i^c . Note that all the parameters mentioned so far are constrained to be non-negative, but may be solved efficiently using standard quadratic program solvers if we use the simple reparameterization $\tau_i^c \rightarrow 1 - \Delta/\tau_i^c$.

Finally, the last term may be expanded:

$$\begin{aligned} & E[\ln P[n_i(t), \mathbf{h}_i(t) | \mathbf{F}; \boldsymbol{\theta}_i]] \\ &= P[n_i(t), \mathbf{h}_i(t) | \mathbf{F}; \boldsymbol{\theta}_i] \ln f[J_i(t)] + (1 - P[n_i(t), \mathbf{h}_i(t) | \mathbf{F}; \boldsymbol{\theta}_i]) \ln[1 - f(J_i(t))]; \quad (3.15) \end{aligned}$$

since $J_i(t)$ is a linear function of $\{b_i, \mathbf{w}_i\}$, and the right-hand side of Eq. (3.15) is concave in $J_i(t)$, we see that the third term in Eq. (3.7) is a sum of terms which are concave in $\{b_i, \mathbf{w}_i\}$ — and therefore also concave in the linear subspace $\{b_i, w_{ii}\}$ with $\{w_{ij}\}_{i \neq j}$ held fixed — and may thus be maximized efficiently using any convex optimization method, e.g. Newton-Raphson or conjugate gradient ascent.

Our procedure therefore is to initialize the parameters for each neuron using some default values that we have found to be effective in practice in analyzing real data, and then iteratively (i) estimate the marginal posteriors via the SMC recursions (3.10-3.14) (E step), and (ii) maximize over the intrinsic parameters $\tilde{\boldsymbol{\theta}}_i$ (M step), using the separable convex optimization approach described above. We iterate these two steps until the change in $\tilde{\boldsymbol{\theta}}_i$ does not exceed some minimum threshold. We then use the marginal posteriors from the last iteration to seed the factorized method described below for approximating $P[n_i, \mathbf{h}_i | \mathbf{F}; \boldsymbol{\theta}_i]$.

3.2.4 A factorized approximation of the joint posteriors

If the SNR in the calcium imaging is sufficiently high, then by definition the observed fluorescence data F_i will provide enough information to determine the underlying hidden variables \mathbf{X}_i . Thus, in this case the joint posterior approximately factorizes into a product

CHAPTER 3. POP-OOPSI

of marginals for each neuron i :

$$P[\mathbf{X}|\mathbf{F}; \boldsymbol{\theta}] \approx \prod_{i \leq N} P[X_i|\mathbf{F}; \tilde{\boldsymbol{\theta}}_i]. \quad (3.16)$$

We can take advantage of this because we have already estimated all the marginals on the right hand side using the approximate SMC methods in Section 3.2.3. This factorized approximation entails a significant gain in efficiency because we can easily parallelize the SMC step, inferring the marginals $P[X_i(t)|F_i; \tilde{\boldsymbol{\theta}}_i]$ and estimating the parameters $\boldsymbol{\theta}_i$ for each neuron on a separate processor. We will discuss the empirical accuracy of this approximation in the Results section.

3.2.5 Estimating the connectivity matrix

Computing the M-step for the connectivity matrix, \mathbf{w} , is an optimization problem with on the order of N^2 variables. The auxiliary function Eq. (3.7) is concave in \mathbf{w} , and decomposes into N separable terms that may be optimized independently using standard ascent methods. To improve our estimates, we will incorporate two sources of strong *a priori* information via our prior $P(\mathbf{w})$: first, previous anatomical studies have established that connectivity in many neuroanatomical substrates is “sparse,” i.e., most neurons form synapses with only a fraction of their neighbors [154–163], implying that many elements of the connectivity matrix \mathbf{w} are zero; see also [119, 136, 137, 164] for further discussion. Second, “Dale’s law” states that each of a neuron’s postsynaptic connections in adult cortex (and many other brain areas) must all be of the same sign (either excitatory or inhibitory). Both

of these priors are easy to incorporate in the M-step optimization, as we discuss below.

3.2.5.1 Imposing a sparse prior on the connectivity

It is well-known that imposing sparseness via an $L1$ -regularizer can dramatically reduce the amount of data necessary to accurately reconstruct sparse high-dimensional parameters [165–170]. We incorporate a prior of the form $\ln p(\mathbf{w}) = \text{const.} - \lambda \sum_{i,j} |w_{ij}|$, and additionally enforce the constraints $|w_{ij}| < L$, for a suitable constant L (since both excitatory and inhibitory cortical connections are known to be bounded in size). Since the penalty $\ln p(\mathbf{w})$ is concave, and the constraints $|w_{ij}| < L$ are convex, we may solve the resulting optimization problem in the M-step using standard convex optimization methods [27]. In addition, the problem retains its separable structure: the full optimization may be broken up into N smaller problems that may be solved independently.

3.2.5.2 Imposing Dale’s law on the connectivity

Enforcing Dale’s law requires us to solve a non-convex, non-separable problem: we need to optimize the concave function $Q(\boldsymbol{\theta}, \boldsymbol{\theta}^{(l)}) + \ln P(\boldsymbol{\theta})$ under the non-convex, non-separable constraint that all of the elements in any column of the matrix \mathbf{w} are of the same sign (either nonpositive or nonnegative). It is difficult to solve this nonconvex problem exactly, but we have found that simple greedy methods are quite efficient in finding good approximate solutions.

We begin with our original sparse solution, obtained as discussed in the previous sub-

CHAPTER 3. POP-OOPSI

section without enforcing Dale’s law. Then we assign each neuron as either excitatory or inhibitory, based on the weights we have inferred in the previous step: i.e., neurons i whose inferred postsynaptic connections w_{ij} are largely positive are tentatively labeled excitatory, and neurons with largely inhibitory inferred postsynaptic connections are labeled inhibitory. Neurons which are ambiguous may be unassigned in the early iterations, to avoid making mistakes from which it might be difficult to recover. Given the assignments a_i ($a_i = 1$ for putative excitatory cells, -1 for inhibitory, and 0 for neurons which have not yet been assigned) we solve the convex, separable problem

$$\operatorname{argmax}_{a_i w_{ij} \geq 0, |w_{ij}| < L \ \forall i,j} Q(\boldsymbol{\theta}, \boldsymbol{\theta}^{(l)}) - \lambda \sum_{ij} |w_{ij}| \quad (3.17)$$

which may be handled using the standard convex methods discussed above. Given the new estimated connectivities \boldsymbol{w} , we can re-assign the labels a_i , or flip some randomly to check for local optima. We have found this simple approach to be effective in practice.

3.2.6 Specific implementation notes

Pseudocode summarizing our approach is given in Algorithm 2. As discussed in Section 3.2.3, the intrinsic parameters $\tilde{\boldsymbol{\theta}}_i$ may be initialized effectively using the methods described in [18]; then the full parameter $\boldsymbol{\theta}$ is estimated via EM, where we use the factorized approximation described in Section 3.2.4 to obtain the sufficient statistics in the E step and the separable convex optimization methods discussed in Section 3.2.5 for the M step.

As emphasized above, the parallel nature of these EM steps is essential for making these

Algorithm 2 Pseudocode for estimating connectivity from calcium imaging data using EM;

η_1 and η_2 are user-defined convergence tolerance parameters.

```

while  $|\mathbf{w}^{(l)} - \mathbf{w}^{(l-1)}| > \eta_1$  do

    for all  $i = 1 \dots N$  do

        while  $|\tilde{\theta}_i^{(l)} - \tilde{\theta}_i^{(l-1)}| > \eta_2$  do

            Approximate  $P[X_i(t)|F_i; \tilde{\theta}_i]$  using SMC (Section 3.2.3)

            Perform the M-step for the intrinsic parameters  $\tilde{\theta}_i$  (Section 3.2.3)

        end while

    end for

    for all  $i = 1 \dots N$  do

        Approximate  $P[n_i(t), \mathbf{h}_i(t)|\mathbf{F}; \theta_i]$  using

        the factorized approximation (Section 3.2.4)

    end for

    for all  $i = 1 \dots N$  do

        Perform the M-step for  $\{b_i, \mathbf{w}_i\}_{i \leq N}$  using separable convex optimization methods

        (Section 3.2.5)

    end for

end while

```

computations tractable. We performed the bulk of our analysis on a 256-processor cluster of Intel Xeon L5430 based computers (2.66 GHz). For 10 minutes of simulated fluorescence data, imaged at 30 Hz, calculations using the factorized approximation typically took 10-20

minutes per neuron (divided by the number of available processing nodes on the cluster), with time split approximately equally between (i) estimating the intrinsic parameters $\tilde{\theta}_i$, (ii) approximating the posteriors using the independent SMC method, and (iii) estimating the connectivity matrix, w .

3.2.7 Simulating a neural population

To test the described method for inferring connectivity from calcium imaging data, we simulated networks of spontaneously firing randomly connected neurons according to our model, Eqs. (3.1-3.5), and also using other network models (see Section 3.3.4). Although simulations ran at 1 msec time discretization, the imaging rate was assumed to be much slower: 5–200 Hz (c.f. Fig. 3.8 below).

Model parameters were chosen based on experimental data available in the literature for cortical neural networks [122, 145, 171, 172]. More specifically, the network consisted of 80% excitatory and 20% inhibitory neurons [122, 172], each respecting Dale’s law (as discussed in Section 3.2.5 above). Neurons were randomly connected to each other in a spatially homogeneous manner with probability 0.1 [122, 145]. Synaptic weights for excitatory connections, as defined by excitatory postsynaptic potential (PSP) peak amplitude, were randomly drawn from an exponential distribution with the mean of 0.5 mV [145, 171]. Inhibitory connections were also drawn from an exponential distribution; their strengths chosen so as to balance excitatory and inhibitory currents in the network, and achieve an average firing rate of ≈ 5 Hz [121]. Practically, this meant that the mean strength of

CHAPTER 3. POP-OOPSI

inhibitory connections was about 10 times larger than that of the excitatory connections. PSP shapes were modeled as an alpha function [173]: roughly, the difference of two exponentials, corresponding to a sharp rise and relatively slow decay [171]. We neglected conduction delays, given that the time delays below ~ 1 msec expected in the local cortical circuit were far below the time resolution of our simulated imaging data.

Note that PSP peak amplitudes measured *in vitro* (as in, e.g., [162]) cannot be incorporated directly in Eq. (3.1), since the synaptic weights in our model — w_{ij} in Eq. (3.1) — are dimensionless quantities representing the change in the spiking probability of neuron i given a spike in neuron j , whereas PSP peak amplitude describes the physiologically measured change in the membrane voltage of a neuron due to synaptic currents triggered by a spike in neuron j . To relate the two, note that in order to trigger an immediate spike in a neuron that typically has its membrane voltage V_b mV below the spiking threshold, roughly $n_E = V_b/V_E$ simultaneous excitatory PSPs with the peak amplitude V_E would be necessary. Therefore, the change in the spiking probability of a neuron due to excitatory synaptic current V_E can be approximately defined as

$$\delta P_E = V_E/V_b \quad (3.18)$$

(so that $\delta P_E n_E \approx 1$). $V_b \approx 15$ mV here, while values for the PSP amplitude V_E were chosen as described above. Similarly, according to Eq. 3.1, the same change in the spiking probability of a neuron i following the spike of a neuron j in the GLM is roughly

$$\delta P_E = [f(b_i + w_{ij}) - f(b_i)] \tau_h, \quad (3.19)$$

CHAPTER 3. POP-OOPSI

where recall τ_h is the typical PSP time-scale, i.e. the time over which a spike in neuron j significantly affects the firing probability of the neuron i . Equating these two expressions gives us a simple method for converting the physiological parameters V_E and V_b into suitable GLM parameters w_{ij} .

Finally, parameters for the internal calcium dynamics and fluorescence observations were chosen according to our experience with several cells analyzed using the algorithm of [18], and conformed to previously published results [4, 62, 63]. Table 3.1 summarizes the details for each of the parameters in our model.

3.3 Results

In this section we study the performance of our proposed network estimation methods, using the simulated data described in section 3.2.7 above. Specifically, we estimated the connectivity matrix using the factorized approximation. Figure 3.4 summarizes one typical experiment: the EM algorithm using the factorized approximation estimated the connectivity matrix about as accurately as the full embedded-chain-within-blockwise-Gibbs approach ($r^2 = 0.47$ versus $r^2 = 0.48$) (see [39] for details on the embedded-chain-within-blockwise-Gibbs details).

CHAPTER 3. POP-OOPSI

Table 3.1: Table of simulation parameters. $\mathcal{E}(\lambda)$ indicates an exponential distribution with mean λ , and $\mathcal{N}_p(\mu, \sigma^2)$ indicates a normal distribution with mean μ and variance σ^2 , truncated at lower bound $p\mu$. Units (when applicable) are given with respect to mean values (i.e., units are squared for variance).

Variable	Value/Distribution	Unit
Total neurons	10-500	#
Excitatory neurons	80	%
Connections sparseness	10	%
Baseline firing rate	5	Hz
Excitatory PSP peak height	$\sim \mathcal{E}(0.5)$	mV
Inhibitory PSP peak height	$\sim -\mathcal{E}(2.3)$	mV
Excitatory PSP rise time	1	msec
Inhibitory PSP rise time	1	msec
Excitatory PSP decay time	$\sim \mathcal{N}_{0.5}(10, 2.5)$	msec
Inhibitory PSP decay time	$\sim \mathcal{N}_{0.5}(20, 5)$	msec
Refractory time, w_{ii}	$\sim \mathcal{N}_{0.5}(10, 2.5)$	msec
Calcium std. σ_c	$\sim \mathcal{N}_{0.4}(28, 10)$	μM
Calcium jump after spike, A_c	$\sim \mathcal{N}_{0.4}(80, 20)$	μM
Calcium baseline, C_b	$\sim \mathcal{N}_{0.4}(24, 8)$	μM
Calcium decay time, τ_c	$\sim \mathcal{N}_{0.4}(200, 60)$	msec
Dissociation constant, K_d	200	μM
Fluorescence scale, α	1	n/a
Fluorescence baseline, β	0	n/a
Signal-dependent noise, γ	10^{-3} - 10^{-5} 130	n/a
Signal-independent noise, σ^F	$4 \cdot 10^{-3}$ - $4 \cdot 10^{-5}$	n/a

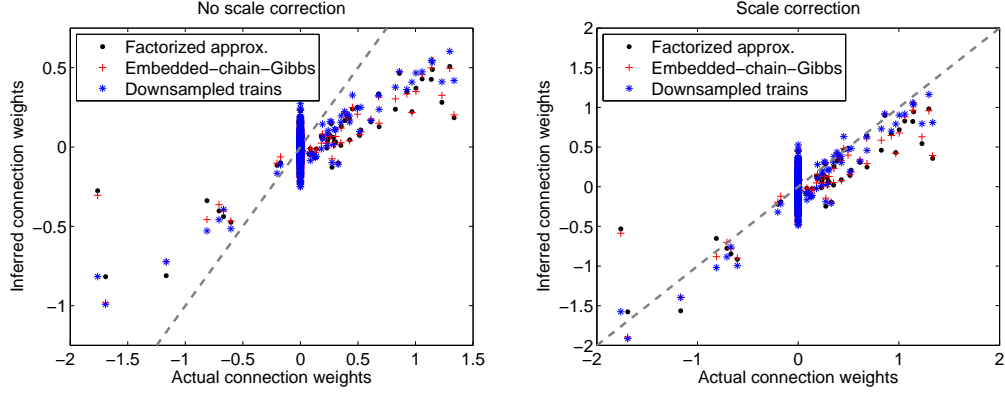


Figure 3.4: Quality of the connectivity matrix estimated from simulated calcium imaging data. Inferred connection weights \hat{w}_{ij} are shown in a scatter plot versus real connection weights w_{ij} , with inference performed using the factorized approximation, exact embedded-chain-within-blockwise-Gibbs approach [39], and true spike trains downsampled to the frame rate of the calcium imaging. A network of $N = 25$ neurons was used, firing at ≈ 5 Hz, and imaged for $T = 10$ min at 60 Hz with intermediate eSNR ≈ 6 (see Eq. (3.6) and Figure 3.9 below). The squared correlation coefficient between the connection weights calculated using the factorized approximation and true connection weights was $r^2 = 0.47$, compared with the embedded-chain-within-blockwise-Gibbs method's $r^2 = 0.48$. For connection weights calculated directly from the true spike train down-sampled to the calcium imaging frame rate we obtained $r^2 = 0.57$. (For comparison, $r^2 = 0.71$ for the connectivity matrix calculated using the full spike trains with 1 ms precision; data not shown.) Here and in the following figures the gray dashed line indicates unity, $y = x$. The inferred connectivity in the left panel shows a clear scale bias, which can be corrected by dividing by the scale correction factor calculated in Section 3.3.1 below (right panel). The vertical lines apparent at zero in both subplots are due to the fact that the connection probability in the true network was significantly less than one: i.e., many of the true weights w_{ij} are exactly zero.

3.3.1 Impact of coarse time discretization of calcium imaging data and scale factor of inferred connection weights

A notable feature of the results illustrated in the left panel of Fig. 3.4 is that our estimator is biased downwards by a roughly constant scale factor: our estimates \hat{w}_{ij} are

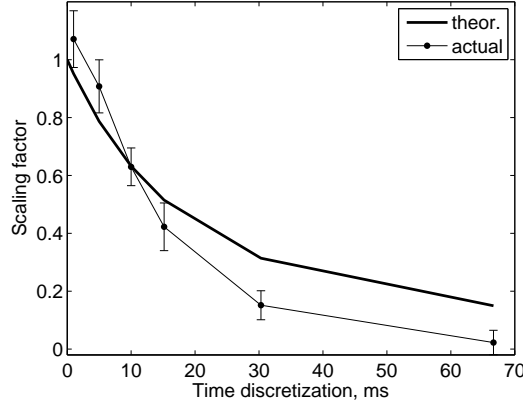


Figure 3.5: The low frame rate of calcium imaging explains the scale error observed in the inferred connectivity weights shown in Figure 3.4. A correction scale factor may be calculated analytically (thick line) as discussed in the main text (Eq. 3.23). The scale error observed empirically (thin line) matches well with this theoretical estimate. In the latter case, the scale error was calculated from the fits obtained directly from the true spike trains, down sampled to different Δ , for a network of $N = 25$ neurons firing at ≈ 5 Hz and observed for $T = 10$ min. The error-bars indicate 95% confidence intervals for scale error at each Δ .

approximately linearly related to the true values of w_{ij} in the simulated network, but the slope of this linear relationship is less than one. At first blush, this bias does not seem like a major problem: as we discussed in Section 3.2.7, even in the noiseless case we should at best expect our estimated coupling weights \hat{w}_{ij} to correspond to some monotonically increasing function of the true neural connectivities, as measured by biophysical quantities such as the peak PSP amplitude. Nonetheless, we would like to understand the source of this bias more quantitatively; in this section, we discuss this issue in more depth and derive a simple method for correcting the bias.

The bias is largely due to the fact that we suffer a loss of temporal resolution when we attempt to infer spike times from slowly-sampled fluorescence data. As discussed in [18],

CHAPTER 3. POP-OOPSI

we can recover some of this temporal information by using a finer time resolution for our recovered spike trains than Δ , the time resolution of the observed fluorescence signal. However, when we attempted to infer \mathbf{w} directly spike trains sampled from the posterior $P[\mathbf{X}|\mathbf{F}]$ at higher-than- Δ resolution, we found that the inferred connectivity matrix was strongly biased towards the symmetrized matrix $(\mathbf{w} + \mathbf{w}^T)/2$ (data not shown). In other words, whenever a nearly synchronous jump was consistently observed in two fluorescent traces $F_i(t)$ and $F_j(t)$ (at the reduced time resolution Δ), the EM algorithm would typically infer an excitatory *bidirectional* connection: i.e., both \hat{w}_{ij} and \hat{w}_{ji} would be large, even if only a unidirectional connection existed between neurons i and j in the true network. While we expect, by standard arguments, that the Monte Carlo EM estimator constructed here should be consistent (i.e., we should recover the correct \mathbf{w} in the limit of large data length T and many Monte Carlo samples), we found that this bias persisted given experimentally-reasonable lengths of data and computation time.

Therefore, to circumvent this problem, we simply used the original imaging time resolution Δ for the inferred spike trains: note that, due to the definition of the spike history terms h_{ij} in Eq. (3.3), a spike in neuron j at time t will only affect neuron i 's firing rate at time $t + \Delta$ and greater. This successfully counteracted the symmetrization problem (and also sped the calculations substantially), but resulted in the scale bias exhibited in Figure 3.4, since any spikes that fall into the same time bin are treated as coincidental: only spikes that precede spikes in a neighboring neuron by at least one time step will directly affect the estimates of w_{ij} , and therefore grouping asynchronous spikes within a single time bin Δ

CHAPTER 3. POP-OOPSI

results in a loss of information.

To estimate the magnitude of this time-discretization bias more quantitatively, we consider a significantly simplified case of two neurons coupled with a small weight w_{12} , and firing with baseline firing rate of $r = f(b)$. In this case an approximate sufficient statistic for estimating w_{12} may be defined as the expected elevation in the spike rate of neuron one on an interval of length \mathcal{T} , following a spike in neuron two:

$$\begin{aligned} SS &= E \left[\int_{t'}^{t'+\mathcal{T}} n_1(t) dt \mid n_2(t') = 1, n_2(t) = 0 \forall t \in (t', t' + \mathcal{T}] \right] \\ &\approx r\mathcal{T} + f'(b)w_{12}\tau_h, \end{aligned} \quad (3.20)$$

where $f'(b)$ represents the slope of the nonlinear function $f(\cdot)$ at the baseline level b . This approximation leads to a conceptually simple method-of-moments estimator,

$$\hat{w}_{12} = (SS - r\mathcal{T})/f'(b)\tau_h. \quad (3.21)$$

Now, if the spike trains are down-sampled into time-bins of size Δ , we must estimate the statistic SS with a discrete sum instead:

$$\begin{aligned} SS^{ds} &= E \left[\sum_{t=t'+\Delta}^{t'+\Delta+\mathcal{T}} n_1^{ds}(t) \mid n_2^{ds}(t') = 1, n_2^{ds}(t) = 0 \forall t \in (t', t' + \mathcal{T}] \right] \\ &\approx r\mathcal{T} + f'(b) \int_0^{\Delta} \frac{dt'}{\Delta} \int_{\Delta}^{\Delta+\mathcal{T}} w_{12} \exp(-(t-t')/\tau_h) dt \\ &\approx r\mathcal{T} + f'(b)w_{12} \frac{1-\exp(-\Delta/\tau_h)}{\Delta/\tau_h^2}. \end{aligned} \quad (3.22)$$

$n^{ds}(t)$ here are down-sampled spikes, i.e. the spikes defined on a grid $t = 0, \Delta, 2\Delta, \dots$

In the second equality we made the approximation that the true position of the spike of the second neuron, $n_2^{ds}(t')$, may be uniformly distributed in the first time-bin $[0, \Delta]$, and the discrete sum over t is from the second time-bin $[\Delta, 2\Delta]$ to $[\mathcal{T}, \mathcal{T} + \Delta]$, i.e. over all spikes

CHAPTER 3. POP-OOPSI

of the first neuron that occurred in any of the strictly subsequent time-bins up to $\mathcal{T} + \Delta$.

Forming a method-of-moments estimator as in Eq. 3.21 leads to a biased estimate:

$$\hat{w}_{12}^{ds} \approx \frac{1 - \exp(-\Delta/\tau_h)}{\Delta/\tau_h} \hat{w}_{12}, \quad (3.23)$$

and somewhat surprisingly (given the rather crude nature of these approximations), this corresponds quite well with the scale bias we observe in practice. In Figure 3.5 we plot the scale bias from Eq. 3.23 versus that empirically deduced from our simulations for different values of Δ ; we see that Eq. 3.23 describes the observed scale bias fairly well. Thus we can divide by this analytically-derived factor to effectively correct the bias of our estimates, as shown in the right panel of Fig. 3.4.

3.3.2 Impact of prior information on the inference

Next we investigated the importance of incorporating prior information in our estimates. We found that imposing a sparse prior (as described in Section 3.2.5) significantly improved our results. For example, Fig. 3.6 illustrates a case in which our obtained r^2 increased from 0.64 (with no L_1 penalization in the M-step) to 0.85 (with penalization; the penalty λ was chosen approximately as the inverse mean absolute value of w_{ij} , which is known here because we prepared the network simulations but is available in practice given the previous physiological measurements discussed in section 3.2.7). See also Fig. 3.10 below. Furthermore, the weights estimated using the sparse prior more reliably provide the sign (i.e., excitatory or inhibitory) of each presynaptic neuron in the network (Figure 3.7).

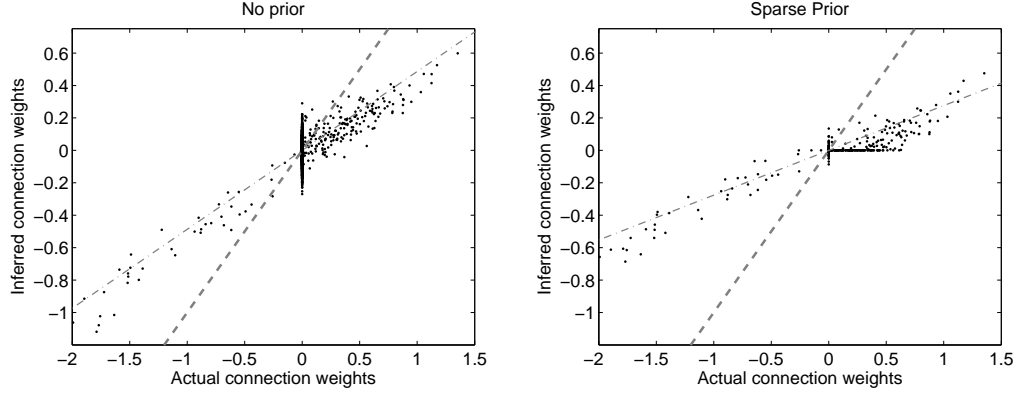


Figure 3.6: Imposing a sparse prior on connectivity improves our estimates. Scatter plots indicate the connection weights w_{ij} reconstructed using no prior ($r^2 = 0.64$; left panel) and a sparse prior ($r^2 = 0.85$; right panel) vs. the true connection weights in each case. These plots were based on a simulation of $N = 50$ neurons firing at ≈ 5 Hz, imaged for $T = 10$ min at 60 Hz, with $\text{eSNR} \approx 10$. Clearly, the sparse prior reduces the relative error, as indicated by comparing the relative distance between the data points (black dots) to the best linear fit (gray dash-dotted line), at the expense of some additional soft-threshold bias, as is usual in the L_1 setting.

Incorporation of Dale’s law, on the other hand, only leads to an $\approx 10\%$ change in the estimation r^2 in the absence of an L_1 penalty, and no significant improvement at all in the presence of an L_1 penalty (data not shown). Thus Dale’s prior was not pursued further here.

3.3.3 Impact of experimental factors on estimator accuracy

Next we sought to quantify the minimal experimental conditions necessary for accurate estimation of the connectivity matrix. Figure 3.8 shows the quality of the inferred connectivity matrix as a function of the imaging frame rate, and indicates that imaging frame rates ≥ 30 Hz are needed to achieve meaningful reconstruction results. This matches nicely with

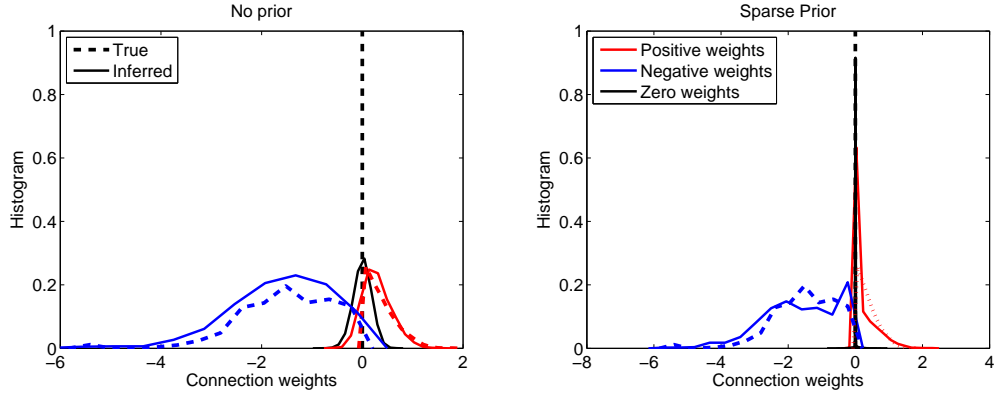


Figure 3.7: The distributions of inferred connection weights using no prior (left panel) and a sparse prior (right panel) vs. true distributions. When the sparse prior is enforced, zero weights are recovered with substantially higher frequency (black lines), thus allowing better identification of connected neural pairs. Likewise, excitatory and inhibitory weights are better recognized (red and blue lines, respectively), thus allowing accurate classification of neurons as excitatory or inhibitory. The normalized Hamming distance between the inferred and true connectivity matrix here (defined as $H(\mathbf{w}, \hat{\mathbf{w}}) = [N(N-1)]^{-1} \sum_{ij} |\text{sign}(w_{ij}) - \text{sign}(\hat{w}_{ij})|$, with the convention $\text{sign}(0) = 0$) was 0.06. Distributions are shown for a simulated population of $N = 200$ neurons firing at ≈ 5 Hz and imaged for $T = 10$ min at 60 Hz, with $\text{eSNR} \approx 10$. Note that the peak at zero in the true distributions (black dashed trace) corresponds to the vertical line visible at zero in Figs. 3.4 and 3.6.

currently-available technology; as discussed in the introduction, 30 or 60 Hz imaging is already in progress in a number of laboratories [74, 127–129], though in some cases higher imaging rates come at a cost in the signal-to-noise ratio of the images or in the number of neurons that may be imaged simultaneously. Similarly, Figure 3.9 illustrates the quality of the inferred connectivity matrix as a function of the effective SNR measure defined in Eq. (3.6).

Finally, Figure 3.10 shows the quality of the inferred connectivity matrix as a function of the experimental duration. The minimal amount of data for a particular r^2 depended substantially on whether the sparse prior was enforced. In particular, when not imposing

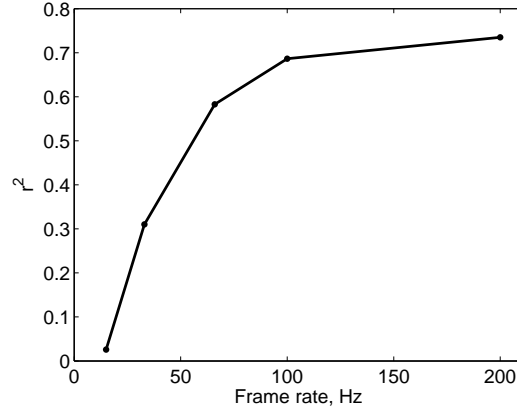


Figure 3.8: Accuracy of the inferred connectivity as a function of the frame rate of calcium imaging. A population of $N = 25$ neurons firing at ≈ 5 Hz and imaged for $T = 10$ min was simulated here, with $\text{eSNR} \approx 10$. At 100 Hz, r^2 saturated at the level $r^2 \approx 0.7$ achieved with $\Delta \rightarrow 0$.

a sparse prior, the calcium imaging duration necessary to achieve $r^2 = 0.5$ for the reconstructed connectivity matrix in this setting was $T \approx 10$ min, and $r^2 = 0.75$ was achieved at $T \approx 30$ min. With a sparse prior, $r^2 > 0.7$ was achieved already at $T \approx 5$ min. Furthermore, we observed that the accuracy of the reconstruction did not deteriorate dramatically with the size of the imaged neural population: roughly the same reconstruction quality was observed (given a fixed length of data) for N varying between 50–200 neurons. These results were consistent with a rough Fisher information computation which we performed but have omitted here to conserve space.

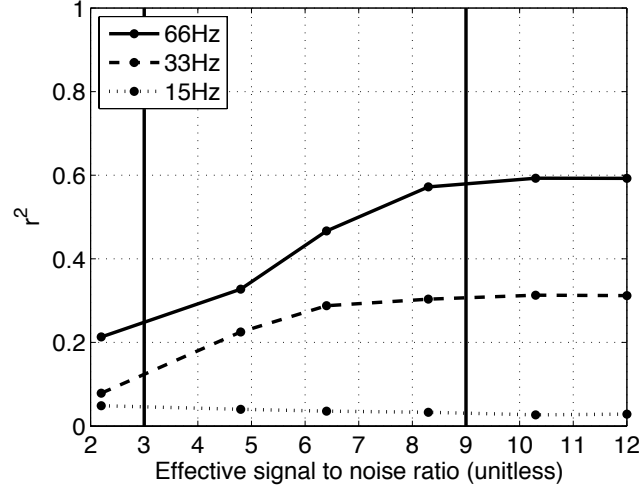


Figure 3.9: Accuracy of inferred connectivity as a function of effective imaging SNR (eSNR, defined in Eq. 3.6), for frame rates of 15, 33, and 66 Hz. Neural population simulation was the same as in Figure 3.8. Vertical black lines correspond to the eSNR values of the two example traces in Figure 3.3, for comparison.

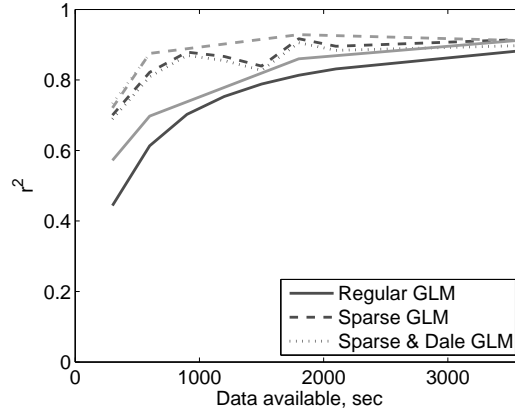


Figure 3.10: Accuracy of inferred connectivity as a function of the imaging time and neural population size. Incorporating a sparse prior dramatically increases the reconstruction quality (dashed lines). When the sparse prior is imposed, $T = 5$ min is sufficient to recover 70% of the variance in the connection weights. Incorporating Dale's prior leads to only marginal improvement (dotted line). Furthermore, reconstruction accuracy does not strongly depend on the neural population size, N . Here, neural populations of size $N = 100$ and 200 are shown (black and gray, respectively), with $\text{eSNR} \approx 10$ and 60 Hz imaging rate in each case.

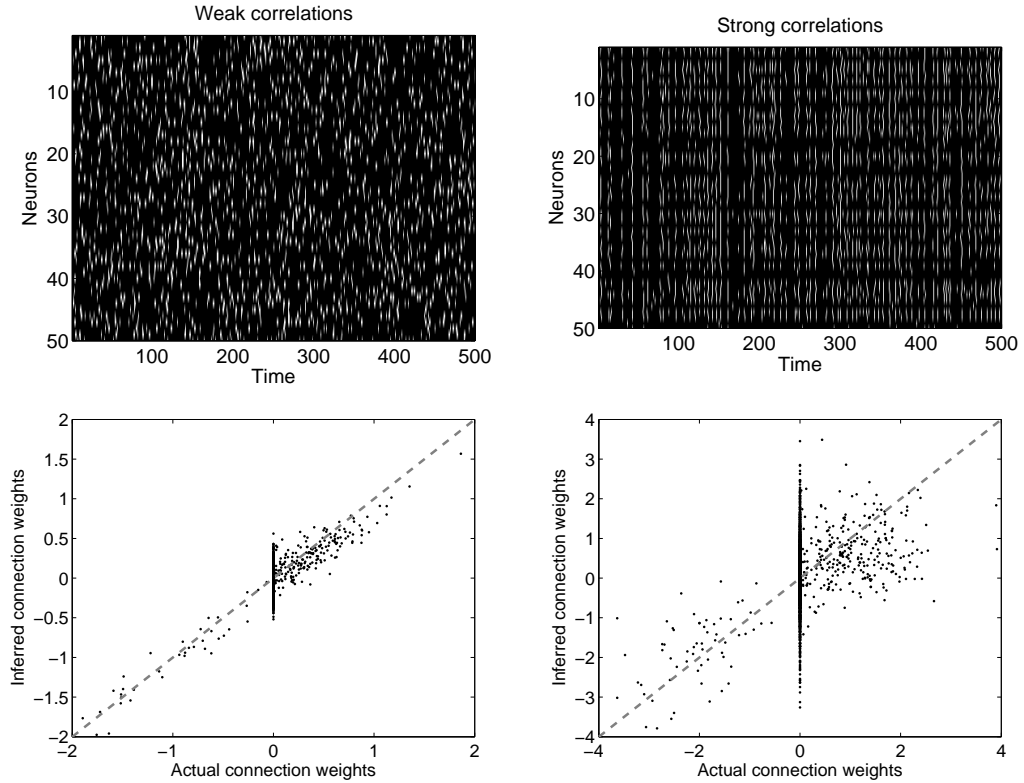


Figure 3.11: Diversity of observed neural activity patterns is required for accurate circuit inference. Here, 15 sec of simulated spike trains for a weakly coupled network (top left panel) and a network with strongly coupled component (top right panel) are shown. In weakly coupled networks, spikes are sufficiently uncorrelated to give access to enough different neural activity patterns to estimate the weights w . In a strongly coupled case, many highly synchronous events are evident (top right panel), thus preventing observation of a sufficiently rich ensemble of activity patterns. Accordingly, the connectivity estimates for the strongly coupled neural network (bottom right panel) does not represent the true connectivity of the circuit, even for the weakly coupled component. This is contrary to the weakly-coupled network (bottom left panel) where true connectivity is successfully obtained. Networks of $N = 50$ neurons firing at ≈ 5 Hz and imaged for $T = 10$ min at 60 Hz were used to produce this figure; eSNR ≈ 10 .

3.3.4 Impact of strong correlations and deviations from generative model on the inference

Estimation of network connectivity is fundamentally rooted in observing changes in the spike rate conditioned on the state of the other neurons. Considered from the point of view

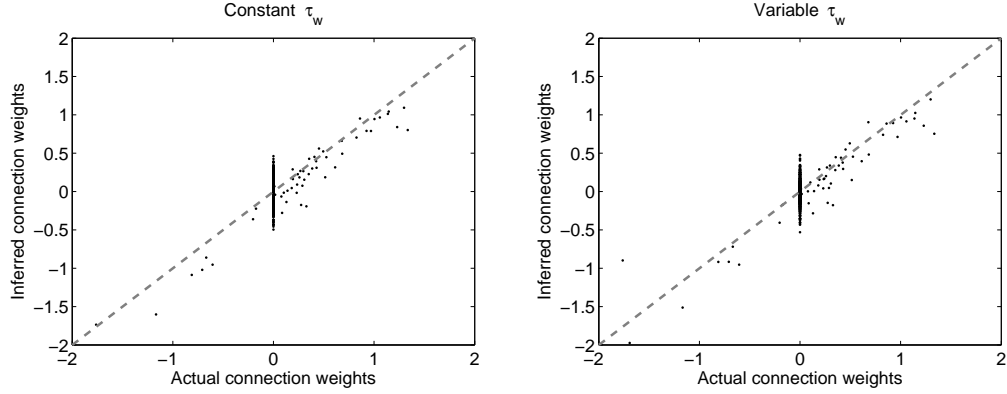


Figure 3.12: Inference is robust to deviations of the data from our generative model. With up to 25% variability allowed in PSP time scales τ_h (right panel), our algorithm provided reconstructions of almost the same quality as when all τ_h 's were the same (left panel). Simulation conditions were the same as in Figure 3.8, at 60 Hz imaging rate.

of estimating a standard GLM, it is clear that the inputs to our model (3.1) must satisfy certain basic identifiability conditions if we are to have any hope of accurately estimating the parameter w . In particular, we must rule out highly multicollinear inputs $\{h_{ij}(t)\}$: speaking roughly, the set of observed spike trains should be rich enough to span all N dimensions of w_i , for each cell i . In the simulations pursued here, the coupling matrix $\{w_{ij}\}_{i \neq j}$ was fairly weak and neurons fired largely independently of each other: see Fig. 3.11, upper left for an illustration. In this case of weakly-correlated firing, the inputs $\{h_{ij}(t)\}$ will also be weakly correlated, and the model should be identifiable, as indeed we found. Should this weak-coupling condition be violated, however (e.g., due to high correlations in the spiking of a few neurons), we may require much more data to obtain accurate estimates due to multicollinearity problems.

To explore this issue, we carried out a simulation of a hypothetical strongly coupled neural network, where in addition to the physiologically-relevant weak sparse connectivity

CHAPTER 3. POP-OOPSI

discussed in section 3.2.7 we introduced a sparse random strong connectivity component. More specifically, we allowed a fraction of neurons to couple strongly to the other neurons, making these “command” neurons which in turn could strongly drive the activity of the rest of the population [174]. The strength of this strong connectivity component was chosen to dynamically build up the actual firing rate from the baseline rate of $f(b) \approx 1$ Hz to approximately 5 Hz. Such a network showed patterns of activity very different from the weakly coupled networks inspected above (Figure 3.11, top right). In particular, a large number of highly correlated events across many neurons were evident in this network. As expected, our algorithm was not able to identify the true connectivity matrix correctly in this scenario (Figure 3.11, bottom right panel). For ease of comparison, the left panels show a “typical” network (i.e., one lacking many strongly coupled neurons), and its associated connectivity inference.

On the other hand, our inference algorithm showed significant robustness to model misspecification, i.e., deviations from our generative model. One important such deviation is variation in the time scales of PSPs in different synapses. Up to now, all PSP time-scales were assumed to be the same, i.e., $\{\tau_{ij}^h\}_{i,j \leq N} = \tau_h$. In Figure 3.12 we introduce additional variability in τ_h from one neuron to another. Variability in τ_h results in added variance in the estimates of the connectivity weights, w_{ij} , through the τ_h -dependence of the scaling factor Eq. (3.23). However, we found that this additional variance was relatively insignificant in cases where τ_h varied up to 25% from neuron to neuron. We also found that inference was robust to changes in the sparseness of the underlying connectivity matrix: we simu-

lated neural populations of size $N = 25$ and $N = 50$ neurons, as above, with connection sparseness varying from 5% (very sparse) to 100% (all-to-all), and in all cases the performance of our algorithm remained stable, with $r^2 \approx 0.9$ for the estimate of the connected weights, $w_{ij} \neq 0$ (data not shown). Finally, simulations with more biophysically-based conductance-driven noisy integrate-and-fire network models [175] led to qualitatively similar results, further establishing the robustness of these methods; again, details are omitted to conserve space.

3.4 Discussion

In this paper we develop a Bayesian approach for inferring connectivity in a network of spiking neurons observed using calcium fluorescent imaging. A number of previous authors have addressed the problem of inferring neuronal connectivity given a fully-observed set of spike trains in a network [131–133, 135–142, 176, 177], but the main challenge in the present work is the indirect nature of the calcium imaging data, which provides only noisy, low-pass filtered, temporally sub-sampled observations of spikes of individual neurons. To solve this problem, we developed a factorized approximation to sample spikes jointly 3.2.4. The connectivity matrix is then inferred in an EM framework; the M-step parallelizes quite efficiently and allows for the easy incorporation of prior sparseness information, which significantly reduces data requirements in this context. We have found that these methods can effectively infer the connectivity in simulated neuronal networks, given reasonable

CHAPTER 3. POP-OOPSI

lengths of data, computation time, and assumptions on the biophysical network parameters.

To our knowledge, we are the first to address this problem using the statistical deconvolution methods and EM formulation described here (though see also [130], who fit simplified, low temporal resolution transition-based models to the 10 Hz calcium data obtained by [6]). However, we should note that [137] developed a closely related approach to infer connectivity from low-SNR electrical recordings involving possibly-misclassified spikes (in contrast to the slow, lowpass-filtered calcium signals we discuss here). In particular, these authors employed a very similar Bernoulli GLM and developed a Metropolis-within-Gibbs sampler to approximate the necessary sufficient statistics for their model. In addition, [137] develop a more intricate hierarchical prior for the connectivity parameter w ; while we found that a simple L_1 penalization was quite effective here, it will be worthwhile to explore more informative priors in future work.

A number of possible improvements of our method are available. One of the biggest challenges for inferring neural connectivity from functional data is the presence of indirect inputs from unobserved neurons [139–141, 178, 179]: it is typically impossible to observe the activity of all neurons in a given circuit, and correlations in the unobserved inputs can mimic connections among different observed neurons. Developing methods to cope with such unobserved common inputs is currently an area of active research, and should certainly be incorporated in the methods we have developed here.

Several other important directions for future work are worth noting. First, recently developed photo-stimulation methods for activating or deactivating individual neurons or

CHAPTER 3. POP-OOPSI

sub-populations [180–182] may be useful to increase statistical power in cases where the circuit’s unperturbed activity may not allow reliable determination of a circuit’s connectivity matrix; in particular, by utilizing external stimulation, we can in principle choose a sufficiently rich experimental design (i.e., a sample of input activity patterns) to overcome the multicollinearity problems discussed in the context of Fig. 3.11.

Second, improvements of the algorithms for faster implementation are under development. Specifically, fast non-negative optimization-based deconvolution methods may be a promising alternative [183, 184] to the SMC approach used here. In addition, modifications of our generative model to incorporate non-stationarities in the fluorescent signal (e.g., due to dye bleaching and drift) are fairly straightforward.

Third, a fully Bayesian algorithm for estimating the posterior distributions of all the parameters (instead of just the MAP estimate) would be of significant interest. Such a fully-Bayesian extension is conceptually simple: we just need to extend the Gibbs sampler from [39] to additionally sample from the parameter θ given the sampled spike trains \mathbf{X} . Since we already have a method for drawing \mathbf{X} given θ and \mathbf{F} , with such an additional sampler we may obtain samples from $P(\mathbf{X}, \theta | \mathbf{F})$ simply by sampling from $\mathbf{X} \sim P(\mathbf{X} | \theta, \mathbf{F})$ and $\theta \sim P(\theta | \mathbf{X})$, via blockwise-Gibbs. Sampling from the posteriors $P(\theta | \mathbf{X})$ in the GLM setting is quite tractable using hybrid Monte Carlo methods, since all of the necessary posteriors are log-concave [185–188].

Finally, most importantly, we are currently applying these algorithms in preliminary experiments on real data. Checking the accuracy of our estimates is of course more chal-

CHAPTER 3. POP-OOPSI

lenging in the context of non-simulated data, but a number of methods for partial validation are available, including multiple-patch recordings [162], photostimulation techniques [189], and fluorescent anatomical markers which can distinguish between different cell types [190] (i.e., inhibitory vs. excitatory cells; c.f. Fig. 3.7). We hope to present our results in the near future.

Chapter 4

discussion

In the first two chapters, filters were developed to infer spike trains from calcium fluorescence imaging. In the third chapter, these filters were used to infer connectivity between simultaneously observed neurons. Specifically, assuming reasonable spiking and observation statistics, a large fraction of the variance of connectivity parameters could reliably be estimated with these tools. That being said, these methods can be extended in a number of reasonably straightforward ways. More specifically, the idealized typical experimental workflow assumed in the above proceeds as follows:

1. obtain a sequence of images
2. if *in vivo*, register each frame
3. segment registered frames into ROIs
4. obtain fluorescence traces from each ROI

CHAPTER 4. DISCUSSION

5. infer spike trains from each trace
6. infer connectivity between observable neurons
7. confirm connectivity between observable neurons.

The first step is not at issue here. The next two were assumed to be solved in the above, but can be easily incorporated in the framework developed, as discussed in Section 4.1. The fourth step has been addressed in Sections 1.2.5 – 1.2.6 and 1.3.4 – 1.3.5, but can also be somewhat extended as discussed in Section 4.2. The fifth step is the focus of Chapters 1 and 2; nonetheless, both these approaches are currently being further developed, as described in Section 4.3. While the sixth step was the focus of Chapter 3, Section 4.4 touches on some possible avenues for improvement. Finally, although the last step was not mentioned at all above, Section 4.5 discusses some not too distant possibilities.

4.1 Towards improving image preprocessing

Typically, for *in vivo* experiments, performing image registration before processing the movie can enhance the effective SNR [103, 191]. This step, however, has been uncoupled to the segmentation step. Figure 3 provides pseudocode for an algorithm that tackles both steps together. It seems likely (to us) that the below algorithm would be both more efficient and more effective than previously proposed algorithms.

The intuition behind is as follows. Neurons, when imaged in 2D, they typically appear approximately circular, or like ellipses. Further, the variability in circle (or ellipse)

CHAPTER 4. DISCUSSION

diameter(s) is relatively small, for a particular experimental trial. Thus, given (manually) the average size of a cell, a simple template matching algorithm could initialize a more sophisticated algorithm to find cell bodies. The template matching can be performed quickly using the `filter` command in Matlab, finding the peak, extracting the ROI, and repeating. Because the number of parameters governing circles (and ellipses) is small — 2 define the center, another one (two) for the radius(s) — gradient ascent can be used to ascend the gradient along each parameter, to fine-tune these parameters for each cell. These operations can be performed initially on the mean frame. Then, since each ROI may drift within the image field independently of the others, by cycling through the sequence of images, one can update each ROI parameter again using gradient ascent techniques. Upon conclusion, the result is a set of pixels, for each ROI, in each frame. Note that this approach would not deal at all with the potentially more problematic issue of z-plane drift.

4.2 Towards improving spatial filtering

The spatial filtering described in Chapter 1 seems very promising. The next natural step is to test the procedure both *in vitro* and *in vivo*, to determine how it effects the effective SNR. Beyond that, generalizing the SMC method to incorporate spatial filtering might further enhance this step. After that, the most natural generalization to the model is to relax the constraint on the covariance matrix. In particular, above it was assumed that the covariance matrix was a constant times the identity matrix:

CHAPTER 4. DISCUSSION

Algorithm 3 Pseudocode for performing segmentation across images that are not registered.

Obtain mean image frame

Specify mean ROI size

Use 2D template matching to find cell body centers on mean frame

Manually add/remove any “mistakes”

Recursively compute the gradient for each parameter and each ROI, ascend the likelihood, converge for each ROI upon finding a local maxima

Manually make any desired “corrections”

for all $t = 1 \dots T$ **do**

 Update parameters for each ROI, again using gradient ascent techniques

end for

Output the set of pixels within each ROI as a function of time to spike inference filters.

$$\vec{F} = \vec{\alpha}(C_t + b) + \sigma, \quad \sigma \sim \mathcal{N}(\mathbf{0}, \mathbf{I}). \quad (4.1)$$

The natural next step would be to relax the constraint that each pixel had the same variance, and make the the covariance matrix a diagonal, or have some other low-rank structure. An important advancement may come from dealing with neuropil contamination for *in vivo* data.

4.3 Towards improving spike inference

Chapter 1 describes how the fast filter might benefit by further analysis on the nonlinear, Poisson, and time-varying prior extensions. The SMC filter can also be extended in several natural ways: (i) modify observation distribution to be Poisson, (ii) allow for Poisson (instead of simply binary) spiking, or (iii) integrate out the calcium dynamics to construct a Rao-Blackwellized particle filter [84]. Further, other approaches to filtering have shown promise in related fields. A particularly relevant example, [38], develops a reversible-jump Markov Chain Monte Carlo method to infer spikes from very similar data. This strategy might be directly applicable, or a slight modification, to use a Dirichlet process to determine the number of spikes in a trace [192]. This last idea seems especially interesting, and is currently under development. It naturally leads to a fully Bayesian approach for jointly inferring the posterior distribution of spikes trains and parameters.

4.4 Towards improving connectivity learning

In Chapter 3, it was shown that incorporating a sparse prior on the connectivity matrix can significantly reduce the amount of data necessary to achieve a certain r^2 value. The improvements to spike inference described above could provide cleaner data, resulting in further improvement. In addition to the published methods for inferring the most likely connectivity matrix, one can compute the uncertainty associated with each synaptic strength (Y. Mishchenko, unpublished). Thus, if one had the ability to directly activate

CHAPTER 4. DISCUSSION

individual neurons, or small populations of neurons, one could design optimal experiments for efficiently inferring connectivity [193–195].

Fortunately, the experimental tools for directly stimulated individual neurons are rapidly advancing. Various methods for stimulating neurons with light have been developed recently [196], including two-photon uncaging of glutamate [189, 197] and optogenetics [180]. In the last year, various labs have shown two-photon activation of channel rhodopsin [198, 199], and even more recently, it has been shown that a two-photon laser can be used to evoke spikes in neurons (K. Deisseroth, personal communication).

4.5 Towards confirming connectivity

The above photostimulation tools may also be employed for conformational experiments. In particular, by coupling patch clamping and photostimulation, one can relatively rapidly activate all the potential presynaptic neurons in an imaging plane [182]. Simultaneous imaging, to confirm that the light in fact evoked spikes, allows one to then determine which neurons spiked due to the light, and the effective EPSP size of each, which can serve as the ground truth for connectivity.

Perhaps more simply, one could conduct the connectivity inference experiments in animals or slices that express fluorescent proteins only in inhibitory neurons [200]. Thus, while one could not confirm the magnitude of connection strength, the sign of connection strength could be confirmed. Similarly, electroporation [7, 46] of mono-synaptically

CHAPTER 4. DISCUSSION

restricted tracer rabies viruses [201] into the patched cell could act as another source of ground-truth information regarding connectivity. All these approaches are currently being pursued.

Bibliography

- [1] S. Ramon y Cajal, *La Textura del Sistema Nerviosa del Hombre y los Vertebrados*. Moya, 1904.
- [2] G. Shepherd, *The synaptic organization of the brain*. Oxford University Press New York, 2004.
- [3] K. Friston, “Functional and effective connectivity in neuroimaging: a synthesis,” *Human Brain Mapping*, vol. 2, no. 1-2, pp. 56–78, 1994.
- [4] R. Yuste and A. Konnerth, *Imaging in Neuroscience and Development, A Laboratory Manual*, 2006.
- [5] D. Smetters, A. Majewska, and R. Yuste, “Detecting action potentials in neuronal populations with calcium imaging,” *Methods*, vol. 18, no. 2, pp. 215–221, Jun 1999.
- [6] Y. Ikegaya, G. Aaron, R. Cossart, D. Aronov, I. Lampl, D. Ferster, and R. Yuste, “Synfire chains and cortical songs: temporal modules of cortical activity,” *Science*, vol. 304, no. 5670, pp. 559–564, Apr 2004.

BIBLIOGRAPHY

- [7] S. Nagayama, S. Zeng, W. Xiong, M. L. Fletcher, A. V. Masurkar, D. J. Davis, V. A. Pieribone, and W. R. Chen, “In vivo simultaneous tracing and Ca^{2+} imaging of local neuronal circuits.” *Neuron*, vol. 53, no. 6, pp. 789–803, Mar 2007. [Online]. Available: <http://dx.doi.org/10.1016/j.neuron.2007.02.018>
- [8] W. Göbel and F. Helmchen, “In vivo calcium imaging of neural network function.” *Physiology (Bethesda)*, vol. 22, pp. 358–365, Dec 2007. [Online]. Available: <http://dx.doi.org/10.1152/physiol.00032.2007>
- [9] L. Luo, E. M. Callaway, and K. Svoboda, “Genetic dissection of neural circuits.” *Neuron*, vol. 57, no. 5, pp. 634–660, Mar 2008. [Online]. Available: <http://dx.doi.org/10.1016/j.neuron.2008.01.002>
- [10] O. Garaschuk, O. Griesbeck, and A. Konnerth, “Troponin c-based biosensors: a new family of genetically encoded indicators for in vivo calcium imaging in the nervous system.” *Cell Calcium*, vol. 42, no. 4-5, pp. 351–361, 2007. [Online]. Available: <http://dx.doi.org/10.1016/j.ceca.2007.02.011>
- [11] M. Mank, A. F. Santos, S. Drenth, T. D. Mrsic-Flogel, S. B. Hofer, V. Stein, T. Hendel, D. F. Reiff, C. Levelt, A. Borst, T. Bonhoeffer, M. Hübner, and O. Griesbeck, “A genetically encoded calcium indicator for chronic in vivo two-photon imaging.” *Nat Methods*, vol. 5, no. 9, pp. 805–811, Sep 2008. [Online]. Available: <http://dx.doi.org/10.1038/nmeth.1243>
- [12] D. J. Wallace, S. M. zum Alten Borgloh, S. Astori, Y. Yang, M. Bausen,

BIBLIOGRAPHY

- S. Kglér, A. E. Palmer, R. Y. Tsien, R. Sprengel, J. N. D. Kerr, W. Denk, and M. T. Hasan, “Single-spike detection in vitro and in vivo with a genetic Ca²⁺ sensor.” *Nat Methods*, vol. 5, no. 9, pp. 797–804, Sep 2008. [Online]. Available: <http://dx.doi.org/10.1038/nmeth.1242>
- [13] T. Schwartz, D. Rabinowitz, V. K. Unni, V. S. Kumar, D. K. Smetters, A. Tsiola, and R. Yuste, “Networks of coactive neurons in developing layer 1.” *Neuron*, vol. 20, pp. 1271–1283, 1998.
- [14] B. Mao, F. Hamzei-Sichani, D. Aronov, R. Froemke, and R. Yuste, “Dynamics of spontaneous activity in neocortical slices,” *Neuron*, vol. 32, no. 5, pp. 883–98, 2001.
- [15] D. S. Greenberg, A. R. Houweling, and J. N. D. Kerr, “Population imaging of ongoing neuronal activity in the visual cortex of awake rats.” *Nat Neurosci*, vol. 11, no. 7, pp. 749 – 751, Jun 2008. [Online]. Available: <http://dx.doi.org/10.1038/nn.2140>
- [16] T. F. Holekamp, D. Turaga, and T. E. Holy, “Fast three-dimensional fluorescence imaging of activity in neural populations by objective-coupled planar illumination microscopy.” *Neuron*, vol. 57, no. 5, pp. 661–672, Mar 2008. [Online]. Available: <http://dx.doi.org/10.1016/j.neuron.2008.01.011>
- [17] T. Sasaki, N. Takahashi, N. Matsuki, and Y. Ikegaya, “Fast and accurate detection of action potentials from somatic calcium fluctuations.” *Journal of*

BIBLIOGRAPHY

- Neurophysiology*, vol. 100, no. 3, p. 1668, Jul 2008. [Online]. Available: <http://dx.doi.org/10.1152/jn.00084.2008>
- [18] J. T. Vogelstein, B. O. Watson, A. M. Packer, R. Yuste, B. Jedynek, and L. Paninski, “Spike inference from calcium imaging using sequential monte carlo methods.” *Biophys J*, vol. 97, no. 2, pp. 636–655, Jul 2009. [Online]. Available: <http://dx.doi.org/10.1016/j.bpj.2008.08.005>
- [19] L. F. Portugal, J. J. Judice, and L. N. Vicente, “A comparison of block pivoting and interior-point algorithms for linear least squares problems with nonnegative variables,” *Mathematics of Computation*, vol. 63, no. 208, pp. 625–643, 1994.
- [20] J. Markham and J.-A. Conchello, “Parametric blind deconvolution: a robust method for the simultaneous estimation of image and blur.” *Journal of The Optical Society Of America A. Optics, Image Science, and Vision*, vol. 16, no. 10, pp. 2377–2391, Oct 1999.
- [21] D. D. Lee and H. S. Seung, “Learning the parts of objects by non-negative matrix factorization.” *Nature*, vol. 401, no. 6755, pp. 788–791, Oct 1999. [Online]. Available: <http://dx.doi.org/10.1038/44565>
- [22] Y. Lin, D. D. Lee, and L. K. Saul, “Nonnegative deconvolution for time of arrival estimation,” *International Conference on Acoustics, Speech, and Signal Processing*, 2004.

BIBLIOGRAPHY

- [23] O’Grady, Paul D. and Pearlmutter, Barak A., “Convolutional non-negative matrix factorisation with a sparseness constraint,” *Machine Learning for Signal Processing, 2006. Proceedings of the 2006 16th IEEE Signal Processing Society Workshop on*, pp. 427–432, 2006.
- [24] Q. J. M. Huys, M. B. Ahrens, and L. Paninski, “Efficient estimation of detailed single-neuron models.” *J Neurophysiol*, vol. 96, no. 2, pp. 872–890, Aug 2006.
[Online]. Available: <http://dx.doi.org/10.1152/jn.00079.2006>
- [25] J. P. Cunningham, K. V. Shenoy, and M. Sahani, “Fast Gaussian process methods for point process intensity estimation,” *ICML*, pp. 192–199, 2008.
- [26] L. Paninski, Y. Ahmadian, D. Ferreira, S. Koyama, K. R. Rad, M. Vidne, J. Vogelstein, and W. Wu, “A new look at state-space models for neural data.” *J Comput Neurosci*, Aug 2009. [Online]. Available: <http://dx.doi.org/10.1007/s10827-009-0179-x>
- [27] S. Boyd and L. Vandenberghe, *Convex Optimization*. Oxford University Press, 2004.
- [28] W. Press, S. Teukolsky, W. Vetterling, and B. Flannery, *Numerical recipes in C*. Cambridge University Press, 1992.
- [29] E. Yaksi and R. W. Friedrich, “Reconstruction of firing rate changes across neuronal

BIBLIOGRAPHY

- populations by temporally deconvolved Ca^{2+} imaging,” *Nature Methods*, vol. 3, no. 5, pp. 377–383, May 2006.
- [30] T. A. Pologruto, R. Yasuda, and K. Svoboda, “Monitoring neural activity and $[\text{Ca}^{2+}]$ with genetically encoded Ca^{2+} indicators.” *J Neurosci*, vol. 24, no. 43, pp. 9572–9579, Oct 2004. [Online]. Available: <http://dx.doi.org/10.1523/JNEUROSCI.2854-04.2004>
- [31] R. Kass and A. Raftery, “Bayes Factors,” *Journal of the American Statistical Association*, vol. 90, no. 430, pp. 773–795, 1995.
- [32] R. Horn and C. Johnson, *Matrix analysis*. Cambridge Univ Pr, 1990.
- [33] E. A. Mukamel, A. Nimmerjahn, and M. J. Schnitzer, “Automated analysis of cellular signals from large-scale calcium imaging data.” *Neuron*, vol. 63, no. 6, pp. 747–760, Sep 2009. [Online]. Available: <http://dx.doi.org/10.1016/j.neuron.2009.08.009>
- [34] V. Rokhlin, A. Szlam, and M. Tygert, “A randomized algorithm for principal component analysis,” *SIAM J. Matrix Anal. Appl*, vol. 31, pp. 1100–1124, 2009.
- [35] J. N. MacLean, B. O. Watson, G. B. Aaron, and R. Yuste, “Internal dynamics determine the cortical response to thalamic stimulation.” *Neuron*, vol. 48, no. 5, pp. 811–823, Dec 2005. [Online]. Available: <http://dx.doi.org/10.1016/j.neuron.2005.09.035>
- [36] L. Sjulson and G. Miesenböck, “Optical recording of action potentials and other discrete physiological events: a perspective from signal detection theory.”

BIBLIOGRAPHY

- Physiology (Bethesda)*, vol. 22, pp. 47–55, Feb 2007. [Online]. Available: <http://dx.doi.org/10.1152/physiol.00036.2006>
- [37] A. J. Bell and T. J. Sejnowski, “An information-maximisation approach to blind separation and blind deconvolution,” *Neural Computation*, vol. 7, no. 6, p. 1004, 1995.
- [38] C. Andrieu, É. Barat, and A. Doucet, “Bayesian deconvolution of noisy filtered point processes,” *IEEE Transactions on Signal Processing*, vol. 49, no. 1, pp. 134–146, 2001.
- [39] M. Y. V. JT, and P. L, “A Bayesian approach for inferring neuronal connectivity from calcium fluorescent imaging data,” *Annals of Applied Statistics*, vol. in press, 2009.
- [40] J. H. Friedman and W. Stuetzle, “Projection Pursuit Regression.” *J. AM. STAT. ASSOC.*, vol. 76, no. 376, pp. 817–823, 1981.
- [41] S. Mallat and Z. Zhang, “Matching pursuit with time-frequency dictionaries: IEEE Trans,” *Signal Processing*, vol. 41, pp. 3397–3415, 1993.
- [42] R. Y. Tsien, “A non-disruptive technique for loading calcium buffers and indicators into cells.” *Nature*, vol. 290, no. 5806, pp. 527–528, Apr 1981.
- [43] R. Yuste and L. C. Katz, “Control of postsynaptic ca^{2+} influx in developing neo-cortex by excitatory and inhibitory neurotransmitters.” *Neuron*, vol. 6, no. 3, pp. 333–344, Mar 1991.

BIBLIOGRAPHY

- [44] E. Brusteiu, N. Marandi, Y. Kovalchuk, P. Drapeau, and A. Konnerth, “In vivo monitoring of neuronal network activity in zebrafish by two-photon Ca^{2+} imaging.” *Pflugers Arch*, vol. 446, no. 6, pp. 766–773, Sep 2003. [Online]. Available: <http://dx.doi.org/10.1007/s00424-003-1138-4>
- [45] C. Stosiek, O. Garaschuk, K. Holthoff, and A. Konnerth, “In vivo two-photon calcium imaging of neuronal networks,” *Proceedings of The National Academy Of Sciences Of The United States Of America*, vol. 100, no. 12, pp. 7319–7324, Jun 2003.
- [46] T. Nevian and F. Helmchen, “Calcium indicator loading of neurons using single-cell electroporation.” *Pflugers Arch*, vol. 454, no. 4, pp. 675–688, Jul 2007. [Online]. Available: <http://dx.doi.org/10.1007/s00424-007-0234-2>
- [47] A. Miyawaki, J. Llopis, R. Heim, J. McCaffery, J. Adams, M. Ikura, and R. Tsien, “Fluorescent indicators for Ca^{2+} based on green fluorescent proteins and calmodulin.” *Nature*, vol. 388, no. 6645, pp. 882–7, 1997.
- [48] O. Griesbeck, G. S. Baird, R. E. Campbell, D. A. Zacharias, and R. Y. Tsien, “Reducing the environmental sensitivity of yellow fluorescent protein. mechanism and applications.” *J Biol Chem*, vol. 276, no. 31, pp. 29 188–29 194, Aug 2001. [Online]. Available: <http://dx.doi.org/10.1074/jbc.M102815200>
- [49] J. Nakai, M. Ohkura, and K. Imoto, “A high signal-to-noise Ca^{2+} probe composed of a single green fluorescent protein.” *Nat Biotechnol*, vol. 19, no. 2, pp. 137–141, Feb 2001. [Online]. Available: <http://dx.doi.org/10.1038/84397>

BIBLIOGRAPHY

- [50] W. Denk, J. H. Strickler, and W. W. Webb, “Two-photon laser scanning fluorescence microscopy,” *Science*, vol. 248, no. 4951, pp. 73–76, Apr 1990.
- [51] M. Oheim, E. Beaupaire, E. Chaigneau, J. Mertz, and S. Charpak, “Two-photon microscopy in brain tissue: parameters influencing the imaging depth,” *Journal of neuroscience methods*, vol. 111, no. 1, pp. 29–37, 2001.
- [52] P. Theer, M. T. Hasan, and W. Denk, “Two-photon imaging to a depth of 1000 μm in living brains by use of a $\text{Ti:Al}_2\text{O}_3$ regenerative amplifier,” *Opt Lett*, vol. 28, no. 12, pp. 1022–1024, Jun 2003.
- [53] B. A. Flusberg, E. D. Cocker, W. Piyawattanametha, J. C. Jung, E. L. M. Cheung, and M. J. Schnitzer, “Fiber-optic fluorescence imaging,” *Nat Methods*, vol. 2, no. 12, pp. 941–950, Dec 2005. [Online]. Available: <http://dx.doi.org/10.1038/nmeth820>
- [54] W. Müller and J. A. Connor, “Dendritic spines as individual neuronal compartments for synaptic Ca^{2+} responses,” *Nature*, vol. 354, no. 6348, pp. 73–76, Nov 1991. [Online]. Available: <http://dx.doi.org/10.1038/354073a0>
- [55] R. Yuste and W. Denk, “Dendritic spines as basic functional units of neuronal integration,” *Nature*, vol. 375, no. 6533, pp. 682–684, Jun 1995. [Online]. Available: <http://dx.doi.org/10.1038/375682a0>
- [56] F. Engert and T. Bonhoeffer, “Dendritic spine changes associated with hippocampal

BIBLIOGRAPHY

- long-term synaptic plasticity.” *Nature*, vol. 399, no. 6731, pp. 66–70, May 1999. [Online]. Available: <http://dx.doi.org/10.1038/19978>
- [57] E. A. Nimchinsky, R. Yasuda, T. G. Oertner, and K. Svoboda, “The number of glutamate receptors opened by synaptic stimulation in single hippocampal spines.” *J Neurosci*, vol. 24, no. 8, pp. 2054–2064, Feb 2004. [Online]. Available: <http://dx.doi.org/10.1523/JNEUROSCI.5066-03.2004>
- [58] A. Majewska, G. Yiu, and R. Yuste, “A custom-made two-photon microscope and deconvolution system.” *Pflugers Arch*, vol. 441, no. 2-3, pp. 398–408, Dec 2000.
- [59] V. Scheuss, R. Yasuda, A. Sobczyk, and K. Svoboda, “Nonlinear $[Ca^{2+}]$ signaling in dendrites and spines caused by activity-dependent depression of Ca^{2+} extrusion.” *J Neurosci*, vol. 26, no. 31, pp. 8183–8194, Aug 2006. [Online]. Available: <http://dx.doi.org/10.1523/JNEUROSCI.1962-06.2006>
- [60] A. D. Sdrulla and D. J. Linden, “Double dissociation between long-term depression and dendritic spine morphology in cerebellar purkinje cells.” *Nat Neurosci*, vol. 10, no. 5, pp. 546–548, May 2007. [Online]. Available: <http://dx.doi.org/10.1038/nn1889>
- [61] A. K. Majewska, J. R. Newton, and M. Sur, “Remodeling of synaptic structure in sensory cortical areas in vivo.” *J Neurosci*, vol. 26, no. 11, pp. 3021–3029, Mar 2006. [Online]. Available: <http://dx.doi.org/10.1523/JNEUROSCI.4454-05.2006>

BIBLIOGRAPHY

- [62] S. D. Brenowitz and W. G. Regehr, “Reliability and heterogeneity of calcium signaling at single presynaptic boutons of cerebellar granule cells.” *J Neurosci*, vol. 27, no. 30, pp. 7888–7898, Jul 2007. [Online]. Available: <http://dx.doi.org/10.1523/JNEUROSCI.1064-07.2007>
- [63] F. Helmchen, K. Imoto, and B. Sakmann, “Ca²⁺ buffering and action potential-evoked Ca²⁺ signaling in dendrites of pyramidal neurons.” *Biophys J*, vol. 70, no. 2, pp. 1069–1081, Feb 1996.
- [64] K. Svoboda, D. W. Tank, and W. Denk, “Direct measurement of coupling between dendritic spines and shafts.” *Science*, vol. 272, no. 5262, pp. 716–719, May 1996.
- [65] M. Maravall, Z. F. Mainen, B. L. Sabatini, and K. Svoboda, “Estimating intracellular calcium concentrations and buffering without wavelength ratioing.” *Biophys J*, vol. 78, no. 5, pp. 2655–2667, May 2000.
- [66] D. M. O’Malley, Y. H. Kao, and J. R. Fetcho, “Imaging the functional organization of zebrafish hindbrain segments during escape behaviors.” *Neuron*, vol. 17, no. 6, pp. 1145–1155, Dec 1996.
- [67] C. M. Niell and S. J. Smith, “Functional imaging reveals rapid development of visual response properties in the zebrafish tectum.” *Neuron*, vol. 45, no. 6, pp. 941–951, Mar 2005. [Online]. Available: <http://dx.doi.org/10.1016/j.neuron.2005.01.047>
- [68] K. Ohki, S. Chung, Y. H. Ch’ng, P. Kara, and R. C. Reid, “Functional imaging with

BIBLIOGRAPHY

- cellular resolution reveals precise micro-architecture in visual cortex,” *Nature*, vol. 433, no. 7026, pp. 597–603, Feb 2005.
- [69] K. Ohki, S. Chung, P. Kara, M. Hubener, T. Bonhoeffer, and R. C. Reid, “Highly ordered arrangement of single neurons in orientation pinwheels.” *Nature*, vol. 442, no. 7105, pp. 925–928, Aug 2006. [Online]. Available: <http://dx.doi.org/10.1038/nature05019>
- [70] E. Yaksi, B. Judkewitz, and R. W. Friedrich, “Topological reorganization of odor representations in the olfactory bulb.” *PLoS Biol*, vol. 5, no. 7, p. e178, Jul 2007. [Online]. Available: <http://dx.doi.org/10.1371/journal.pbio.0050178>
- [71] T. R. Sato, N. W. Gray, Z. F. Mainen, and K. Svoboda, “The functional microarchitecture of the mouse barrel cortex.” *PLoS Biol*, vol. 5, no. 7, p. e189, Jul 2007. [Online]. Available: <http://dx.doi.org/10.1371/journal.pbio.0050189>
- [72] C. M. Root, J. L. Semmelhack, A. M. Wong, J. Flores, and J. W. Wang, “Propagation of olfactory information in drosophila.” *Proc Natl Acad Sci U S A*, vol. 104, no. 28, pp. 11 826–11 831, Jul 2007. [Online]. Available: <http://dx.doi.org/10.1073/pnas.0704523104>
- [73] G. Y. Fan, H. Fujisaki, A. Miyawaki, R. K. Tsay, R. Y. Tsien, and M. H. Ellisman, “Video-rate scanning two-photon excitation fluorescence microscopy and ratio imaging with cameleons,” *Biophysical Journal*, vol. 76, no. 5, pp. 2412–2420, May 1999.

BIBLIOGRAPHY

- [74] Q. T. Nguyen, N. Callamaras, C. Hsieh, and I. Parker, "Construction of a two-photon microscope for video-rate Ca^{2+} imaging." *Cell Calcium*, vol. 30, no. 6, pp. 383–393, Dec 2001. [Online]. Available: <http://dx.doi.org/10.1054/ceca.2001.0246>
- [75] V. Iyer, T. M. Hoogland, and P. Saggau, "Fast functional imaging of single neurons using random-access multiphoton (RAMP) microscopy," *Journal of Neurophysiology*, vol. 95, no. 1, pp. 535–545, Jan 2006.
- [76] L. H. Tay, O. Griesbeck, and D. T. Yue, "Live-Cell Transforms between Ca^{2+} Transients and FRET Responses for a Troponin-C-Based Ca^{2+} Sensor." *Biophys J*, vol. 93, no. 11, pp. 4031–4040, Aug 2007. [Online]. Available: <http://dx.doi.org/10.1529/biophysj.107.109629>
- [77] R. Yasuda, E. A. Nimchinsky, V. Scheuss, T. A. Pologruto, T. G. Oertner, B. L. Sabatini, and K. Svoboda, "Imaging calcium concentration dynamics in small neuronal compartments." *Sci STKE*, vol. 2004, no. 219, p. pl5, Feb 2004. [Online]. Available: <http://dx.doi.org/10.1126/stke.2192004pl5>
- [78] D. F. Reiff, A. Ihring, G. Guerrero, E. Y. Isacoff, M. Joesch, J. Nakai, and A. Borst, "In vivo performance of genetically encoded indicators of neural activity in flies." *J Neurosci*, vol. 25, no. 19, pp. 4766–4778, May 2005. [Online]. Available: <http://dx.doi.org/10.1523/JNEUROSCI.4900-04.2005>
- [79] A. Borst and H. D. I. Abarbanel, "Relating a calcium indicator signal to the

BIBLIOGRAPHY

- unperturbed calcium concentration time-course.” *Theor Biol Med Model*, vol. 4, no. 1, p. 7, 2007. [Online]. Available: <http://dx.doi.org/10.1186/1742-4682-4-7>
- [80] J. N. D. Kerr, D. Greenberg, and F. Helmchen, “Imaging input and output of neocortical networks in vivo,” *Proceedings of The National Academy Of Sciences Of The United States Of America*, vol. 102, no. 39, pp. 14 063–14 068, Sep 2005.
- [81] B. L. Sabatini and W. G. Regehr, “Optical measurement of presynaptic calcium currents.” *Biophys J*, vol. 74, no. 3, pp. 1549–1563, Mar 1998.
- [82] L. N. Cornelisse, R. A. J. van Elburg, R. M. Meredith, R. Yuste, and H. D. Mansvelder, “High speed two-photon imaging of calcium dynamics in dendritic spines: consequences for spine calcium kinetics and buffer capacity.” *PLoS ONE*, vol. 2, no. 10, p. e1073, 2007. [Online]. Available: <http://dx.doi.org/10.1371/journal.pone.0001073>
- [83] W. G. Regehr and P. P. Atluri, “Calcium transients in cerebellar granule cell presynaptic terminals.” *Biophys J*, vol. 68, no. 5, pp. 2156–2170, May 1995.
- [84] A. Smith, A. Doucet, N. de Freitas, and N. Gordon, *Sequential Monte Carlo Methods in Practice*. New York: Springer, 2001.
- [85] A. Dempster, N. Laird, D. Rubin *et al.*, “Maximum likelihood from incomplete data via the EM algorithm,” *Journal of the Royal Statistical Society. Series B (Methodological)*, vol. 39, no. 1, pp. 1–38, 1977.

BIBLIOGRAPHY

- [86] Y. Gao, M. Black, E. Bienenstock, S. Shoham, and J. Donoghue, “Probabilistic inference of hand motion from neural activity in motor cortex,” *Advances in Neural Information Processing Systems*, vol. 14, pp. 213–20, 2002.
- [87] A. E. Brockwell, A. L. Rojas, and R. E. Kass, “Recursive Bayesian decoding of motor cortical signals by particle filtering,” *J Neurophysiol*, vol. 91, no. 4, pp. 1899–1907, Apr 2004. [Online]. Available: <http://dx.doi.org/10.1152/jn.00438.2003>
- [88] R. Kelly and T. Lee, “Decoding V1 Neuronal Activity using Particle Filtering with Volterra Kernels,” *Advances in Neural Information Processing Systems*, vol. 15, pp. 1359–1366, 2004.
- [89] K. Samejima, K. Doya, Y. Ueda, and M. Kimura, “Estimating internal variables and parameters of a learning agent by a particle filter,” *Advances in Neural Information Processing Systems*, vol. 16, 2004.
- [90] Q. Huys and L. Paninski, “Model-based optimal interpolation and filtering for noisy, intermittent biophysical recordings,” *CNS meeting*, 2006.
- [91] T. D. Sanger, “Bayesian filtering of myoelectric signals,” *J Neurophysiol*, vol. 97, no. 2, pp. 1839–1845, Feb 2007. [Online]. Available: <http://dx.doi.org/10.1152/jn.00936.2006>
- [92] A. Ergün, R. Barbieri, U. T. Eden, M. A. Wilson, and E. N. Brown, “Construction

BIBLIOGRAPHY

- of point process adaptive filter algorithms for neural systems using sequential monte carlo methods.” *IEEE Trans Biomed Eng*, vol. 54, no. 3, pp. 419–428, Mar 2007.
- [93] L. R. Rabiner, “A Tutorial on Hidden Markov Models and Selected Applications in Speech Recognition,” *Proceedings of the IEEE*, vol. 72, no. 2, pp. 257–286, February 1989.
- [94] R. Kalman, “A new approach to linear filtering and prediction problems,” *Journal of Basic Engineering*, vol. 82, no. 1, pp. 35–45, 1960.
- [95] R. Douc, O. Cappe, and E. Moulines, “Comparison of resampling schemes for particle filtering,” *Image and Signal Processing and Analysis, 2005. ISPA 2005. Proceedings of the 4th International Symposium on*, pp. 64–69, 2005.
- [96] A. Wills, T. Schön, and B. Ninness, “Parameter estimation for discrete-time nonlinear systems using em,” *Proceedings of the 17th IFAC World Congress*, Jul. 2008.
- [97] P. McCullagh and J. Nelder, *Generalized Linear Models*. Chapman and Hall, 1989.
- [98] L. Paninski, J. Pillow, and J. Lewi, “Statistical models for neural encoding, decoding, and optimal stimulus design.” *Prog Brain Res*, vol. 165, pp. 493–507, 2007. [Online]. Available: [http://dx.doi.org/10.1016/S0079-6123\(06\)65031-0](http://dx.doi.org/10.1016/S0079-6123(06)65031-0)
- [99] S. Escola and L. Paninski, “Hmms applied toward the inference of neural states and the improved estimation of linear rfs,” in *COSYNE*, 2007.

BIBLIOGRAPHY

- [100] L. Paninski, “Maximum likelihood estimation of cascade point-process neural encoding models,” *Network: Computation in Neural Systems*, vol. 15, pp. 243–262, 2004.
- [101] W. Truccolo, U. T. Eden, M. R. Fellows, J. P. Donoghue, and E. N. Brown, “A point process framework for relating neural spiking activity to spiking history, neural ensemble, and extrinsic covariate effects,” *J Neurophysiol*, vol. 93, no. 2, pp. 1074–1089, Feb 2005. [Online]. Available: <http://dx.doi.org/10.1152/jn.00697.2004>
- [102] L. Paninski, J. W. Pillow, and E. P. Simoncelli, “Maximum likelihood estimation of a stochastic integrate-and-fire neural encoding model,” *Neural Computation*, vol. 16, no. 12, pp. 2533–2561, Dec 2004.
- [103] D. A. Dombeck, A. N. Khabbaz, F. Collman, T. L. Adelman, and D. W. Tank, “Imaging large-scale neural activity with cellular resolution in awake, mobile mice,” *Neuron*, vol. 56, no. 1, pp. 43–57, Oct 2007. [Online]. Available: <http://dx.doi.org/10.1016/j.neuron.2007.08.003>
- [104] R. W. Tsien and R. Y. Tsien, “Calcium channels, stores, and oscillations,” *Annu Rev Cell Biol*, vol. 6, pp. 715–760, 1990. [Online]. Available: <http://dx.doi.org/10.1146/annurev.cb.06.110190.003435>
- [105] J. Pillow, J. Shlens, L. Paninski, A. Sher, A. Litke, E. Chichilnisky, and E. Simoncelli, “Spatiotemporal correlations and visual signaling in a complete neuronal population,” *Nature*, vol. 454, no. 7207, pp. 995–9, Aug 21 2008.

BIBLIOGRAPHY

- [106] R. Shumway and D. Stoffer, *Time Series Analysis and Its Applications*, 2nd ed. New York, NY: Springer, 2006.
- [107] S. Ramon y Cajal, *Recuerdos de mi vida: Historia de mi labor científica*. Alianza Editorial, 1923.
- [108] K. Micheva and S. Smith, “Array tomography: A new tool for imaging the molecular architecture and ultrastructure of neural circuits,” *Neuron*, vol. 55, pp. 25–36, 2007.
- [109] J. Livet, T. Weissman, H. Kang, R. Draft, J. Lu, R. Bennis, J. Sanes, and J. Lichtman, “Transgenic strategies for combinatorial expression of fluorescent proteins in the nervous system.” *Nature*, vol. 450, pp. 56–62, 2007.
- [110] K. L. Briggman and W. Denk, “Towards neural circuit reconstruction with volume electron microscopy techniques.” *Current Opinions in Neurobiology*, vol. 16, p. 562, 2006.
- [111] N. Hatsopoulos, C. Ojakangas, L. Paninski, and J. Donoghue, “Information about movement direction obtained by synchronous activity of motor cortical neurons,” *PNAS*, vol. 95, pp. 15 706–15 711, 1998.
- [112] K. Harris, J. Csicsvari, H. Hirase, G. Dragoi, and G. Buzsaki, “Organization of cell assemblies in the hippocampus,” *Nature*, vol. 424, pp. 552–556, 2003.
- [113] R. B. Stein, D. J. Weber, Y. Aoyagi, A. Prochazka, J. B. M. Wagenaar, S. Shoham, and R. A. Normann, “Coding of position by simultaneously recorded sensory

BIBLIOGRAPHY

- neurones in the cat dorsal root ganglion,” *J Physiol (Lond)*, vol. 560, no. 3, pp. 883–896, 2004. [Online]. Available: <http://jp.physoc.org/cgi/content/abstract/560/3/883>
- [114] G. Santhanam, S. I. Ryu, B. M. Yu, A. Afshar, and K. V. Shenoy, “A high-performance brain-computer interface,” *Nature*, vol. 442, pp. 195–198, 2006.
- [115] A. Luczak, P. Bartho, S. Marguet, G. Buzsaki, and K. Harris, “Sequential structure of neocortical spontaneous activity in vivo,” *PNAS*, vol. 104, pp. 347–352, 2007.
- [116] R. Segev, J. Goodhouse, J. Puchalla, and M. Berry, “Recording spikes from a large fraction of the ganglion cells in a retinal patch,” *Nature Neuroscience*, vol. 7, pp. 1154–1161, 2004.
- [117] A. Litke, N. Bezayiff, E. Chichilnisky, W. Cunningham, W. Dabrowski, A. Grillo, M. Grivich, P. Grybos, P. Hottowy, S. Kachiguine, R. Kalmar, K. Mathieson, D. Petrusca, M. Rahman, and A. Sher, “What does the eye tell the brain? development of a system for the large scale recording of retinal output activity,” *IEEE Trans Nucl Sci*, pp. 1434–1440, 2004.
- [118] D. Petrusca, M. I. Grivich, A. Sher, G. D. Field, J. L. Gauthier, M. Greschner, J. Shlens, E. J. Chichilnisky, and A. M. Litke, “Identification and characterization of a Y-like primate retinal ganglion cell type,” *J. Neurosci.*, vol. 27, no. 41, pp. 11 019–11 027, 2007. [Online]. Available: <http://www.jneurosci.org/cgi/content/abstract/27/41/11019>

BIBLIOGRAPHY

- [119] J. Pillow, J. Shlens, L. Paninski, A. Sher, A. Litke, E. Chichilnisky, and E. Simoncelli, “Spatiotemporal correlations and visual signaling in a complete neuronal population,” *Nature*, vol. 454, pp. 995–999, 2008.
- [120] N. Lei, B. Watson, M. J. R. Yuste, and K. Shepard, “A 256-by-256 cmos microelectrode array for extracellular stimulation of acute brain slices.” in *Proceedings to the International Solid-State Circuits Conference*, 2008.
- [121] M. Abeles, *Corticonics*. Cambridge University Press, 1991.
- [122] V. Braitenberg and A. Schuz, *Cortex: statistics and geometry of neuronal connectivity*. Berlin: Springer, 1998.
- [123] R. Y. Tsien, “Fluorescent probes of cell signaling,” *Ann. Rev. Neurosci.*, vol. 12, pp. 227–253, 1989.
- [124] R. Cossart, D. Aronov, and R. Yuste, “Attractor dynamics of network up states in the neocortex,” *Nature*, vol. 423, pp. 283–288, 2003.
- [125] K. Ohki, S. Chung, Y. Ch’ng, P. Kara, and C. Reid, “Functional imaging with cellular resolution reveals precise micro-architecture in visual cortex,” *Nature*, vol. 433, pp. 597–603, 2005.
- [126] M. Djuricic, S. Antic, W. R. Chen, and D. Zecevic, “Voltage imaging from dendrites of mitral cells: EPSP attenuation and spike trigger zones,”

BIBLIOGRAPHY

- J. Neurosci.*, vol. 24, no. 30, pp. 6703–6714, 2004. [Online]. Available: <http://www.jneurosci.org/cgi/content/abstract/24/30/6703>
- [127] V. Iyer, T. M. Hoogland, and P. Saggau, “Fast functional imaging of single neurons using random-access multiphoton (RAMP) microscopy,” *J Neurophysiol*, vol. 95, no. 1, pp. 535–545, 2006.
- [128] R. Salome, Y. Kremer, S. Dieudonne, J.-F. Leger, O. Krichevsky, C. Wyart, D. Chate-
nay, and L. Bourdieu, “Ultrafast random-access scanning in two-photon microscopy
using acousto-optic deflectors,” *Journal of Neuroscience Methods*, vol. 154, no. 1-2,
pp. 161–174, Jun 2006.
- [129] G. Reddy, K. Kelleher, R. Fink, and P. Saggau, “Three-dimensional random access
multiphoton microscopy for functional imaging of neuronal activity,” *Nature Neuro-
science*, vol. 11, no. 6, pp. 713–720, 2008.
- [130] A. Roxin, V. Hakim, and N. Brunel, “The statistics of repeating patterns of cortical
activity can be reproduced by a model network of stochastic binary neurons,” *J.
Neurosci.*, vol. 28, no. 42, pp. 10 734–10 745, 2008.
- [131] D. Brillinger, “Maximum likelihood analysis of spike trains of interacting nerve
cells,” *Biological Cyberkinetics*, vol. 59, pp. 189–200, 1988.
- [132] E. Chornoboy, L. Schramm, and A. Karr, “Maximum likelihood identification of
neural point process systems,” *Biological Cybernetics*, vol. 59, pp. 265–275, 1988.

BIBLIOGRAPHY

- [133] D. Brillinger, “Nerve cell spike train data analysis: a progression of technique,” *Journal of the American Statistical Association*, vol. 87, pp. 260–271, 1992.
- [134] H. Plesser and W. Gerstner, “Noise in integrate-and-fire neurons: From stochastic input to escape rates,” *Neural Computation*, vol. 12, pp. 367–384, 2000.
- [135] L. Paninski, M. Fellows, S. Shoham, N. Hatsopoulos, and J. Donoghue, “Super-linear population encoding of dynamic hand trajectory in primary motor cortex,” *J. Neurosci.*, vol. 24, pp. 8551–8561, 2004.
- [136] L. Paninski, “Maximum likelihood estimation of cascade point-process neural encoding models,” *Network: Computation in Neural Systems*, vol. 15, pp. 243–262, 2004.
- [137] F. Rigat, M. de Gunst, and J. van Pelt, “Bayesian modelling and analysis of spatio-temporal neuronal networks,” *Bayesian Analysis*, vol. 1, pp. 733–764, 2006.
- [138] W. Truccolo, U. Eden, M. Fellows, J. Donoghue, and E. Brown, “A point process framework for relating neural spiking activity to spiking history, neural ensemble and extrinsic covariate effects,” *Journal of Neurophysiology*, vol. 93, pp. 1074–1089, 2005.
- [139] D. Nykamp, “A mathematical framework for inferring connectivity in probabilistic neuronal networks,” *Mathematical Biosciences*, vol. 205, pp. 204–251, 2007.

BIBLIOGRAPHY

- [140] J. Kulkarni and L. Paninski, “Common-input models for multiple neural spike-train data,” *Network: Computation in Neural Systems*, vol. 18, pp. 375–407, 2007.
- [141] M. Vidne, J. Kulkarni, Y. Ahmadian, J. Pillow, J. Shlens, E. Chichilnisky, E. Simoncelli, and L. Paninski, “Inferring functional connectivity in an ensemble of retinal ganglion cells sharing a common input,” *COSYNE*, 2009.
- [142] I. H. Stevenson, J. M. Rebesco, N. G. Hatsopoulos, Z. Haga, L. E. Miller, and K. P. Kording, “Bayesian inference of functional connectivity and network structure from spikes,” *IEEE Trans. Neural Systems and Rehab.*, vol. 17, pp. 203–13, 2009.
- [143] S. Escola and L. Paninski, “Hidden Markov models applied toward the inference of neural states and the improved estimation of linear receptive fields,” *Under review, Neural Computation*, 2008.
- [144] K. Li and N. Duan, “Regression analysis under link violation,” *Annals of Statistics*, vol. 17, pp. 1009–1052, 1989.
- [145] S. Lefort, C. Tómm, J.-C. Floyd Sarria, and C. C. H. Petersen, “The excitatory neuronal network of the c2 barrel column in mouse primary somatosensory cortex,” *Neuron*, vol. 61, pp. 301–16, 2009.
- [146] R. Yasuda, E. A. Nimchinsky, V. Scheuss, T. A. Polgruto, T. G. Oertner, B. L. Sabatini, and K. Svoboda, “Imaging calcium concentration dynamics in small neuronal compartments,” *Sci STKE*, vol. 219, p. p15, 2004.

BIBLIOGRAPHY

- [147] A. Dempster, N. Laird, and D. Rubin, “Maximum likelihood from incomplete data via the EM algorithm,” *Journal Royal Stat. Soc., Series B*, vol. 39, pp. 1–38, 1977.
- [148] G. McLachlan and T. Krishnan, *The EM Algorithm and Extensions*. Wiley-Interscience, 1996.
- [149] L. Rabiner, “A tutorial on hidden Markov models and selected applications in speech recognition,” *Proceedings of the IEEE*, vol. 77, pp. 257–286, 1989.
- [150] A. Doucet, S. Godsill, and C. Andrieu, “On sequential Monte Carlo sampling methods for Bayesian filtering,” *Statistics and Computing*, vol. 10, pp. 197–208, 2000.
- [151] A. Doucet, N. de Freitas, and N. Gordon, Eds., *Sequential Monte Carlo in Practice*. Springer, 2001.
- [152] S. Godsill, A. Doucet, and M. West, “Monte Carlo smoothing for non-linear time series,” *Journal of the American Statistical Association*, vol. 99, pp. 156–168, 2004.
- [153] R. Douc, O. Cappe, and E. Moulines, “Comparison of resampling schemes for particle filtering,” *Proc. 4th Int. Symp. Image and Signal Processing and Analysis*, 2005.
- [154] E. Buhl, K. Halasy, and P. Somogyi, “Diverse sources of hippocampal unitary inhibitory postynaptic potentials and the number of synaptic release sites,” *Nature*, vol. 368, pp. 823–828, 1994.
- [155] A. Thompson, D. Girdlestone, and D. West, “Voltage-dependent currents prolong

BIBLIOGRAPHY

- single-axon postsynaptic potentials in layer III pyramidal neurons in rat neocortical slices,” *J Neurophysiol*, vol. 60, pp. 1896–1907, 1988.
- [156] A. Reyes, R. Lujan, A. Rozov, N. Burnashev, P. Somogyi, and B. Sakmann, “Target-cell-specific facilitation and depression in neocortical circuits,” *Nat Neurosci*, vol. 1, pp. 279–285, 1998.
- [157] D. Feldmeyer, V. Egger, J. Lubke, and B. Sakmann, “Reliable synaptic connections between pairs of excitatory layer 4 neurones within a single “barrel” of developing rat somatosensory cortex,” *J Physiol*, vol. 521 Pt 1, pp. 169–90., 1999.
- [158] A. Gupta, Y. Wang, and H. Markram, “Organizing principles for a diversity of gabaergic interneurons and synapses in the neocortex,” *Science*, vol. 287, pp. 273–8, 2000.
- [159] D. Feldmeyer and B. Sakmann, “Synaptic efficacy and reliability of excitatory connections between the principal neurones of the input (layer 4) and output layer (layer 5) of the neocortex,” *J Physiol*, vol. 525, pp. 31–9, 2000.
- [160] C. C. Petersen and B. Sakmann, “The excitatory neuronal network of rat layer 4 barrel cortex,” *J Neurosci*, vol. 20, no. 20, pp. 7579–86., 2000.
- [161] T. Binzegger, R. J. Douglas, and K. A. C. Martin, “A Quantitative Map of the Circuit of Cat Primary Visual Cortex,” *J. Neurosci.*, vol. 24, no. 39, pp. 8441–8453, 2004.

BIBLIOGRAPHY

- [162] S. Song, P. J. Sjöström, M. Reigl, S. Nelson, and D. B. Chklovskii, “Highly non-random features of synaptic connectivity in local cortical circuits.” *PLoS Biology*, vol. 3, p. e68, 2005.
- [163] Y. Mishchenko, J. Spacek, J. Mendenhall, D. Chklovskii, and K. M. Harris, “Reconstruction of hippocampal CA1 neuropil at nanometer resolution reveals disordered packing of processes and dependence of synaptic connectivity on local environment and dendritic caliber.” *Submitted*, 2009.
- [164] I. Stevenson, J. Rebeschke, N. Hatsopoulos, Z. Haga, L. Miller, and K. Koerding, “Inferring network structure from spikes,” *Statistical Analysis of Neural Data meeting*, 2008.
- [165] R. Tibshirani, “Regression shrinkage and selection via the lasso,” *Journal of the Royal Statistical Society. Series B*, vol. 58, pp. 267–288, 1996.
- [166] M. Tipping, “Sparse Bayesian learning and the relevance vector machine,” *Journal of Machine Learning Research*, vol. 1, pp. 211–244, 2001.
- [167] D. Donoho and M. Elad, “Optimally sparse representation in general (nonorthogonal) dictionaries via L^1 minimization,” *PNAS*, vol. 100, pp. 2197–2202, 2003.
- [168] A. Ng, “Feature selection, L_1 vs. L_2 regularization, and rotational invariance,” *ICML*, vol. 21, 2004.

BIBLIOGRAPHY

- [169] E. J. Candes and M. Wakin, “An introduction to compressive sampling,” *IEEE Signal Processing Magazine*, vol. 25, no. 2, pp. 21–30, 2008.
- [170] Y. Mishchenko, “Strategies for identifying exact structure of neural circuits with broad light microscopy connectivity probes,” *Preprint*: <http://precedings.nature.com/documents/2669/version/2>, 2009.
- [171] R. J. Sayer, M. J. Friedlander, and S. J. Redman, “The time course and amplitude of epsps evoked at synapses between pairs of CA3/CA1 neurons in the hippocampal slice,” *J. Neurosci.*, vol. 10, pp. 826–36, 1990.
- [172] S. M. Gomez-Urquijo, C. Reblet, J. L. Bueno-Lopez, and I. Gutierrez-Ibarluzea, “Gabaergic neurons in the rabbit visual cortex: percentage, distribution and cortical projections,” *Brain Res*, vol. 862, pp. 171–9, 2000.
- [173] C. Koch, *Biophysics of Computation*. Oxford University Press, 1999.
- [174] J. MacLean, B. Watson, G. Aaron, and R. Yuste, “Internal dynamics determine the cortical response to thalamic stimulation,” *Neuron*, vol. 48, pp. 811–823, 2005.
- [175] T. P. Vogels and L. F. Abbott, “Signal propagation and logic gating in networks of integrate-and-fire neurons,” *J Neurosci*, vol. 25, no. 46, pp. 10 786–10 795, Nov 2005. [Online]. Available: <http://dx.doi.org/10.1523/JNEUROSCI.3508-05.2005>
- [176] M. Garofalo, T. Nieuw, P. Massobrio, and S. Martinoia, “Evaluation of the perfor-

BIBLIOGRAPHY

- mance of information theory-based methods and cross-correlation to estimate the functional connectivity in cortical networks,” *PLoS ONE*, vol. 4, p. e6482, 2009.
- [177] S. Cocco, S. Leibler, and R. Monasson, “Neuronal couplings between retinal ganglion cells inferred by efficient inverse statistical physics methods,” *Proc Natl Acad Sci U S A*, vol. 106, no. 33, pp. 14 058–14 062, Aug 2009. [Online]. Available: <http://dx.doi.org/10.1073/pnas.0906705106>
- [178] D. Q. Nykamp, “Revealing pairwise coupling in linear-nonlinear networks,” *SIAM J Applied Mathematics*, vol. 65, no. 6, pp. 2005–2032, 2005.
- [179] V. A. Vakorin, O. A. Krakovska, and A. R. McIntosh, “Confounding effects of indirect connections on causality estimation,” *Journal of Neuroscience Methods*, vol. In press, 2009.
- [180] E. S. Boyden, F. Zhang, E. Bamberg, G. Nagel, and K. Deisseroth, “Millisecond-timescale, genetically targeted optical control of neural activity,” *Nat Neurosci*, vol. 8, no. 9, pp. 1263–1268, Sep 2005.
- [181] S. Szobota, P. Gorostiza, F. Del Bene, C. Wyart, D. L. Fortin, K. D. Kolstad, O. Tulyathan, M. Volgraf, R. Numano, H. L. Aaron, E. K. Scott, R. H. Kramer, J. Flannery, H. Baier, D. Trauner, and E. Y. Isacoff, “Remote control of neuronal activity with a light-gated glutamate receptor,” *Neuron*, vol. 54, pp. 535–545, 2007.
- [182] V. Nikolenko, B. O. Watson, R. Araya, A. Woodruff, D. S. Peterka, and R. Yuste,

BIBLIOGRAPHY

- “Slm microscopy: Scanless two-photon imaging and photostimulation with spatial light modulators.” *Front Neural Circuits*, vol. 2, p. 5, 2008. [Online]. Available: <http://dx.doi.org/10.3389/neuro.04.005.2008>
- [183] J. Vogelstein, B. Babadi, B. Watson, R. Yuste, and L. Paninski, “Fast nonnegative deconvolution via tridiagonal interior-point methods, applied to calcium fluorescence data.” *Statistical analysis of neural data (SAND) conference*, 2008.
- [184] L. Paninski, Y. Ahmadian, D. Ferreira, S. Koyama, K. Rahnema, M. Vidne, J. Vogelstein, and W. Wu, “A new look at state-space models for neural data,” *Journal of Computational Neuroscience*, vol. In press, 2009.
- [185] H. Ishwaran, “Applications of hybrid Monte Carlo to Bayesian generalized linear models: quasicomplete separation and neural networks,” *Journal of Computational and Graphical Statistics*, vol. 8, pp. 779–799, 1999.
- [186] D. Gamerman, “Sampling from the posterior distribution in generalized linear mixed models,” *Statistics and Computing*, vol. 7, no. 1, pp. 57–68, 1997.
- [187] —, “Markov chain monte carlo for dynamic generalised linear models,” *Biometrika*, vol. 85, no. 1, pp. 215–227, 1998.
- [188] Y. Ahmadian, J. Pillow, and L. Paninski, “Efficient Markov Chain Monte Carlo methods for decoding population spike trains.” *Under review, Neural Computation*, 2009.

BIBLIOGRAPHY

- [189] V. Nikolenko, K. Poskanzer, and R. Yuste, “Two-photon photostimulation and imaging of neural circuits,” *Nature Methods*, vol. 4, pp. 943–950, 2007.
- [190] A. H. Meyer, I. Katona, M. Blatow, A. Rozov, and H. Monyer, “In Vivo Labeling of Parvalbumin-Positive Interneurons and Analysis of Electrical Coupling in Identified Neurons,” *J. Neurosci.*, vol. 22, pp. 7055–7064, 2002.
- [191] D. S. Greenberg and J. N. Kerr, “Automated correction of fast motion artifacts for two-photon imaging of awake animals,” *Journal of Neuroscience Methods*, vol. 176, no. 1, pp. 1–15, 01 2009. [Online]. Available: <http://dx.doi.org/10.1016/j.jneumeth.2008.08.020>
- [192] F. Wood and M. Black, “A nonparametric Bayesian alternative to spike sorting,” *Journal of Neuroscience Methods*, vol. 173, pp. 1–12, 2008.
- [193] V. Fedorov, *Theory of Optimal Experiments*. New York: Academic Press, 1972.
- [194] K. Chaloner and I. Verdinelli, “Bayesian experimental design: A review,” *Statistical Science*, vol. 10, no. 3, pp. 273–304, 1995.
- [195] J. Lewi, R. Butera, and L. Paninski, “Sequential optimal design of neurophysiology experiments,” *Neural Computation*, vol. 21, pp. 619–687, 2009.
- [196] E. Callaway and R. Yuste, “Stimulating neurons with light,” *Current Opinion in Neurobiology*, vol. 12, pp. 587–592, 2002.

BIBLIOGRAPHY

- [197] E. Fino, R. Araya, D. S. Peterka, M. Salierno, R. Etchenique, and R. Yuste, “Rubi-glutamate: Two-photon and visible-light photoactivation of neurons and dendritic spines.” *Front Neural Circuits*, vol. 3, p. 2, 2009. [Online]. Available: <http://dx.doi.org/10.3389/neuro.04.002.2009>
- [198] S. K. Mohanty, R. K. Reinscheid, X. Liu, N. Okamura, T. B. Krasieva, and M. W. Berns, “In-Depth Activation of Channelrhodopsin 2-Sensitized Excitable Cells with High Spatial Resolution Using Two-Photon Excitation with a Near-Infrared Laser Microbeam,” *Biophys. J.*, vol. 95, no. 8, pp. 3916–3926, 2008.
- [199] J. P. Rickgauer and D. W. Tank, “Two-photon excitation of channelrhodopsin-2 at saturation.” *Proc Natl Acad Sci U S A*, vol. 106, no. 35, pp. 15 025–15 030, Sep 2009. [Online]. Available: <http://dx.doi.org/10.1073/pnas.0907084106>
- [200] A. A. Oliva, M. Jiang, T. Lam, K. L. Smith, and J. W. Swann, “Novel hippocampal interneuronal subtypes identified using transgenic mice that express green fluorescent protein in gabaergic interneurons.” *J Neurosci*, vol. 20, no. 9, pp. 3354–3368, May 2000.
- [201] I. Wickersham, D. Lyon, R. Barnard, T. Mori, S. Finke, K.-K. Conzelmann, J. Young, and E. Callaway, “Monosynaptic restriction of transsynaptic tracing from single, genetically targeted neurons,” *Neuron*, vol. 53, pp. 639–647, 2007.

Vita



Joshua T. Vogelstein graduated with a B.S. degree in Biomedical Engineering from Washington University in St. Louis in 2002, enrolled in the Neuroscience Ph.D. program at Johns Hopkins University in 2003, and enrolled in the Joint Master's program from the Department of Applied Mathematics and Statistics in 2009. His research has focused developing statistical models and algorithms for the analysis of spike related time-varying neural signals.

Starting in January 2010, Joshua will work on developing “Neurocognitive Graph Theory,” jointly at the Johns Hopkins University National Center of Applied Neuroscience and the Department of Applied Mathematics and Statistics, under the guidance of Carey Priebe and R. Jacob Vogelstein, where he will be pushing the limits with respect to what kinds of questions neuroscientists can even address.